

26021

*Shelley
Gullett
Shelley*

**QUARTERLY PROGRESS REPORT
METALLURGY RESEARCH OPERATION**

APRIL, MAY, JUNE, 1964

Reproduced From
Best Available Copy

JULY 15, 1964

DISTRIBUTION STATEMENT A
Approved for Public Release
Distribution Unlimited

HANFORD LABORATORIES

HANFORD ATOMIC PRODUCTS OPERATION
RICHLAND, WASHINGTON

GENERAL  ELECTRIC

AMPTIAC

20000721 096

DTIC QUALITY INSPECTED 4

LEGAL NOTICE

This report was prepared as an account of Government sponsored work. Neither the United States, nor the Commission, nor any person acting on behalf of the Commission:

A. Makes any warranty or representation, expressed or implied, with respect to the accuracy, completeness, or usefulness of the information contained in this report, or that the use of any information, apparatus, method, or process disclosed in this report may not infringe privately owned rights; or

B. Assumes any liabilities with respect to the use of, or for damages resulting from the use of any information, apparatus, method, or process disclosed in this report.

As used in the above, "person acting on behalf of the Commission" includes any employee or contractor of the Commission, or employee of such contractor, to the extent that such employee or contractor of the Commission, or employee of such contractor prepares, disseminates, or provides access to, any information pursuant to his employment or contract with the Commission, or his employment with such contractor.

HW-82651

UC-25, Metals, Ceramics
and Materials
(TID-4500, 32nd Ed.)

QUARTERLY PROGRESS REPORT
METALLURGY RESEARCH OPERATION

APRIL, MAY, JUNE, 1964

By

FIRST UNRESTRICTED
DISTRIBUTION MADE

SEP 21 '64

Staff of Metallurgy Research Operation

J. J. Cadwell

Manager

J. C. Tobin
T. K. Bierlein
R. L. Dillon
R. G. Wheeler

Manager, Reactor Metals Research
Manager, Physical Metallurgy
Manager, Chemical Metallurgy
Manager, Materials Engineering

July 15, 1964

HANFORD ATOMIC PRODUCTS OPERATION
RICHLAND, WASHINGTON

Work performed under Contract No. AT(45-1)-1350, between the
Atomic Energy Commission and General Electric Company

WARNING - PRELIMINARY REPORT

This report contains information of a preliminary nature and is prepared
primarily for the use of Hanford Atomic Products Operation personnel.
It is subject to revision on further checking or collection of additional data.

Printed by/for the U. S. Atomic Energy Commission

Printed in USA. ~~Price \$2.75~~ Available from the
Office of Technical Services
Department of Commerce
Washington 25, D. C.

DISTRIBUTION STATEMENT A
Approved for Public Release
Distribution Unlimited

Previous reports in this series:

HW-76228	October, November, December, 1962
HW-77052	January, February, March, 1963
HW-77954	April, May, June, 1963
HW-78962	July, August, September, 1963
HW-79766	October, November, December, 1963
HW-81269	January, February, March, 1964

TABLE OF CONTENTS

SUMMARY	2.1
PHYSICAL METALLURGY	3.1
NEUTRON DAMAGE TO METALS - H. E. Kissinger, J. J. Laidler, B. Mastel, and J. L. Brimhall	3.1
Transmission Electron Microscopy	3.1
Slip Line Study.	3.6
X-Ray Diffraction.	3.12
SWELLING OF IRRADIATED FISSIONABLE MATERIALS - R. D. Leggett, B. Mastel, Y. E. Smith, and J. W. Weber	3.15
Irradiation Program	3.15
Postirradiation Examination.	3.21
Second-Phase Distribution in Dilute Alloys of Uranium.	3.39
PLUTONIUM PHYSICAL METALLURGY - R. D. Nelson, F. E. Bowman, H. E. Kissinger, and B. Mastel	3.47
Steady-State Creep of Plutonium	3.47
Plutonium Research Glovebox	3.51
Metallography	3.52
Transformation Kinetics.	3.55
Deformation and Fracture Mechanisms	3.55
REACTOR METALS RESEARCH	4.1
ALLOY SELECTION - T. T. Claudson	4.1
Mechanical Property Testing	4.5
IN-REACTOR MEASUREMENTS OF MECHANICAL PROPERTIES J. J. Holmes, D. H. Nyman, and J. A. Williams	4.12
In-Reactor Measurements	4.12
IRRADIATION FACILITIES OPERATION - J. E. Irvin.	4.14
Facilities Operation	4.14
IRRADIATION DAMAGE TO ZIRCALOY-2 - J. E. Irvin	4.16
Surveillance of NPR Tubing	4.16
IRRADIATION DAMAGE TO STAINLESS STEELS - J. E. Irvin	4.30
Austenitic Stainless Steels	4.30

IRRADIATION DAMAGE TO NICKEL-BASE ALLOYS	
I. S. Levy and K. R. Wheeler	4.35
Solid-Solution Hardened Alloys	4.35
Precipitation-Hardened Alloys	4.35
DAMAGE MECHANISMS - F. A. Smidt	4.41
CHEMICAL METALLURGY	5.1
ENVIRONMENTAL EFFECTS	5.1
Water Environment - W. A. Burns.	5.1
Environmental Effects - Low Oxygen Coolant Program - W. A. Burns	5.4
Corrosion of ATR Loop Structural Materials - R. E. Westerman	5.5
Gas-Solid Reactions at High Temperatures - W. J. Guay	5.7
Gas Chromatograph - D. W. Shannon	5.9
Irradiation Effects on the Corrosion of PRTR Zircaloy-2 Process Tubes - H. P. Maffei.	5.13
Effect of Thermal Cycling on the Oxidation of Zircaloy-2 - D. W. Shannon	5.15
Effect of Mechanically Flexing Autoclaved Zircaloy-2 Samples on Subsequent Corrosion Behavior - V. H. Troutner*, W. C. Craven, and R. L. Dillon	5.17
Zirconium Hydriding Mechanism - D. W. Shannon	5.20
ADVANCED REACTOR CONCEPT STUDIES.	5.25
Hydride Moderator - W. J. Guay	5.25
Variable Composition Hydride Moderator Studies - W. J. Guay	5.27
PRODUCTION REACTOR CORROSION AND COATING STUDIES	5.28
Corrosion of Aluminum-Rotating Disk Method - A. B. Johnson	5.28
N REACTOR CORROSION AND HYDRIDING STUDIES	5.29
Effect of Thick Oxide Films on the Hydriding of Zircaloy-2 in Contaminated Helium - D. W. Shannon.	5.29

* General Electric Company, Pinellas Peninsula Plant

MATERIALS ENGINEERING	6.1
PRTR PRESSURE TUBES.	6.1
In-Reactor Monitoring - P. J. Pankaskie	6.1
Tube Testing - M. C. Fraser	6.2
N REACTOR PRESSURE TUBES	6.4
Brittle Fracture Tests - R. C. Aungust	6.4
Irradiated Tube Testing Facility - P. M. Jackson	6.7

SUMMARY

PHYSICAL METALLURGY

NEUTRON DAMAGE TO METALS

Electron microscopy studies revealed channels in molybdenum single crystals irradiated to 10^{19} nvt and subsequently strained, but not in crystals irradiated to only 18 nvt. Analysis of the channel traces on the (110) planes indicated that cross slip occurred.

A slip line study of an irradiated single crystal loaded in bending confirms that multiple slip on closely spaced planes causes channels.

Examination of an irradiated (10^{19} nvt) high-purity copper crystal showed that channeling occurs in face-centered cubic structures (copper) as well as body-centered cubic structures (molybdenum).

The accuracy of an X-ray technique for obtaining lattice parameters from single crystals was confirmed to be $\pm 0.001\%$. This measurement technique yielded lattice parameter values of $a_0 = 2.7604 \text{ \AA}$ and $c_0 = 4.4599 \text{ \AA}$ for a single crystal of rhenium. A modified version of this technique gave average values of $a_0 = 2.7599 \text{ \AA}$ and $c_0 = 4.4585 \text{ \AA}$ for a polycrystalline rhenium foil.

SWELLING OF IRRADIATED FISSIONABLE MATERIALS

Two irradiation capsules, one containing high-purity uranium specimens operating in the beta phase region (700 C or 1292 F) and the other containing enriched uranium specimens operating at 400 C (752 F), were discharged.

The high pressure prototype irradiation swelling capsule has successfully completed all out-of-reactor testing and a modified in-reactor capsule was built.

Examination was completed of specimens with various alloying additions. The operating temperature of the specimens was $\sim 575 \text{ C}$ (1067 F) and the exposure was 0.11 at. % burnup. The U + Fe - Al alloy specimens showed superior behavior to the U + Fe - Si alloy specimens which in turn

showed superior behavior to the high-purity dingot uranium specimens. A gamma anneal prior to the beta quench improved the behavior of both alloys. Improvements in swelling behavior are related to the decreases of micro-tearing developed at twin-matrix interfaces. Swelling data from high-purity uranium specimens of three different enrichments are also reported.

A quantitative metallography technique was applied to a U + Fe - Si alloy subjected to various solution and precipitation heat treatments. Alpha range solution heat prior to the precipitation treatment was inadequate while the beta solution treatment was effective in improving the as-received density of finely divided particles. Three numerical methods of analyzing the data from one sample were compared and differences in the resulting distribution are presented.

PLUTONIUM PHYSICAL METALLURGY

Steady-state creep tests on the six allotropes of plutonium have been completed and analysis of data is in progress. Activation energies and parameters in a material model proposed by Sherby have been evaluated. Anomalies in the creep of the beta phase formed by transformation from the gamma as opposed to transformation from the alpha are presented.

Vacuum cathodic and alternating current electrolytic etching techniques have been applied to alpha plutonium; these techniques show promise in the area of bright field optical and replica electron metallography.

The kinetics of the $\beta \rightarrow \alpha$ transformation in electrorefined metal were investigated at -196 C (-321 F); no physical damage was observed after nine transformation cycles.

Absorption of diffracted X-rays in plutonium is established to be so great as to limit texture information from a single surface. Castings and rolled specimens of electrorefined Los Alamos Scientific Laboratory (LASL) material have been made for the pole figure studies. Aging of castings appears to be detrimental to rolling. Diffraction patterns are presented for alpha plutonium produced by transformation from the beta under pressure.

REACTOR METALS RESEARCH

ALLOY SELECTION

Corrosion and oxidation tests have been performed on nickel-base alloys in water vapor and deoxygenated steam and at temperatures from 1200 F (649 C) to 1900 F (1038 C). Hastelloy R-235, Inconel 702, and Hastelloy N exhibited substantial weight losses in 1200 F (649 C) steam after 1680 hours. All other alloys showed weight gains, and in this group, those showing superior corrosion resistance were Hastelloy X-280, Inconel 600, Incoloy 800, and Inconel 718. Hastelloy N exhibited best overall performance when exposed to the water vapor environment tests. Severe intergranular penetration at each temperature was found in Incoloy 800, Inconel 702, and Hastelloy R-235.

Evaluation of the effects of irradiation on the mechanical properties of a variety of nickel-base alloys is continuing. The results of room temperature tests on specimens irradiated at several temperatures are given.

IN-REACTOR MEASUREMENTS OF MECHANICAL PROPERTIES

Two in-reactor creep tests on 304 AISI SS are in progress at temperature of 500 C (932 F) and stresses of 20,000 and 30,000 psi. The test at 20,000 psi is showing a creep rate below the minimum resolvable rate of 2.5×10^{-7} /hr. Out-of-reactor data at this temperature and stress is not yet available due to premature failure.

The in-reactor test at 30,000 psi stress and 500 C (932 F) showed a lower creep rate than the out-of-reactor test but a valid comparison will not be able to be made until another out-of-reactor test is started which will give the same temperature pulse as that observed in-reactor.

Up to termination due to heater failure after 600 hours, an in-reactor test at 30,000 psi and 550 C (932 F) showed no significant difference when compared to the out-of-reactor one.

IRRADIATION DAMAGE TO NICKEL-BASE ALLOYS

To test the hypothesis presented last quarter, that high temperature irradiation of Hastelloy X-280 in the solution-treated condition causes carbides to precipitate at irradiation damage sites within the matrix, specimens were solution-treated, cold-worked 26%, and then aged. Room temperature tensile tests showed increased strength and reduced ductility relative to controls. Micrographs show that heavy precipitation occurred along the strain lines of the cold-worked specimens and that grain boundary carbide precipitation was reduced.

Room tensile tests on Inconel X-750 in three heat treatments were made. Two double-age treatments differing in environment, cooling rate, and solution treatments showed significantly different properties, particularly in ductility. Micrographs indicate that both grain size and grain boundary carbide distribution differ in the two treatments.

DAMAGE MECHANISMS

The empirical relationship between strain rate and effective stress proposed in the last Quarterly Report has been modified. Analysis, based on this modified relationship, of a stress relaxation experiment yielded a theoretical expression which could be fitted to the experimental data by computer methods. Examples of the usefulness of the stress relaxation test are given. These afford insight into work hardening in body-centered cubic metals and in interpreting the strain rate sensitivity parameter. Derivation of equations unifying the concepts of dislocation dynamics and thermally activated flow are given. Discussion of dislocation multiplication effects is given and evidence is presented that dislocation density change occurs during stress relaxation and strain rate change tests. It is concluded that provisions in the theory should be made for changes in density of mobile dislocations if good agreement with experimental results is to be expected.

CHEMICAL METALLURGY

ENVIRONMENTAL EFFECTS

Additional data are presented on Zircaloy-2 corrosion confirming accelerated rates with normal fractional pickup of corrosion product hydrogen in the ETR G-7 540 F (280 C) water loop. Details of a scheduled two cycle experiment in the G-7 Loop are described, in which the effects of hydrogen addition to the loop water on zirconium alloy corrosion will be determined.

ATR GAS LOOP CORROSION STUDIES

Oxidation rates have been determined for Haynes Alloy 25 in 100 torr oxygen pressure at 2050 F (1120 C). Rates were less by a factor of 13 than at 2192 F (1200 C). In a vacuum of 10^{-4} torr, evaporation rates for Haynes Alloy 25 at 2050 F were one-third those at 2192 F (1200 C).

Additional sensitivity in the chromatographic analysis of impurities in helium gas has been achieved by optimizing column length and substitution of Linde 13X molecular sieve for the 5A grade. Calibration gas mixtures have been prepared in the new gas mixing facility. Extrapolation of peak heights obtained from three standard mixtures down to a value twice the instrument noise level, indicates detection limits for all gases (H_2 , O_2 , N_2 , CH_4 , CO , CO_2) of less than 1 ppm.

Oxidation studies of molybdenum and the molybdenum alloy TZM in 1000 C (1832 F) oxygen at 5×10^{-3} and 5×10^{-4} mm pressure are reported. Weight change data for the oxidized specimens are supplemented by direct measurement of metal loss based on an oxide stripping procedure. Oxidation rates are markedly reduced at the lower oxygen pressures, where formation of the volatile MoO_3 from MoO_2 is slower.

PRTR MATERIALS DEVELOPMENT

The thickness of oxide film on a discharged PRTR process tube has been determined metallographically for both irradiated portions and the unirradiated downstream end. Rates of film growth in-core appear to be about a factor of 5 greater than for the out-of-core sample. Corrosion of the tube interior exposed to hot D_2O and the tube exterior in a moist helium

environment is similar. Hydrogen analysis qualitatively indicates higher pickup for the irradiated portions of the tube.

Evidence pointing to the mechanical nature of film breakdown on corroding zirconium alloys has been obtained from two experiments. In one test thermal cycling was shown to precipitate rate transition at much lower weight gains than for a duplicate uncycled sample. In the second experiment premature breakaway was induced by mechanically flexing a sample over a cylindrical mandrel, then bending it back to shape. Subsequent weight gains of flexed samples were not affected unless a critical thickness of film was present.

The more important corrosion and hydriding characteristics of zirconium alloys are reviewed and interpreted in terms of the observed oxide properties. As the oxide thickness increases with time, associated progressive changes in oxide composition gradient occur which regulate transport processes through the oxide.

ADVANCED REACTOR CONCEPT STUDIES

Equilibrium and kinetic studies of the zirconium-hydrogen system have been undertaken to determine the feasibility of using a zirconium hydride moderator of variable hydrogen content as a means of reactor control. Hydrogen absorption and desorption curves were determined at 750 C (1385 F) in the composition range $\text{ZrH}_{0.28}$ to $\text{ZrH}_{1.63}$. Isotherms and phase relationships are compared with available published work. Since absorption and desorption processes approached 90% of equilibrium values in a matter of a few minutes, the variable composition hydride moderator appears to have promise.

PRODUCTION REACTOR CORROSION AND HYDRIDING

The investigation of velocity effects on aluminum corrosion in Columbia River water by the spinning disc technique has been directed to the synergistic effects of copper and chloride ion on pit initiation. The effects of pH in the range 3.2 to 7.8 on pit formation and metal loss were examined.

N REACTOR CORROSION AND HYDRIDING STUDIES

Refined experiments on the effect of thick oxide films on the hydriding behavior of Zircaloy-2 in dilute mixtures of H_2O , CO , and H_2 in helium are in progress. Corrosion rates are observed to fall off sharply with increasing film thickness from normal high pressure values. When corrosion rates are reduced samples are prone to hydriding. Recent experiments involving various hydrogen partial pressures indicate thick film also slows hydrogen penetration of the oxide.

MATERIALS ENGINEERING

PRTR PRESSURE TUBES

During this quarter 32 inspections were made in 29 process channels. New inspection probes were installed and employed in the inspections of the last 15 process channels.

PRTR Zircaloy-2 pressure tube testing has involved two room temperature burst tests of irradiated specimens, two room temperature crack propagation tests of unirradiated specimens, and an eddy current examination of a flaw in an irradiated tube. Post burst test examination is not complete. Burst strengths were $7,650 \text{ kg/cm}^2$ (108,600 psi) and $8,700 \text{ kg/cm}^2$ (124,000 psi) for an annealed and a cold-worked specimen, respectively. Cold-worked and annealed unirradiated specimens had identical Lamé hoop stress at crack propagation which, macroscopically, appeared brittle in both cases. Each specimen had a 9.65 mm (0.38 in.) long crack. The flaw location in one irradiated tube and the probable upper limit of its size was determined with the eddy current equipment.

N REACTOR PRESSURE TUBES

Slot type brittle fracture tests on N Reactor Zircaloy-2 pressure tubing have shown that increasing levels of hydride concentration cause an increasing sensitivity to larger defects. At room temperature and reactor operating pressure the crack length for instability in as-received tubing is greater than 50 cm (20 in.). This is reduced to 15 cm (6 in.) at 275 ppm hydrogen.

Initial tests on irradiated KER process tubing indicate little or no effect of irradiation on susceptibility to brittle fracture.

The Irradiated Tube Testing Facility has been in operation during the past quarter and seven tube sections have been burst tested. Tests on the furnaces have produced good temperature uniformity over the length of the test piece.

PHYSICAL METALLURGYNEUTRON DAMAGE TO METALS - H. E. Kissinger, J. J. Laidler,
B. Mastel, and J. L. Brimhall

This program is directed toward establishing the combined effect of impurities and neutron irradiation on the properties and structure of specific metals, and deducing from thermally-activated recovery processes how the damage state can be altered. Present studies involve single and polycrystalline specimens of molybdenum, nickel, and rhenium. Work to date has been concentrated on molybdenum, with the efforts on nickel and rhenium confined mainly to procurement, sample preparation, and development of associated experimental procedures.

Transmission Electron Microscopy

Studies of wafers cut from fractured single crystals of molybdenum have continued. One crystal, containing 450 ppm carbon which had been irradiated to 10^{18} nvt, was sectioned parallel to (110), the primary slip plane. Channels were not observed in any of the wafers cut from this crystal. In the gage section, where deformation was greatest, complex dislocation tangles were present. In some cases, the tangles developed subgrain boundaries. Radiation-induced defect structures in the form of small spots were observed. The concentration of the spots in the grip end of the specimen was approximately $10^{16}/\text{cm}^2$. In the deformed region of the sample the concentration was lower, indicating an interaction of the moving dislocations with the clusters. These observations are in agreement with those made on polycrystalline molybdenum foils which were irradiated to a similar exposure and deformed. The absence of channels in the foils and single crystals irradiated to this exposure is presumably due to an insufficient number of defects in the matrix. Glide dislocations are not restricted and slip occurs on a number of systems simultaneously. Higher exposures do create more defects, which in turn do restrict the number of active slip systems and produce channels.

Single crystals of molybdenum containing 20 and 450 ppm carbon which had been irradiated to 10^{19} nvt were also sectioned parallel to the (110) after fracturing and examined. The occurrence and distribution of channels is similar to those described in HW-81269. Straight line channels corresponding to traces of (110) and (112) planes were disclosed. In addition to the straight line channels, a number of curved and branching channels were also observed which are illustrated in Figure 3.1. If the curved channels are broken into straight line segments it is possible to index the traces with the aid of the diffraction pattern. The plane of the foil is close to (133). A stereographic projection of (133) is shown in Figure 3.2. The straight line segments appear to be parallel to traces of {110} and {112}, all of which have a common direction, namely $[111]$. Therefore, the observed traces may result from cross-slip on the four planes $(\bar{1}10)$, $(\bar{1}01)$, $(\bar{2}11)$, and $(\bar{1}2\bar{1})$ in the $[111]$ direction. Cross-slip of individual dislocations has been reported in deformed unirradiated polycrystalline foils of molybdenum by Benson, et al.⁽¹⁾ Therefore, it is not surprising to find evidence for cross-slip in the form of channel traces.

In addition to the channels, a high density of loop defects was observed in the micrographs. The loops were larger than those observed previously, approximately 400 Å in length, and their appearance is sensitive to the orientation of the crystal sections. In sections exactly parallel to (110) the loops appear to be elongated, but for orientations near (331), 13 degrees from (110), the loops appear as straight parallel lines. In all cases, the long axes of the loops are perpendicular to $[111]$ directions. It is possible that prismatic glide of a closed dislocation loop has occurred. Under suitable stress the loop may form an elongated loop similar to those observed. A detailed analysis of these micrographs is in progress.

-
1. R. Benson, G. Thomas, and J. Washburn. "Dislocation Substructures in Deformed and Recovered Molybdenum," Direct Observation of Imperfections in Crystals, edited by J. B. Newkirk and J. H. Wernick, Interscience Publishers, New York, 1962. pp. 375 to 391.

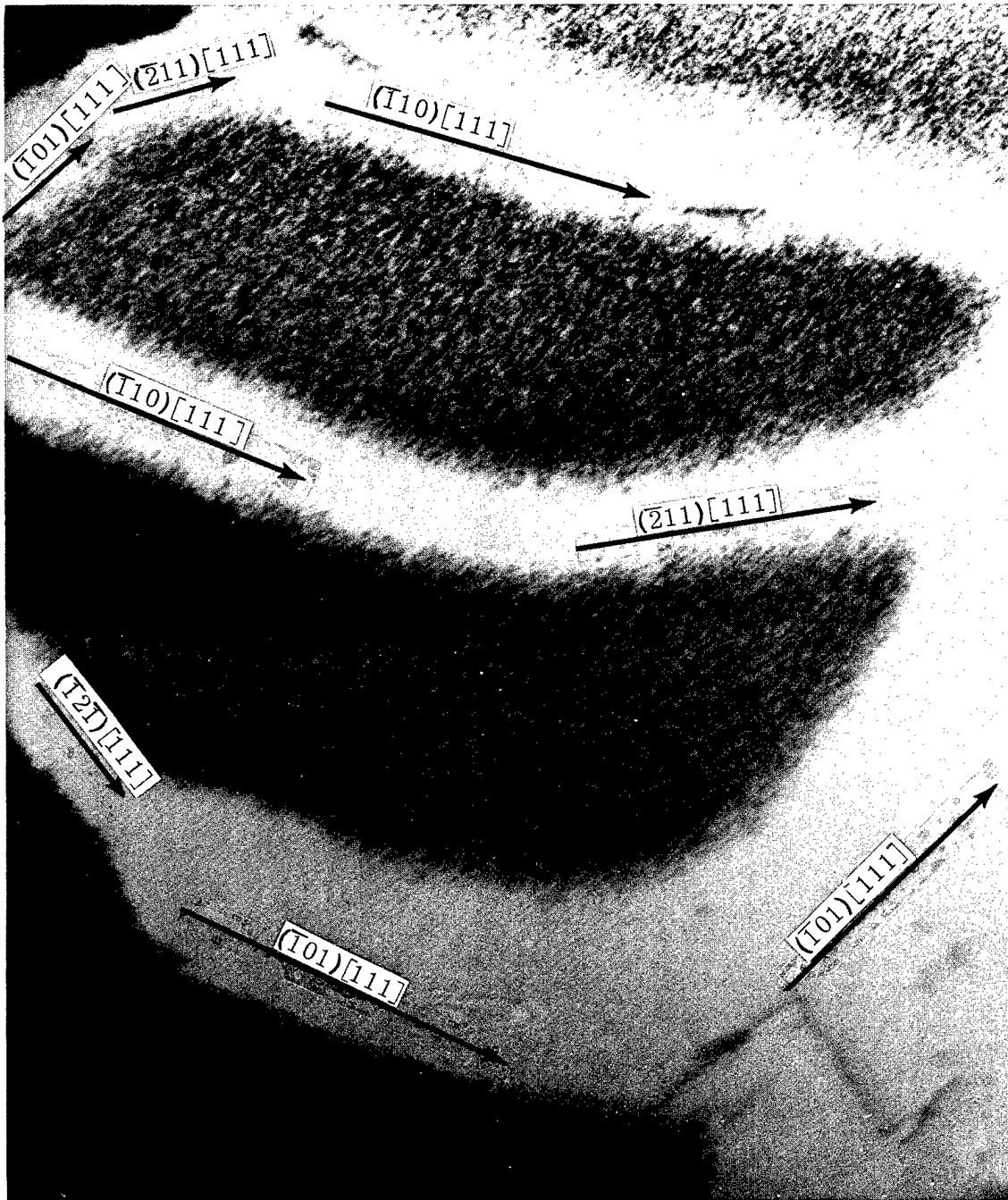


FIGURE 3.1

Curved and Branching Channels Present in a Single Crystal
of Molybdenum after Irradiation and Straining

Neg. No. 2627C

2700X

AEC-GE RICHLAND, WASH.

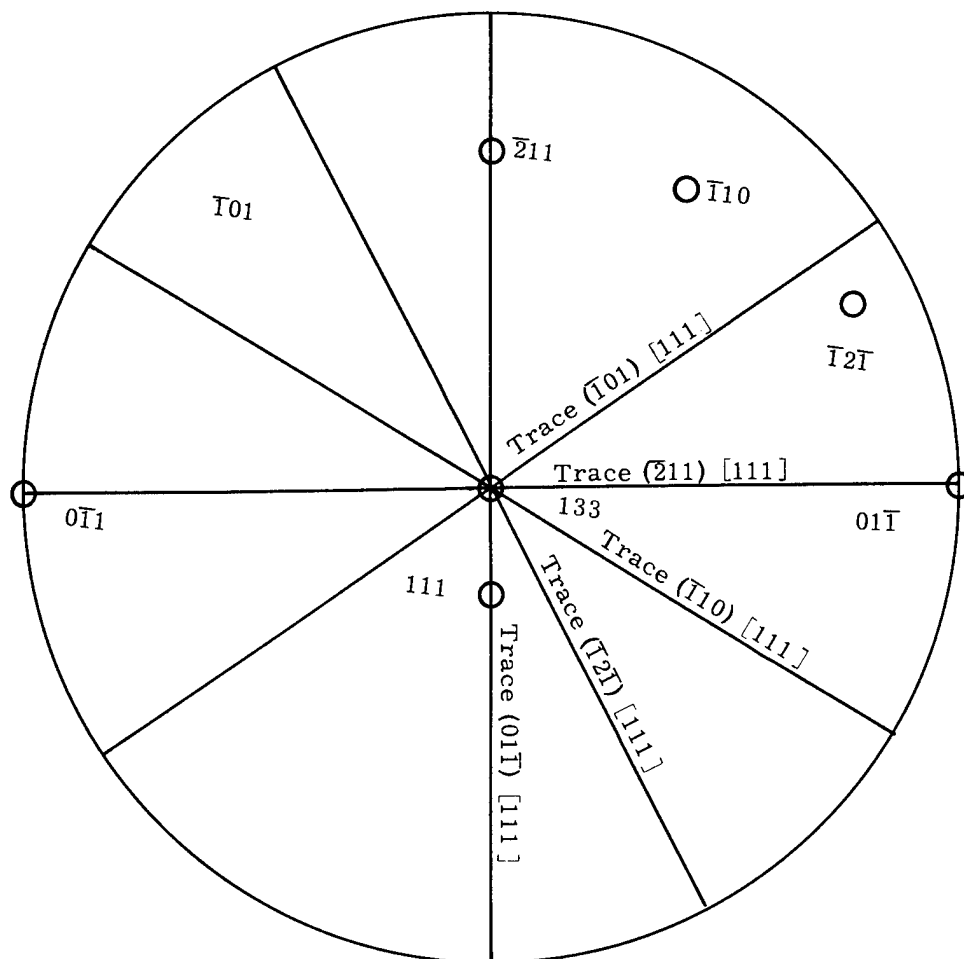


FIGURE 3.2

Stereographic Projection on (133),
Showing Possible Origin of Channels in Preceding Figure

In order to determine if the formation of channels is a unique deformation mode of irradiated body-centered cubic metals, high-purity copper (a face-centered cubic metal) was irradiated to 10^{19} nvt (fast). Transmission electron microscopy revealed defects in the form of small spots and larger prismatic dislocation loops. The irradiated foils were deformed approximately 2% in tension and examined. Channels similar to those observed in molybdenum were observed in the deformed foils. Several micrographs and accompanying diffraction patterns have been analyzed and show that the channels correspond to traces of the (111) on the plane of the foil. This result was expected as the (111) is normally the slip plane in face-centered cubic metals. Figure 3.3 is a transmission micrograph of such

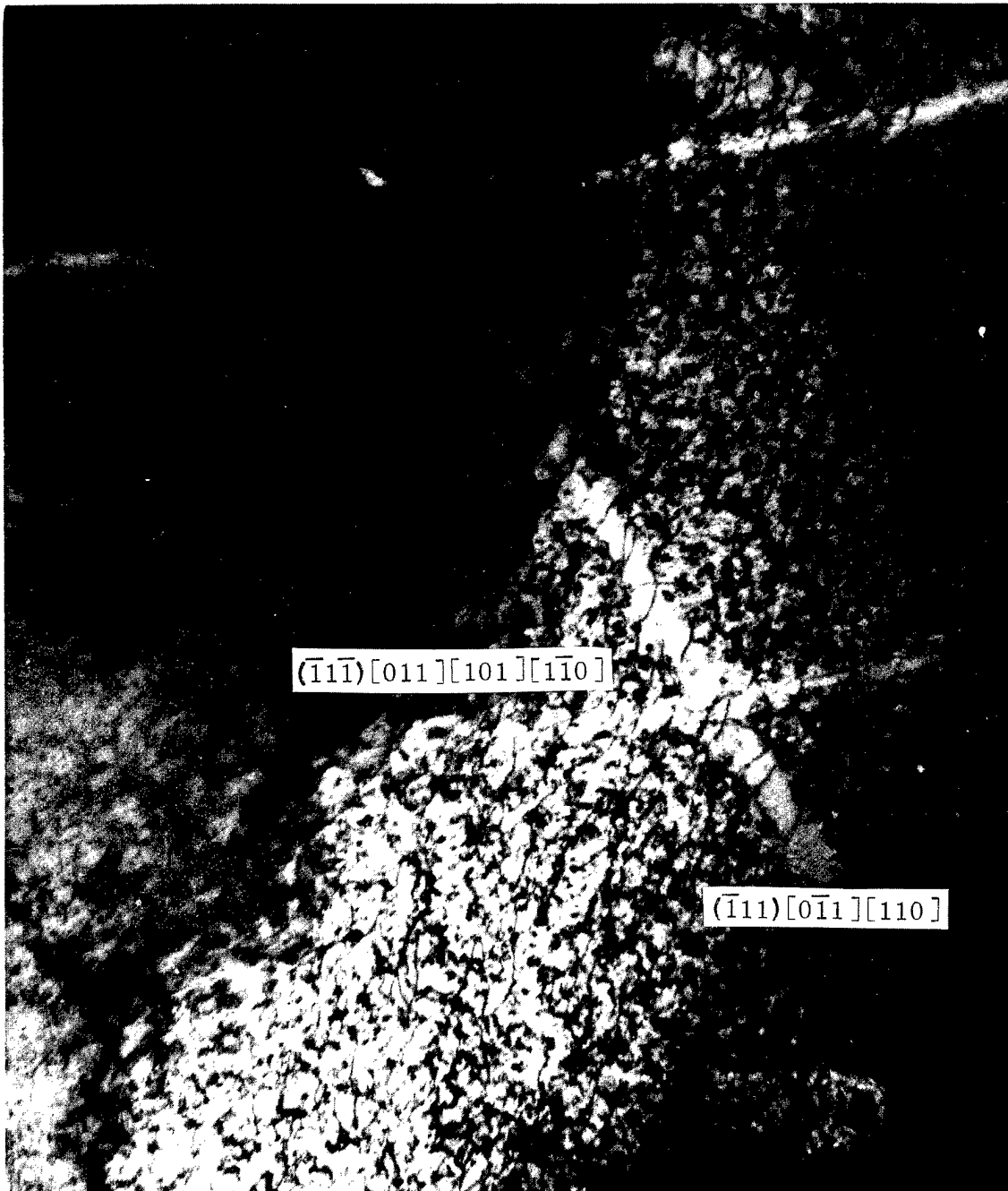


FIGURE 3.3

Channels and Defect Clusters Present in Irradiated Copper
after an Exposure of 10^{19} nvt and Deformation of 1 to 2%
Neg. No. 2603C 30,000X

AEC-GE RICHLAND, WASH.

a foil, the orientation of which is close to (101). Complex dislocation networks exist between the channels. This observation is contrary to that made on molybdenum foils where dislocations are seldom observed outside of the channels. This suggests that more slip systems are operating in the face-centered cubic metals than in body-centered systems. However, the existence of channels in both metals suggests that the deformation process in irradiated face-centered and body-centered cubic metals is similar. The results on copper substantiate work reported in the literature, namely, that channels in irradiated, deformed copper single crystals have been observed and the channels correlated with external slip traces.⁽¹⁾

Slip Line Study

In conjunction with the electron microscopy of irradiated molybdenum, the slip line structure is currently being studied. Deformation is carried out by bending and both optical and replica electron microscopy are being used.

One irradiated crystal has been studied to date. Figure 3.4 shows the orientation of the crystal with respect to the bending loads and the orientation of the observed slip lines.

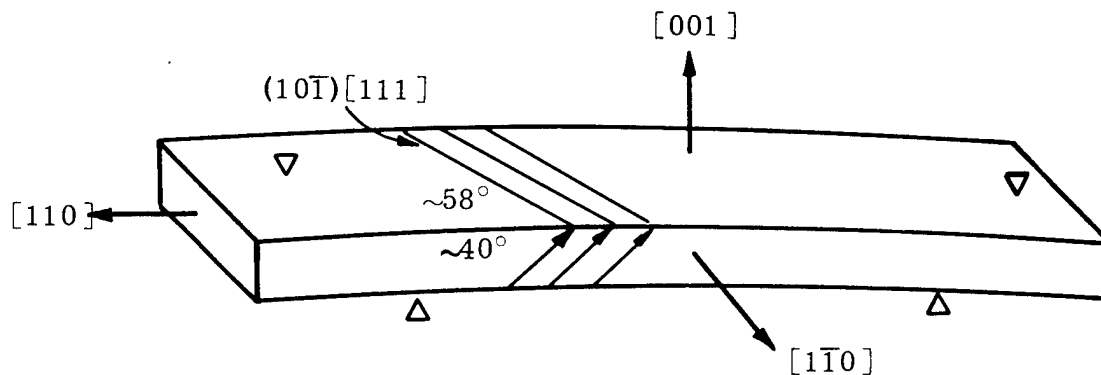


FIGURE 3.4

Diagram of Operative Slip System for Crystal Orientation as Shown
(The principal operative slip system was found to be $(10\bar{1})[111]$)

-
1. I. G. Greenfield and H. G. F. Wilsdorf. "Observations Concerning Radiation Hardening in Copper and Nickel," Naturwissenschaften, vol. 47, pp. 395 to 396. 1960.

Figures 3.5 and 3.6 show the slip line structure on the two adjacent faces. During deformation, most of the bending occurred at one point and it was not possible to obtain a good quantitative relation between degree of strain and slip line appearance.



FIGURE 3.5

Slip Lines on (001) Face
of Irradiated Molybdenum Single
Crystal Deformed by Bending
(110) Specimen Axis
130X

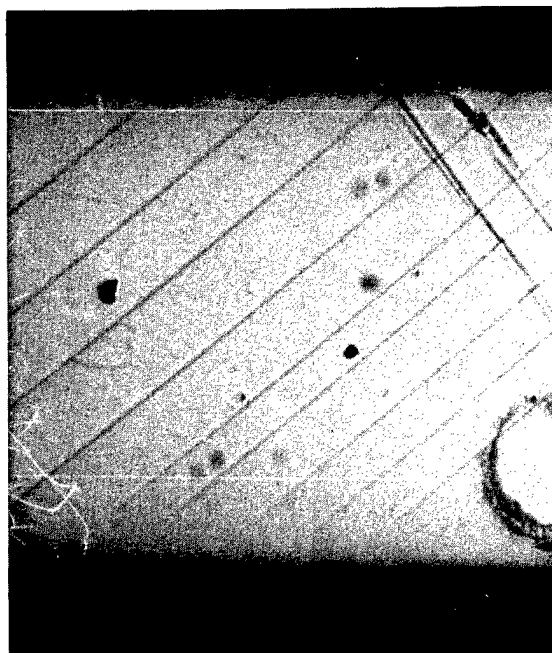


FIGURE 3.6

Slip Lines on ($\bar{1}\bar{1}0$) Face
of Irradiated Molybdenum Single
Crystal Deformed by Bending
(110) Specimen Axis
130X

The slip lines appear very faint on the ($\bar{1}\bar{1}0$) face as the $[111]$ direction lies parallel to this ($\bar{1}\bar{1}0$) plane. In contrast, the $[111]$ direction makes an angle of approximately 55° with the $[001]$ plane; hence, the offset and slip lines are much more pronounced on the (001) face. Also seen on the (001) face are faint, interconnecting, wavy lines between the long predominant slip lines. There is no hint of these on the ($\bar{1}\bar{1}0$) face but probably are due to small amounts of slip on a major secondary system.

In the replicas, the coarse slip lines appear as broad, smooth bands, as shown in Figure 3.7. The bands appear light or dark depending on whether the slip step is facing the direction of the shadowing material. In contrast to the coarse lines, the faint lines on the $(1\bar{1}0)$ face seen in Figure 3.6 also appear as very faint bands in the replicas, Figure 3.8. Shadowing does not bring out the slip line to any significant degree.

It can also be shown with reference to Figure 3.9 that these slip lines, such as in Figure 3.7 represent the offset from slip on a number of neighboring planes rather than from one $(10\bar{1})$ plane. This can be done by calculating the slope of the slip step from the change in shadow length of the latex balls when they lie near slip lines.

From an analysis of the micrographs as in Figure 3.7, ϕ varies from 25° to 35° which is significantly less than 45° . This indicates that the slip lines are in fact a collection of closely spaced slip lines. Individual steps could not be resolved on the broad lines possibly because the steps are near monotonic in height.

The irregular profile of the lines as seen in the replica could arise from dislocation gliding on different $(10\bar{1})$ planes at different segments along its length.

The number of dislocations contributing to the slip line can also be calculated by knowing the line width and slope of the step, as shown in Figure 3.10.

For the slip line shown in Figure 3.7, n is calculated to be approximately 5000 dislocations. In light of the concentrated nature of dislocation movement in the irradiated material, this is not an unreasonable value.

The relatively large value of n , large width of the bands, and their general appearance support the conclusion that the slip lines result from the dislocations moving through the channels. From the true width w and spacing of the lines, it should be possible to correlate the lines directly with the channels. Thin sections cut perpendicular to the slip planes and observed in transmission are required. In future bend experiments, it will be ascertained how the depth and number of the slip lines varies as a function of strain. Correlations will also be made with unirradiated crystals of the same orientation.

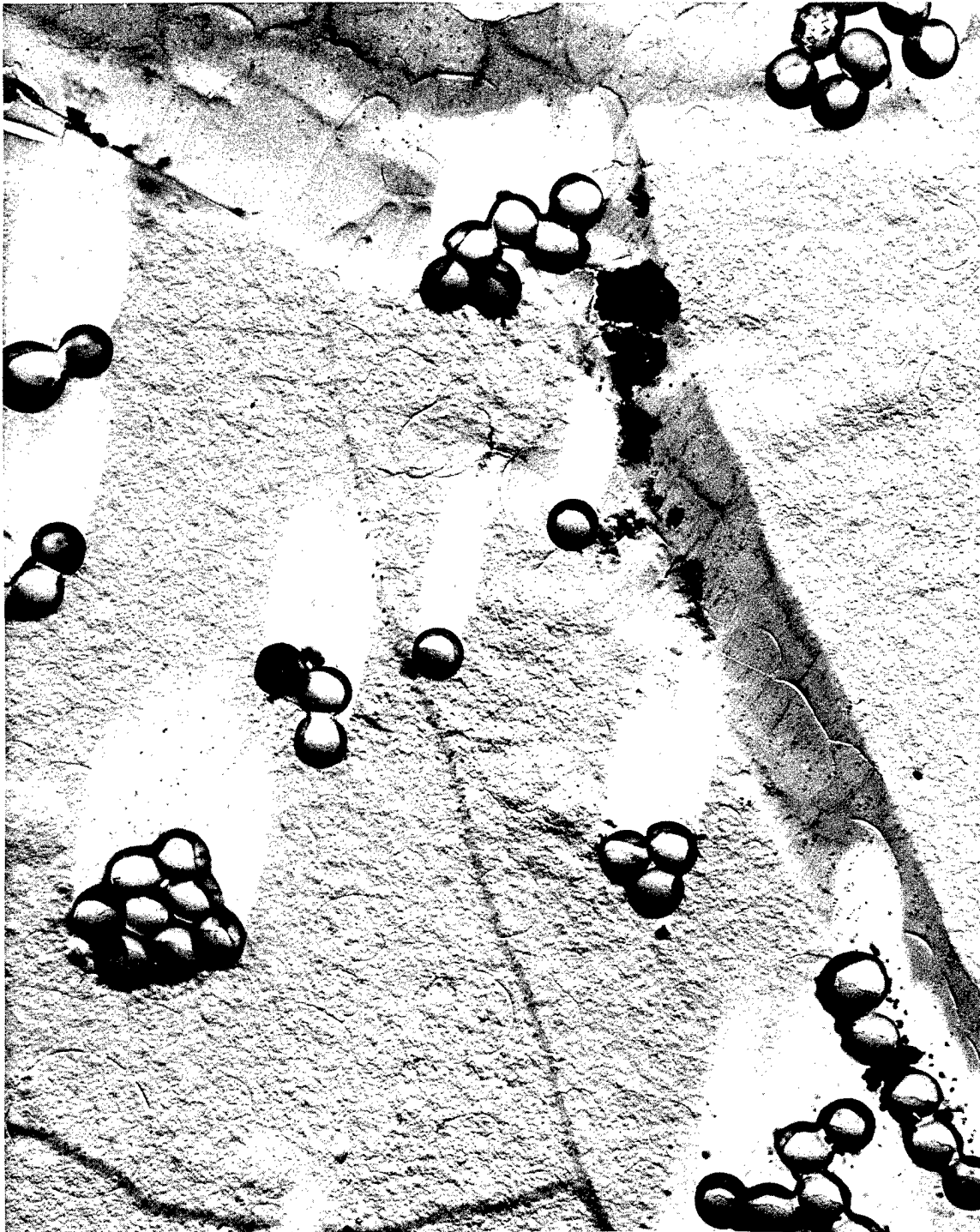


FIGURE 3.7

Replica of the Slip Line Structure
from the (001) Face as Seen in Figure 3.5
9000X

Neg. No. 32 C

AEC-GE RICHLAND, WASH.



FIGURE 3.8

Replica of the Slip Line Structure
from the $(1\bar{1}0)$ Face as Seen in Figure 3.6
9000X

Neg. No. 31B

AEC-GE RICHLAND, WASH.

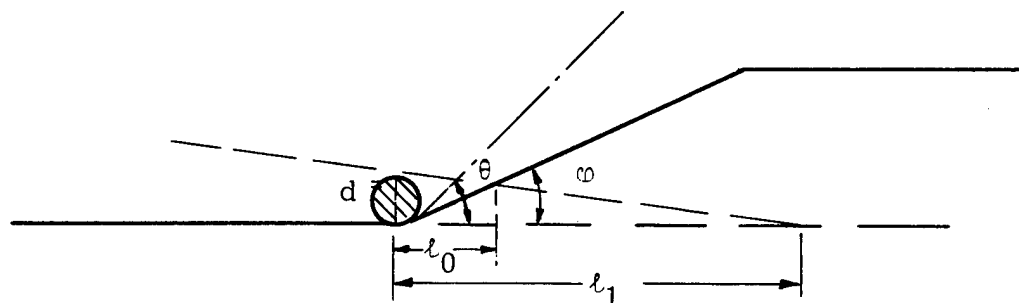


FIGURE 3. 9

Diagram for Evaluation of Slope of Slip Offset

θ = Angle between slip plane and surface = 45°

φ = Angle between slip line and surface

l_0 = Length of shadow with slip step

l_1 = Length of shadow without slip step

d = Diameter of latex ball

$$\tan \varphi = \frac{(l_1 - l_0)d}{l_1 \sqrt{l_1^2 - d^2}}$$

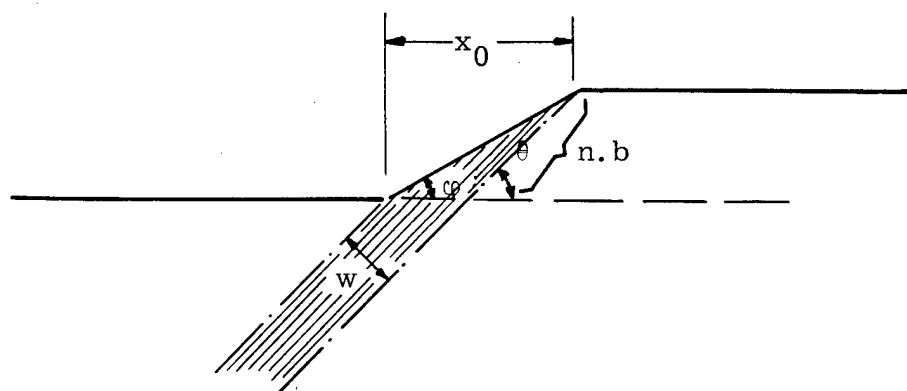


FIGURE 3. 10

Diagram for Evaluating Slip Height

$$n.b = x_0 \frac{\tan \theta}{\sin \theta}$$

where n = Number of dislocations producing offset

b = Burgers vector

x_0 = Width of slip line measured on micrograph

X-Ray Diffraction

The technique which has been employed for X-ray lattice parameter measurement on single-crystal specimens apparently provides an accuracy of 0.001%. To verify this conclusion, a single crystal of semiconductor grade silicon was obtained. A (111) face was cut, the crystal was etched, and X-ray measurements were made on this face. The experimental procedure was the same as described in previous reports (HW-77052, HW-81269). Copper $K\alpha_1$ and $K\alpha_2$ radiations were used to obtain the (444) reflection at approximately $160^\circ 2\theta$. Because of the very sharp diffraction maxima, no correction for the variation of Lorentz polarization factor with angle was needed. Five measurements for each wave length yielded an average lattice parameter for silicon of 5.43046 \AA , ± 0.00006 , which may be compared with the value of 5.43050 \AA obtained by Vogel and Kempter [Acta Crystallographica 14, 1130 (1961)] in a precision measurement by the powder method. The observed standard deviation, 0.00006 \AA , is in agreement with the previously claimed precision of 0.001% in these measurements.

A single crystal of rhenium was sectioned parallel to (100) and to (001) for precision lattice parameter measurements. Sections were cut with a water-cooled diamond saw blade and the resulting surface electropolished in a HNO_3 solution to remove cold work. The crystal sections were then used to determine lattice spacings by the symmetrical back-reflection method, using the (300) reflections at $2\theta = 150.3^\circ$ and 151.4° (copper $K\alpha_1$ and $K\alpha_2$) and the (006) reflection at 139.9° (copper $K\beta$). Lattice parameter values, not corrected for refraction, are $a_o = 2.7604 \text{ \AA}$, $c_o = 4.4599 \text{ \AA}$, with $c/a = 1.6157$. These may be compared with corresponding values of 2.760 \AA , 4.458 \AA , and 1.615 reported by Campbell, et al. ⁽¹⁾

Lattice parameters of high-purity rhenium foils were desired as part of the preirradiation characterization. The annealing treatment, however, produced very large grains in the foils so that conventional X-ray diffractometry was all but impossible. A modified technique was employed in which an

1. I. E. Campbell, D. M. Rosenbaum, and B. W. Gonser. J. Less Common Metals, vol. 1, pp. 185 to 191. 1959.

individual grain was oriented in diffracting position. Without changing the sample orientation, the $K\alpha_1$, $K\alpha_2$, and $K\beta$ peaks of the copper spectrum were obtained for the (105), (204), and (300) reflections, all of which appear at relatively high angles. Data obtained for a number of sample positions was then refined by plotting the observed d-values against $\cos^2 \theta$ and extrapolating to $\theta = 90^\circ$. In all cases, the plots converged to essentially a unique value for each d-spacing, as shown in Figure 3.11. Final values were $d_{105} = 0.83543 \text{ \AA}$, $d_{204} = 0.81512 \text{ \AA}$, and $d_{300} = 0.79668 \text{ \AA}$. These data were then used to compute lattice parameters by first determining a_0 from the (300) d-spacing, then using this value of a_0 to determine c_0 from the (105) and (204) d-spacings. Also, c_0 and a_0 were computed directly from the (105) and (204) d-spacings. The results are summarized in Table 3.1.

TABLE 3.1
LATTICE PARAMETER OF RHENIUM

<u>Source</u>	<u>Result</u>
(300)	$a_0 = 2.7598 \text{ \AA}$
(105), (300)	$c_0 = 4.4587 \text{ \AA}$
(204), (300)	$c_0 = 4.4584 \text{ \AA}$
(105), (204)	$c_0 = 4.4583 \text{ \AA}$
(105), (204)	$a_0 = 2.7600 \text{ \AA}$
Average $a_0 = 2.7599 \text{ \AA}$	
$c_0 = 4.4585 \text{ \AA}$	
$c/a = 1.6155$	

These results indicate that the a_0 dimensions of the polycrystalline sample and the single crystal are essentially identical while the c_0 dimension is somewhat greater for the single crystal. Quite possibly the single crystal surface was not completely free of cold work. Another possibility is a difference in purity between the samples.

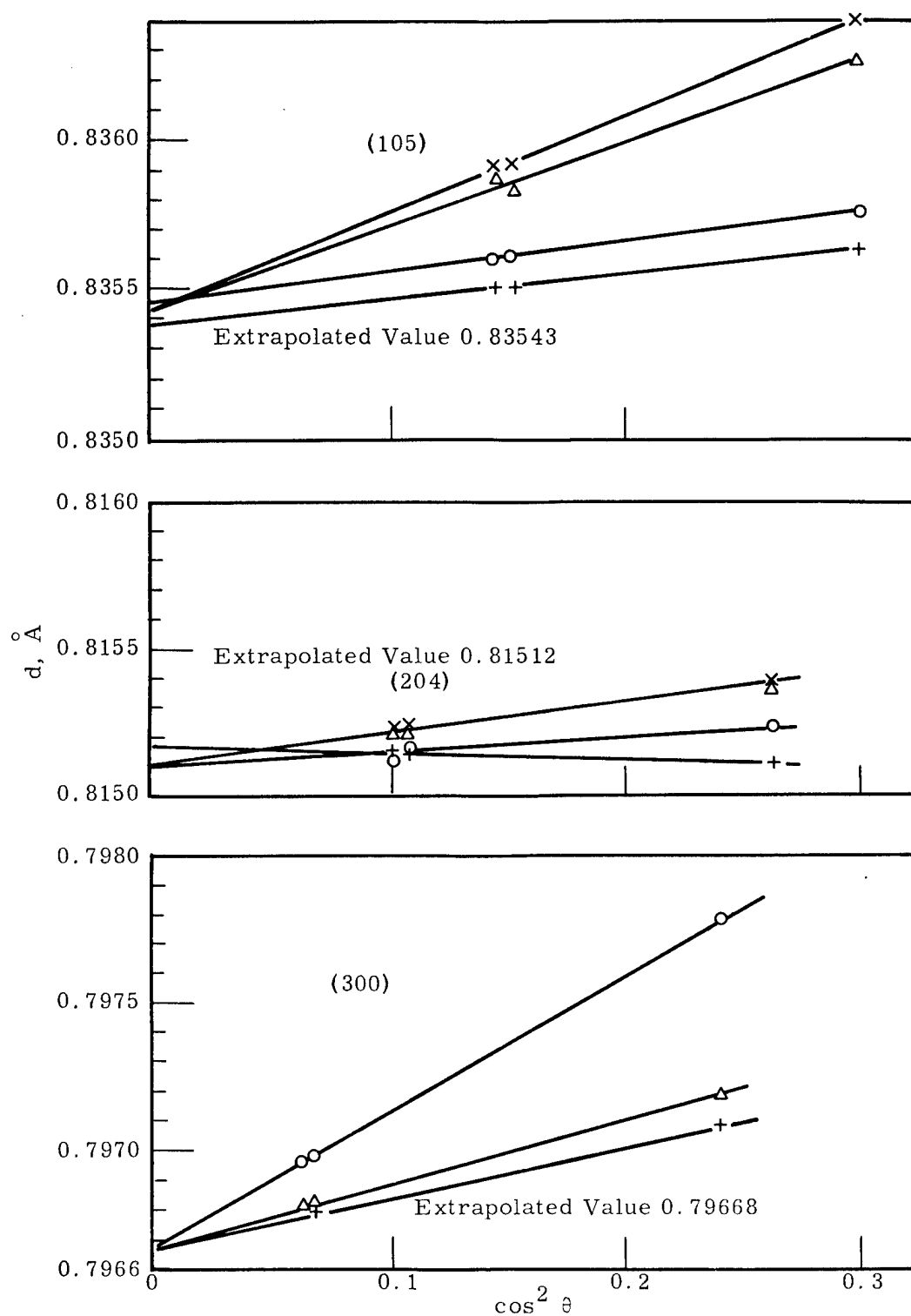


FIGURE 3. 11

Graphical Determination of Precision Lattice
Spacings for Rhenium

SWELLING OF IRRADIATED FISSIONABLE MATERIALS - R. D. Leggett,
B. Mastel, Y. E. Smith, and J. W. Weber

When fissionable metals are irradiated, the ordered metallic structure is perturbed in a number of ways. High energy neutrons and fission fragments collide with metal atoms, knocking them out of their structural positions. The resultant defects, vacancies, interstitials, dislocation loops, etc. can adversely affect metallic properties. Similarly, the fission products generated, some of which are noble gases, may be incompatible with the structure and so precipitate or coalesce as second phase inclusions or gas pores. Furthermore, the high localized temperatures associated with the fission event can cause anisotropic fissionable metals such as uranium to drastically change shape in accordance with the crystallography of the specimens. These effects and their interactions are being studied with regard to the influence of irradiation variables such as the specimen temperature, burnup, burnup rate and external pressure, and of metallurgical variables such as composition, structure, and geometry. The primary emphasis to date on this program has been that of determining the basic processes responsible for the behavior of uranium irradiated at temperatures in the high alpha, where swelling is known to be important. Fundamental information developed by this program will provide a basis for engineering exploitation of the many beneficial attributes of metal fuels for use in reactor applications.

Irradiation Program

Two irradiation test capsules were discharged from the reactor after reaching their respective goal exposures. One capsule containing high-purity uranium specimens of varying specimen geometry was irradiated in the beta phase region at 700 C (1292 F). The second capsule contained enriched uranium specimens and, therefore, was fitted with eight heat transfer fins between the inner and outer chamber instead of the usual six in order to allow removal of the additional fission heat. However, the required level of heat transfer was not realized in the bench test. In order to further increase the overall heat transfer coefficient of the capsule, the end cap was

temporarily removed and 0.032 in. diameter stainless steel, chopped wire pellets were poured in to fill the annulus between the inner specimen tube and the outer tube wall. The increase in heat transfer capability is illustrated by the power temperature curves of Figure 3.12 which were obtained during bench tests before and after adding the stainless steel pellets to the annulus. This capsule was operated in-reactor at 400 C (752 F). Both of these capsules were controlled at constant temperature by the recently installed solid state three mode control system. This system has performed without difficulty since its installation.

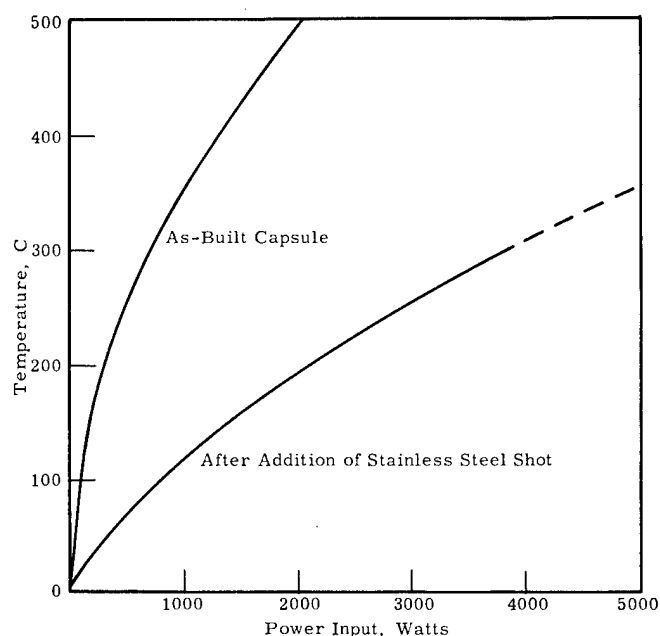


FIGURE 3.12

Heat Transfer Characteristics of a General Swelling Capsule
Before and After Modification by the Addition of Stainless Steel Shot

The prototype high pressure irradiation capsule was completed and processed through out-of-reactor tests. The capsule is designed for controlled temperature irradiations at up to 140 kg/cm² (2000 psi) and 700 C (1292 F). The three prime considerations involved in the design of this capsule were: • pressure containment capability at high temperatures; • capability of conforming to changes in NaK volume; and • sufficient heat transfer capability without excessive power requirement. The capsule was

designed in accordance with the cold wall autoclave principle as discussed in HW-76228.⁽¹⁾ The outer pressure containment wall is constructed of AISI 316 SS, with the allowable stress level selected on the basis of a maximum allowable inner wall temperature of 400 C (752 F).

The design of the prototype test capsule included an additional modification to the NaK expansion chamber region as presented in HW-79766.⁽²⁾ The length of the capsule and the NaK expansion bellows shield was extended several inches to make room for a slide-wire resistance type linear displacement transducer. The transducer yields a 0 to 10 v linear output for a 2.25 in. range of displacement of the end of the expansion bellows.

The following series of three tests were conducted in a high pressure testing facility in order to establish that the capsule met the three primary design objectives:

- The pressure was increased in a stepwise manner at ambient temperature and the corresponding compression of the NaK expansion bellows was recorded.
- The capsule was isolated from the pressurization system at two atmospheres of helium pressure and the temperature was incrementally increased. Temperatures, bellows position, and power input data were recorded. In addition to the specimen chamber temperature, the inner wall temperature at a point between the heat transfer fins and, also, the temperature of the aluminum case of the displacement transducer were recorded.
- On attaining the maximum temperature possible with the power supply available, the pressure was incrementally increased to the 140 kg/cm² (2000 psi) design pressure* and data was recorded as in the above test.

-
1. Quarterly Progress Report - Metallurgy Research Operation - October, November, December, 1962, edited by J. J. Cadwell, HW-76228. January 15, 1963.
 2. Quarterly Progress Report - Metallurgy Research Operation - October, November, December, 1963, edited by J. J. Cadwell, HW-79766. January 15, 1964.

* This particular capsule is designed for in-reactor operation at 140 kg/cm² (2000 psi). Therefore, to be consistent with standard practice it must be proof-tested at 210 kg/cm² (3000 psi). A pressurization system which is currently on order will have this capability. The above testing pressure is more than adequate for the first irradiation test which will be conducted at 70 kg/cm² (1000 psi).

The results of this series of tests indicated that the capsule met all three primary design objectives. Figure 3.13 presents the compression of the bellows as a function of pressure at ambient temperature. The total decrease in volume of the specimen chamber was 4.7 cm^3 , which is approximately equal to the standard cm^3 of helium trapped in the chamber.

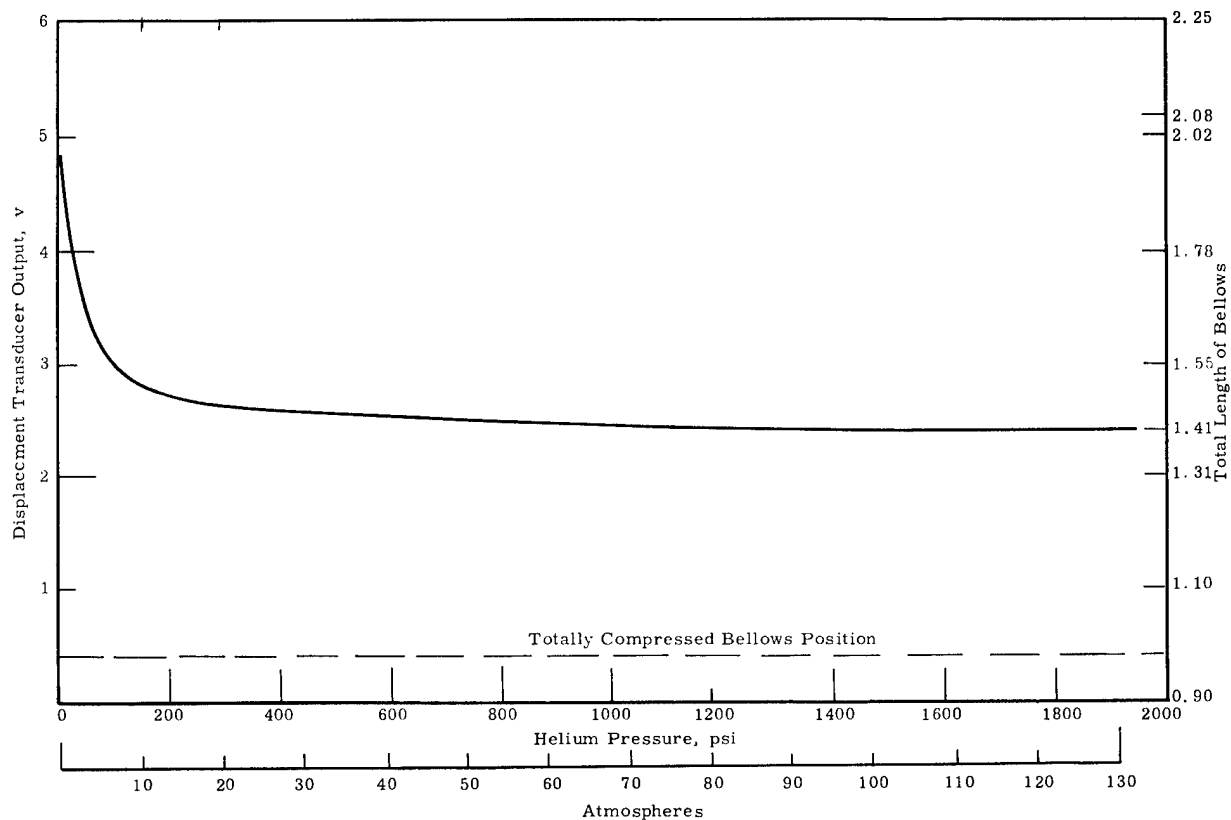


FIGURE 3.13

Compression of Bellows on Initial Increase
of Pressure on Prototype High Pressure Irradiation Capsule

The maximum specimen chamber temperature, inner wall temperature of the pressure containment vessel, displacement transducer temperature and bellows extension position during the final test run are presented in Figure 3.14. The incremental increase of power input is reflected in all of the curves. The reaction of the system to pressurization was similar to that at ambient temperature in that significant compression occurred on the

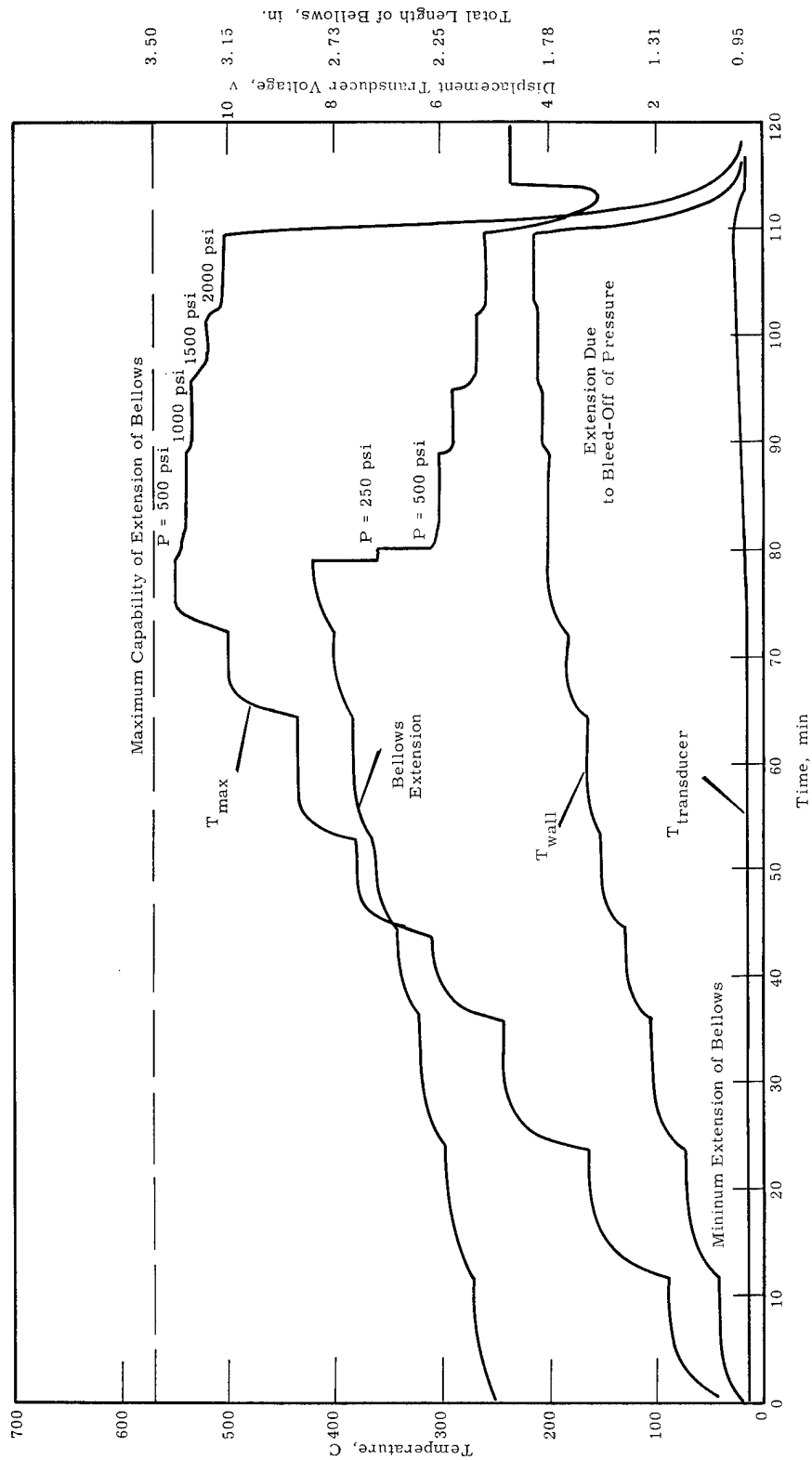


FIGURE 3.14

Maximum Specimen Chamber Temperature, Internal Wall Temperature
Displacement Transducer Temperature and Bellows Extension During
Second Test Run of Prototype High Pressure Irradiation Capsule

initial increases in pressure and only moderate volume changes took place thereafter. Pressurization also resulted in minor adjustments in heat transfer characteristics.

The power input versus temperature curve from the design calculations is presented in Figure 3.15. Data points have been plotted for the two low pressure check out runs. The power curve at high pressure would be altered slightly, as indicated by the deviation of T_{\max} as a function of pressure in Figure 3.14.

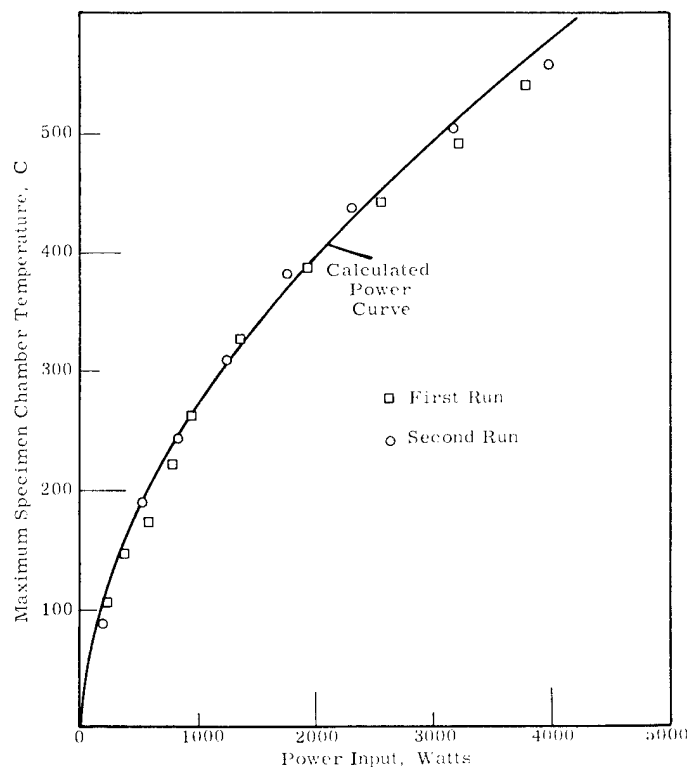


FIGURE 3.15

Heat Transfer Characteristics
of the Prototype High Pressure Irradiation Capsule

On the basis of the success of this prototype test, the capsule for the first in-reactor test has been constructed in accordance with this design. One minor modification was introduced. Namely, the heat transfer fins were changed to stainless steel in place of nickel in order to reduce the power requirement during high temperature tests. This capsule is currently undergoing preirradiation testing.

Postirradiation Examination

[A general swelling capsule, No. 26, (containing half-tubular specimens of high-purity dingot uranium, ingot uranium with small additions of iron and silicon, and ingot uranium with additions of iron and aluminum) was examined] opened in Radiometallurgy and the specimens recovered. Several metallurgical states were also represented for each composition. [The capsule was irradiated at a control temperature of 575 C (1067 F) to a burnup in the specimens of 0.11 at.% (5.2×10^{19} fission/cc).] The composition, preirradiation heat treatment, irradiation temperature, as-irradiated density and the calculated volume increase are indicated for each of the eight specimens in Table 3.2. The macro appearance of these samples is shown in Figure 3.16. The volume changes calculated from the density measurements for the most part corroborate the macro appearance. The accuracy of the reported values is better for the "A" and "D" specimens than for the "B" and "C" specimens because the magnitude of the observed swelling and the surface roughing is less in the former case. Sample C-1, for example, has holes extending completely through the thickness of the specimen where the large grains have fallen out. The estimates of the volume increase experienced by this sample are probably low due to the internal wetting of holes and cracks by the immersion fluid used in the density determinations.

The marked influence of composition and heat treatment on the innate irradiation behavior of uranium is quite obvious. [The specimens of the U + Fe-Al alloy were far superior to the other specimens in both of the metallurgical states represented in this capsule. Furthermore, there was an apparent improvement due to a gamma annealing treatment prior to quenching from the beta phase](A-1 specimen compared with D-1 specimen). [Specimens of the U + Fe-Si alloy (A-2 and D-2) behaved significantly better than the high-purity uranium specimens but not nearly as well as the U + Fe-Al alloy specimens.] ^{4.3.22 copy to p. 338} U + Fe-Si alloy specimens also appeared to derive some benefit from a gamma treatment prior to the beta quench. With regard to this gamma-beta treatment, it should be borne in mind that the "D" specimens which received only the beta treatment were heat-treated in a bulk form and then

TABLE 3.2
IRRADIATION HISTORY AND VOLUME CHANGE
OF SPECIMENS* IN CAPSULE 26

Specimen Number	Type Material**	Heat Treatment	Irradiation Temperature		As-Irradiated Density ρ_i , g/cc	Swelling, % $\frac{\rho_i - \rho_f}{\rho_f} \times 100$
			Reactor Up, C	Reactor Down, C		
A-1	U + Fe-Al	800 C, 2 hr, Furnace Cooled 730 C, 15 min, Oil Quenched	535	565	18.9	0
A-2	U + Fe-Si	800 C, 2 hr, Furnace Cooled 730 C, 15 min, Oil Quenched	535	565	17.5	8
B-1	High-Purity U	As Extruded	585	575	15.3	24
B-2	High-Purity U	730 C, 15 min, Oil Quenched	585	575	15.6	22
C-1	High-Purity U	730 C, 15 min, Furnace Cooled	575	575	13.9	37
C-2	High-Purity U	900 C, 15 min, Furnace Cooled	575	575	15.4	24
D-1	U + Fe-Al	Beta Quench***	535	535	18.3	3
D-2	U + Fe-Si	Beta Quench***	535	535	16.8	13

* Specimens were half, hollow cylinders, 10 mm OD x 15 mm long x 1 mm wall thickness

** Composition in ppm: U + Fe-Al: 400 Fe, 640 Al, 85 Si, 500 C

U + Fe-Si: 140 Fe, ~25 Al, 95 Si, 400 C

High Purity U: 65 Fe, <5 Al, 24 Si, 6 C

*** Beta Quench - Large bulk specimen heated to 730 C (1346 F) in a salt bath and quenched into water prior to machining specimens

Exposure: 0.11 at. % burnup (5.3×10^{19} fissions/cc)

3.23

HW-82651

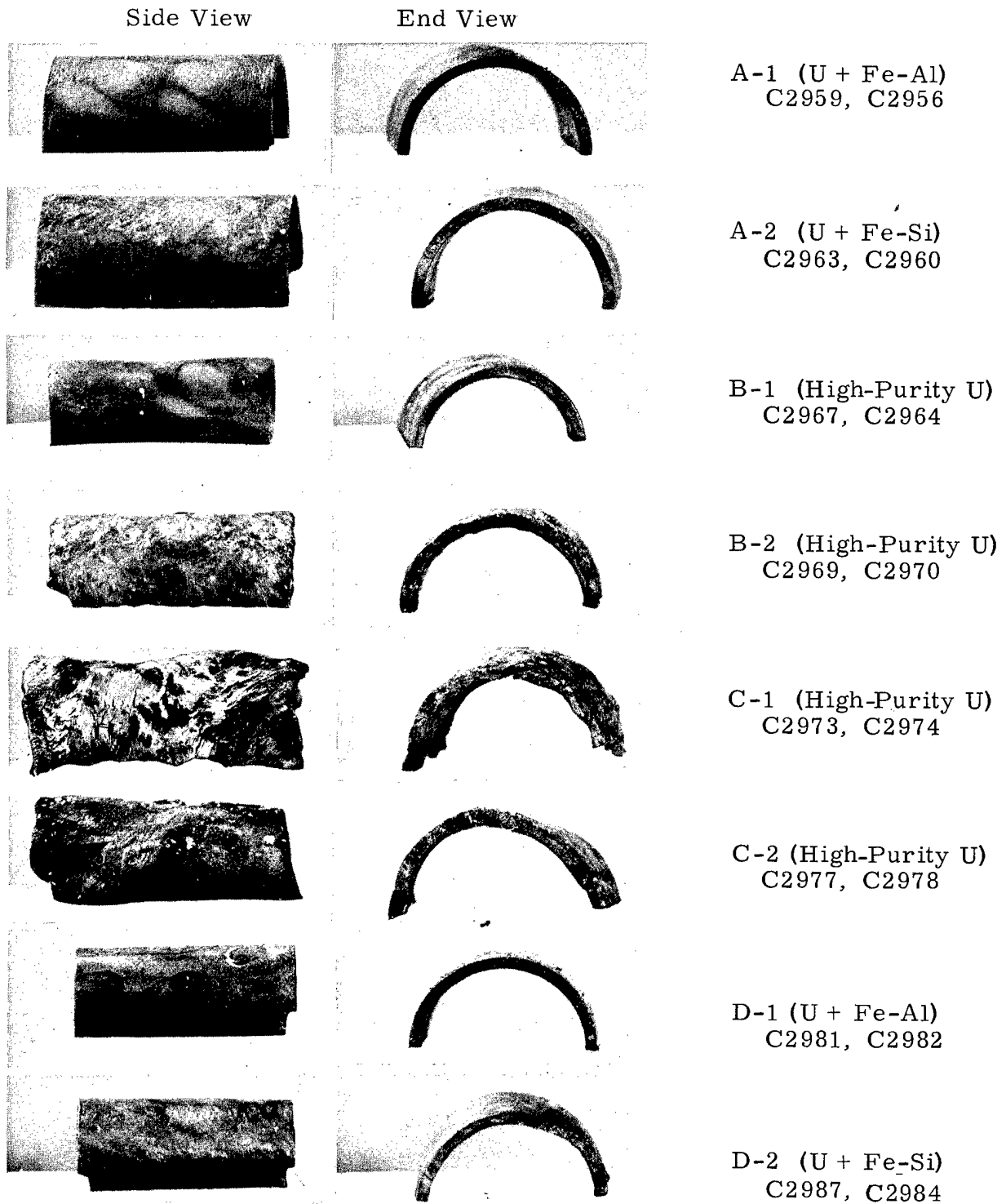
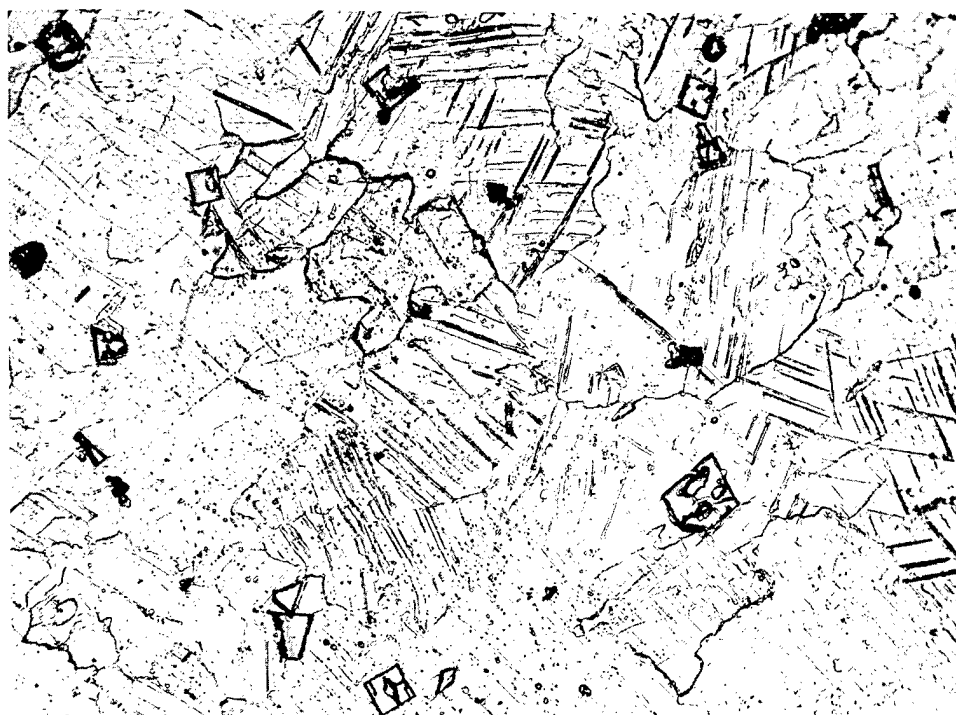


FIGURE 3.16

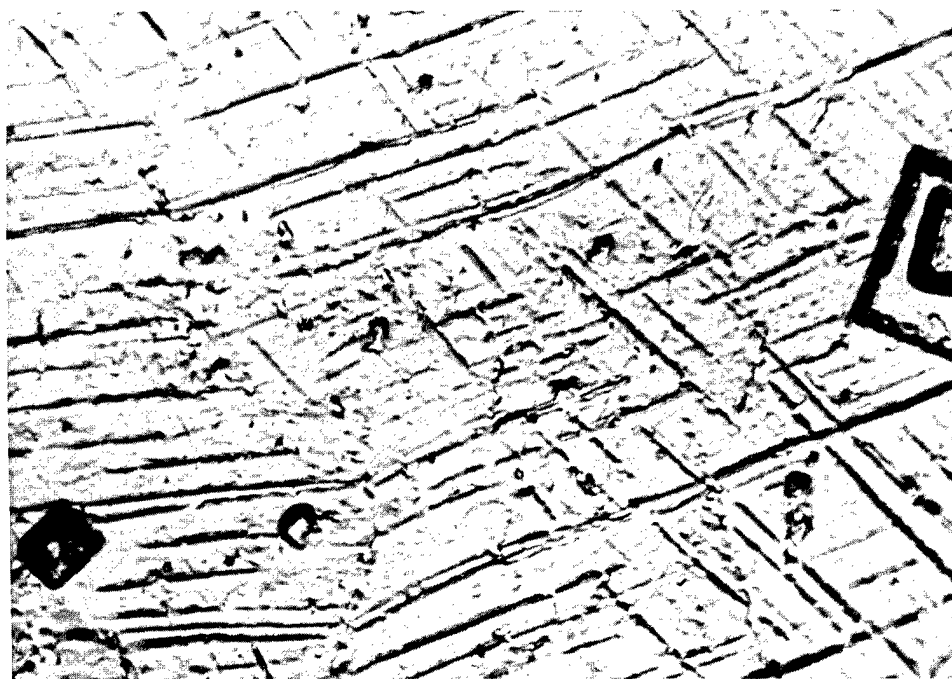
As-Irradiated Macro Appearance
of Specimens Irradiated in Capsule 26
2X

machined into specimens, whereas the "A" specimens were first machined and then gamma-beta treated. The differences in cooling rate and residual machining stresses may also be exerting a minor influence on these observations.

The observations of porosity in the optical and electron microscopes qualitatively corroborated the measured density changes. Figures 3.17 and 3.18 reveal the as-irradiated appearance of the U + Fe-Al specimen (A-1) that had received the gamma-beta treatment prior to irradiation. Except for possible broadening of twin bands there were no obvious changes in the optical appearance of this specimen. When viewed in the electron microscope limited porosity was evident in this specimen in spite of the fact that no volume change was detected with the density measurements. Much of this porosity is believed to arise because of the dropout of second phase particles during the specimen preparation and, hence, would not contribute to a density change. In Figure 3.18 this type of porosity appears as rows of shallow surface depressions which are aligned along a prior set of grain boundaries. This has been observed in nonirradiated specimens which were heated into the gamma. Apparently grain boundary segregation of the additives occurs in the gamma phase and precipitation of second phase particles takes place as the material is cooled to room temperature. This produces a network of precipitate particles outlining prior gamma grain boundaries. In some instances these second phase particles appear as holes due either to preferential etching or dropout of the particles. It becomes very difficult, therefore, to positively identify all of the holes that may appear on the metallographically prepared surface of an irradiated alloy specimen. A small amount of irradiation induced microcracking is believed to exist along some of the twin-matrix interfaces, Figure 3.18. These microcracks or tears present on many of the twin-matrix interfaces obviously contribute very little to an increase in volume. An occasional microtear located at a grain boundary triple point was also observed in this sample.



250X



1000X

FIGURE 3. 17

Metallographic Appearance of U + Fe-Al Specimen 26 A-1
Irradiated to 0.11 at. % Burnup at 535 C (995 F)

Neg. No. C-3112, C-3251

AEC-GE RICHLAND, WASH.



FIGURE 3.18

U + Fe-Al Specimen 26 A-1
Irradiated to 0.11 at. % Burnup at 535 C (995 F)
Shadowed, Negative Replica

Neg. No. 2262D

5500X

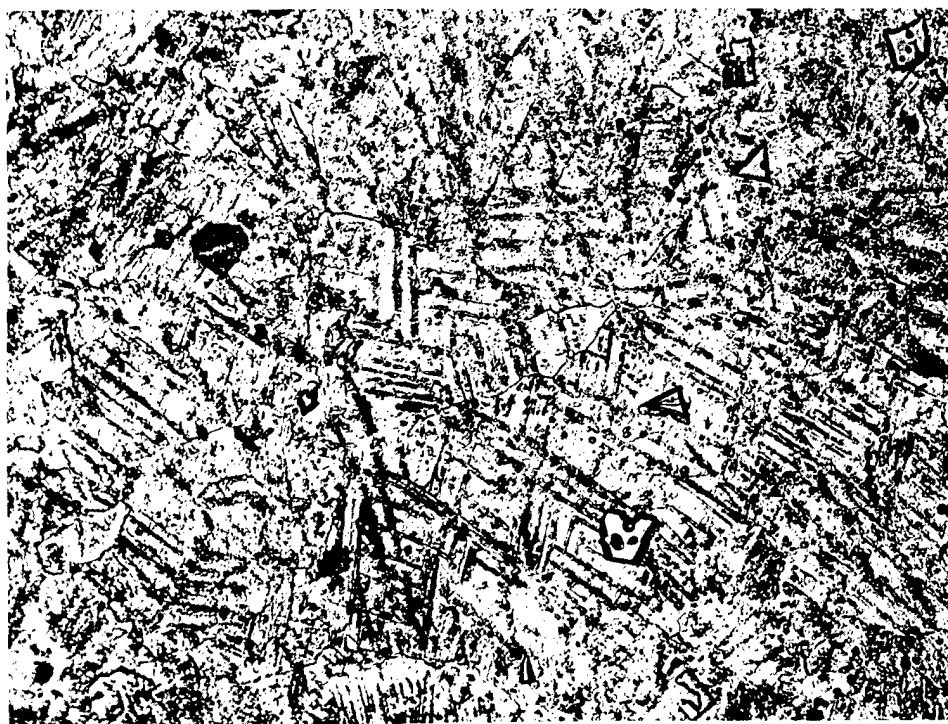
AEC-GE RICHLAND, WASH.

The second U + Fe-Al specimen (D-1) present in Capsule 26 received the standard beta treatment* prior to irradiation. This specimen exhibited a 3% increase in volume compared with the gamma-beta treated specimen which indicated a zero volume increase. The optical and electron metallography (Figures 3.19 and 3.20) confirm the density measurements. Microcracks and tears are present in greater numbers along many of the twin-matrix interfaces. This can be readily seen in the electron micrograph of Figure 3.20 and accounts for the increase in the black spots located along twin bands in the optical micrographs. The alignment of shallow holes along a prior set of boundaries was absent in this specimen as it had not been heated into the gamma.

Figures 3.21 and 3.22 show the structure developed by the U + Fe-Si specimen (A-2) that was gamma-beta treated prior to irradiation and Figures 3.23 and 3.24 show the structure developed by the U + Fe-Si specimen (D-2) that was beta treated prior to irradiation. The nature of the structural changes which take place in the U + Fe-Si alloy are similar to those that take place in the U + Fe-Al alloy. As expected, the magnitude of the tearing becomes progressively greater as the density decreases.

The preirradiation microstructure of the alloy specimens is indicated in Figure 3.25. The very large amount of second-phase present in the U + Fe-Al specimens is quite apparent. The segregation at prior boundaries can also be clearly seen in the U + Fe-Al specimens. Electron metallography is being conducted to establish the size distribution of second-phase particles.

* This particular capsule is designed for in-reactor operation at 140 kg/cm² (2000 psi). Therefore, to be consistent with standard practice it must be proof-tested at 210 kg/cm² (3000 psi). A pressurization system which is currently on order will have this capability. The above testing pressure is more than adequate for the first irradiation test which will be conducted at 70 kg/cm² (1000 psi).



250X

FIGURE 3.19

1000X

Metallographic Appearance of U + Fe-Al Specimen 26 D-1
Irradiated to 0.11 at. % Burnup at 535 C (995 F)

Neg. No. C-3138; C-3142

AEC-GE RICHLAND, WASH.



FIGURE 3.20

U + Fe-Al Specimen 26 D-1
Irradiated to 0.11 at. % Burnup at 535 C (995 F)
Shadowed Negative Replica
5000X

Neg. No. 2670A

AEC-GE RICHLAND, WASH.

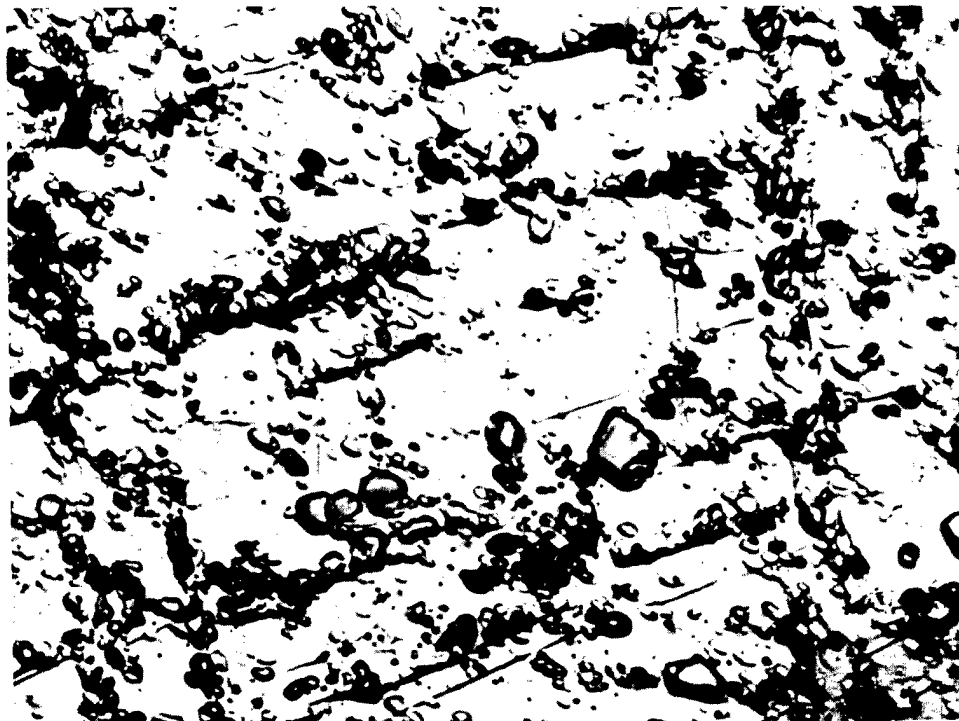
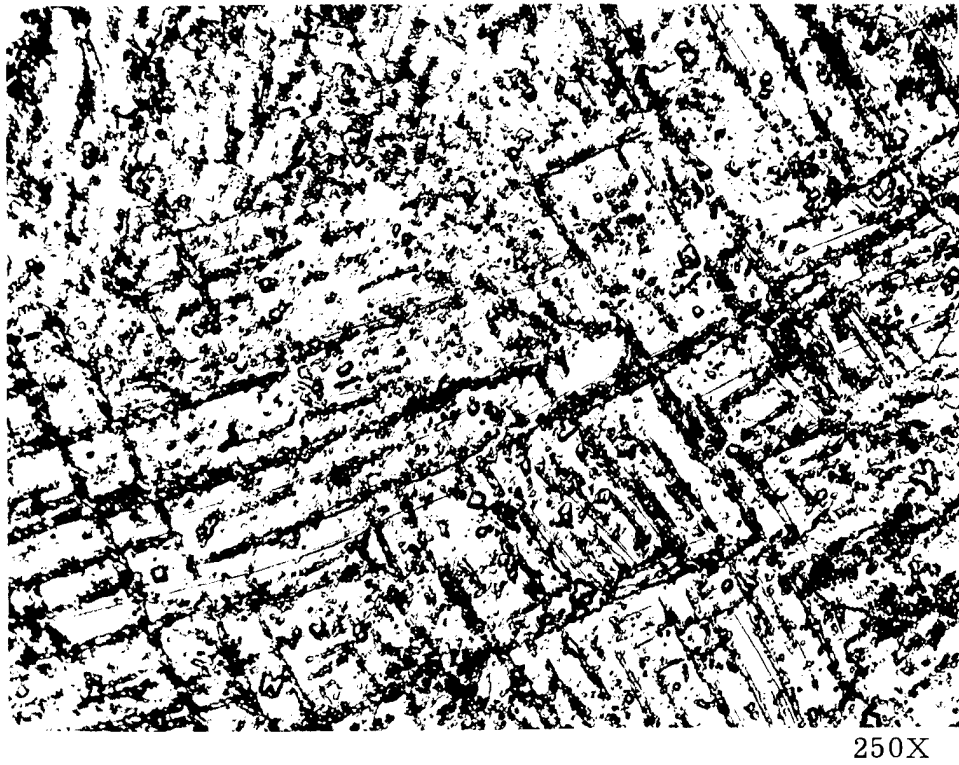


FIGURE 3. 21

1000X

Metallographic Appearance of U + Fe-Si Specimen 26 A-2
Irradiated to 0.11 at. % Burnup at 535 C (995 F)

Neg. No. C-3166; C-3172
AEC-GE RICHLAND, WASH.



FIGURE 3.22

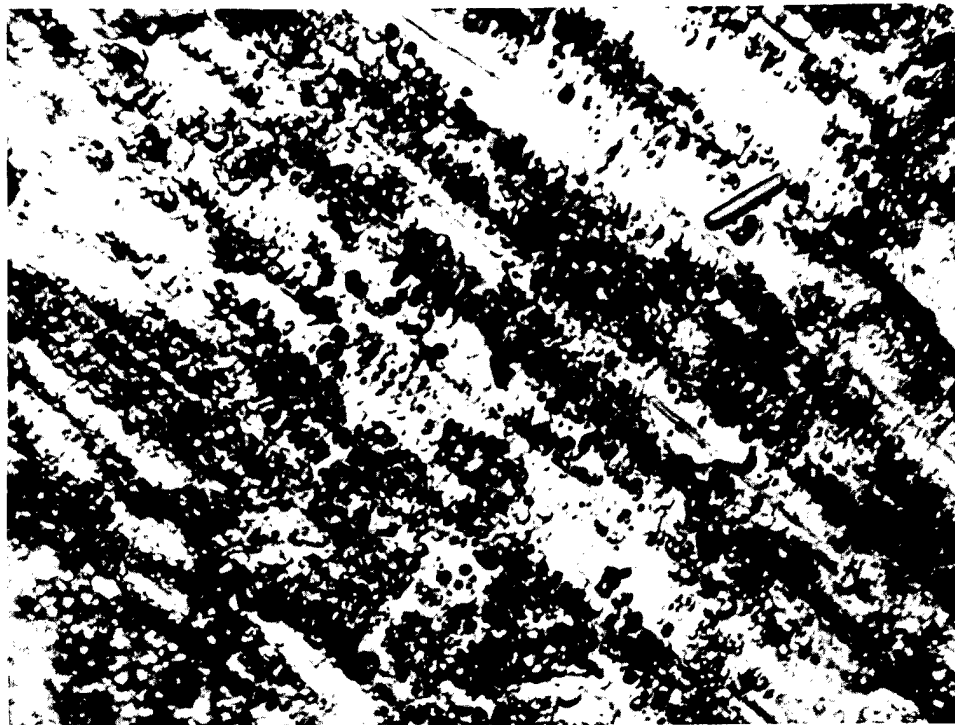
U + Fe-Al Specimen 26 A-2
Irradiated to 0.11 at. % Burnup at 535 C (995 F)
Shadowed Negative Replica
5800X

Neg. No. 2669D

AEC-GE RICHLAND, WASH.



250X



1000X

FIGURE 3.23

Metallographic Appearance of U + Fe-Si Specimen 26 D-2
Irradiated to 0.11 at. % Burnup at 535 C (995 F)

Neg. No. C-3156; C-3157

AEC-GE RICHLAND, WASH.

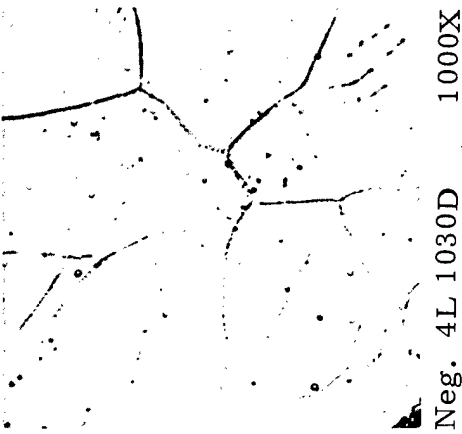


FIGURE 3.24

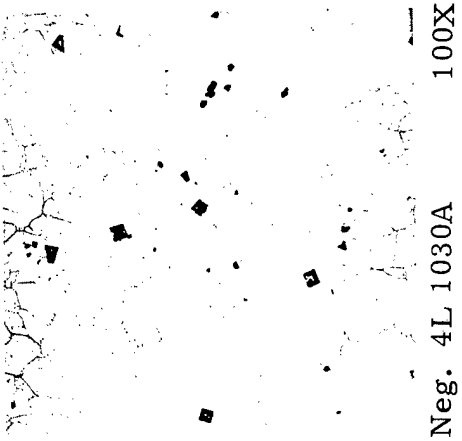
U + Fe-Si Specimen 26 D-2
Irradiated to 0.11 at. % Burnup at 535 C (995 F)
Shadowed Negative Replica
5500 X

Neg. No. 2677B

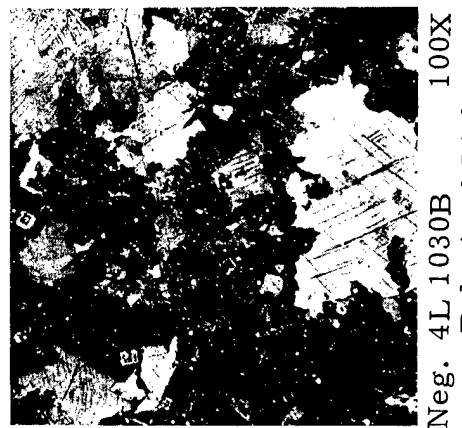
AEC-GE RICHLAND, WASH.



Neg. 4L 1030D 1000X



Neg. 4L 1030A 100X

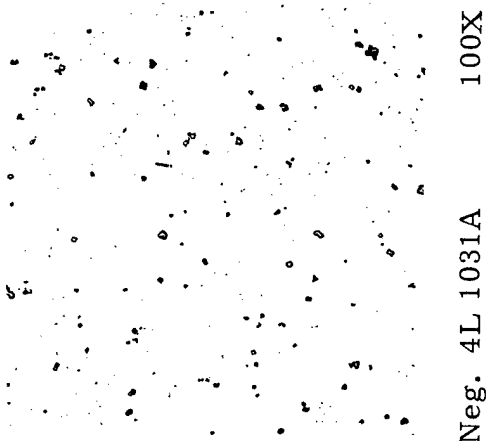


Neg. 4L 1030B 100X

Polarized Light



Neg. 4L 1031D 1000X



Neg. 4L 1031A 100X



Neg. 4L 1031B 100X

Polarized Light

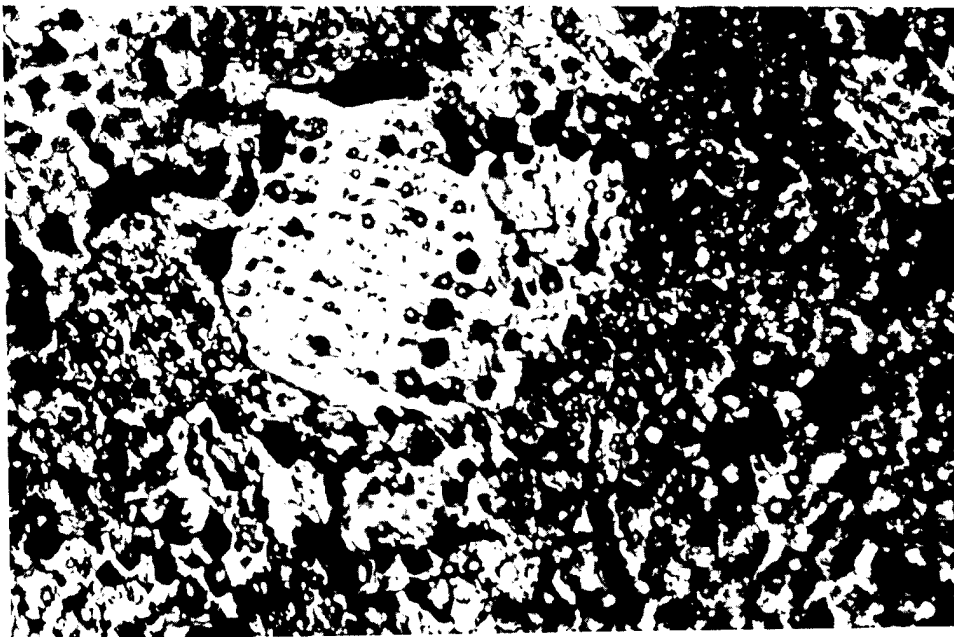
FIGURE 3.25

Preirradiation Metallographic Appearance of the U + Fe-Al (Top Row)
and U + Fe-Si (Bottom Row) Specimens Annealed 800 C (1472 F), 2 hr, Furnace Cooled;
730 C (1346 F), 15 min, Oil Quenched

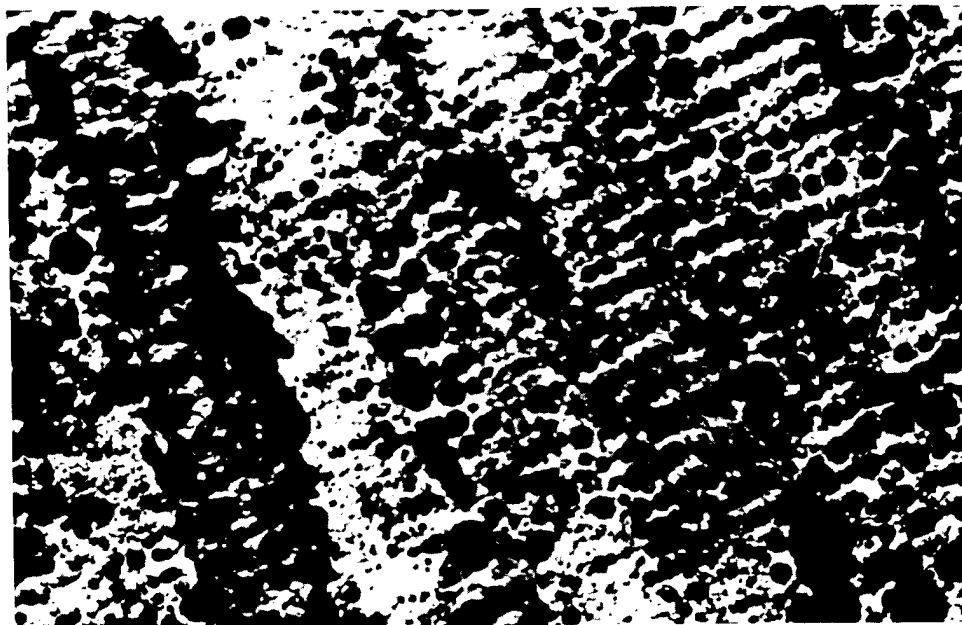
Four specimens of high-purity uranium (B-1, B-2, C-1 and C-2) representing four different metallurgical states were also included in Capsule 26. As can be seen in Table 3.2, the volume increase for three of the specimens was 20 to 25% while the fourth sample showed almost 40%. The as-extruded specimen had a fine grain size while the annealed specimens were extremely coarse grained. These differences in grain size are reflected in the degree of surface roughening after irradiation. Severe porosity was noted in all of the high-purity specimens. Much of it was aligned crystallographically within grains but an unusually large amount was also present at grain boundaries. Figures 3.26 and 3.27 illustrate typical structures obtained with these specimens. These four specimens represent the first irradiation data obtained from the second extrusion of high-purity uranium (T-3) employed on this program. The behavior agrees favorably with that of the first high-purity uranium extrusion (T-2) that has been studied extensively.

The specimens in Capsule 26 were irradiated in the temperature range where drastic volume increases are observed in high-purity uranium. The type of damage observed in this temperature range has been attributed to fission event induced defect recovery giving rise to crystallographically aligned microtears. The high-purity uranium specimens behaved about as expected showing the crystallographic alignment of microtears and the detrimental effect of large grains. For reasons not clear, the sample slowly cooled from the beta phase behaved more poorly than did any of the other high-purity specimens.

The alloy samples resisted this "recovery" type of volume change. The improvement depended radically on alloy content and to a lesser extent on the heat treatment. The role of twins in this type of volume increase was once again emphasized by the microstructures that were developed. When the amount of volume increase was small a very few microtears were detected at the twin-matrix interface. As the magnitude of the volume increase became greater more tears developed at the twin-matrix interface



(a) Specimen 26 B-1 (Table 3.2)

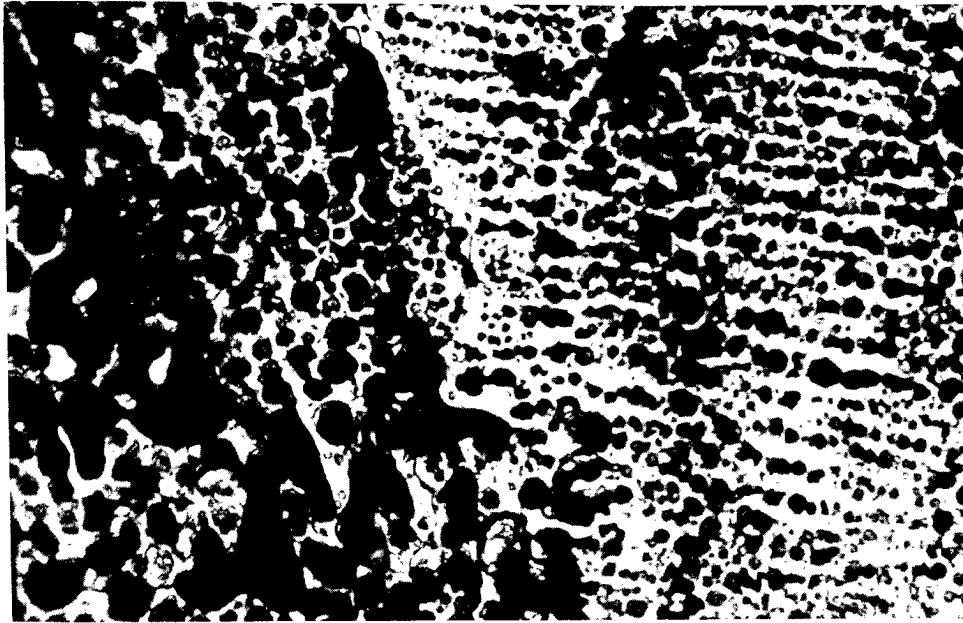


(b) Specimen 26 B-2 (Table 3.2)

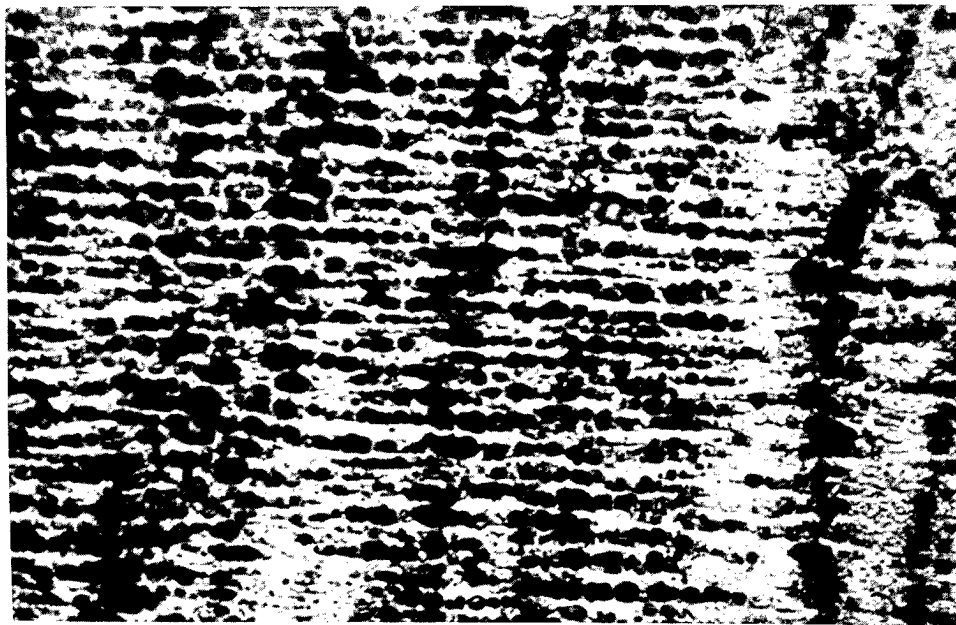
FIGURE 3.26

Metallographic Appearance of High-Purity Uranium (T-3)
Irradiated to 0.11 at. % Burnup at 585 C (1085 F)
1000X

Neg. No. C 3293; C 3313
AEC-GE RICHLAND, WASH.



(a) Specimen 26 C-1 (Table 3.2)



(b) Specimen 26 C-2 (Table 3.2)

FIGURE 3.27

Metallographic Appearance of High-Purity Uranium (T-3)
Irradiated to 0.11 at. % Burnup at 575 C (1067 F)
1000X

Neg. No. C 3418; C 3325
AEC-GE RICHLAND, WASH.

until in the case of Specimen 26 D-2 (13% swelling) the twin can no longer be detected and only the rows of tears can be seen. It is not clear whether the twins have completely annealed out. Much remains to be done to clarify the role of twins and their interaction with irradiation-induced defects in this "recovery" type of volume increase.

[Three general swelling capsules, No. 16, 20, and 21, containing high-purity uranium specimens of natural, 1.44% and 2.88% enrichment, respectively, were opened in radiometallurgy and the specimens were recovered. Immersion density measurements were made and both optical and electron metallography are in progress. The observed volume increases and the macro appearances were in agreement and essentially corroborated previous observations made with specimens of this type. The irradiation conditions, total exposure and amount of observed swelling are summarized in Table 3.3. The metallography will be described next quarter.

TABLE 3.3
IRRADIATION CONDITIONS AND VOLUME INCREASES OBSERVED
WITH SPECIMENS IN CAPSULES 16, 20, AND 21

copy

Specimen Number	Preirradiation Heat Treatment	Irradiation Temperature		Burnup at. %	As-Irradiated Density ρ , g/cc	Swelling, % $\frac{\rho_f - \rho_i}{\rho_f} \times 100$
		Reactor Up, C	Reactor Down, C			
16 A-1	A			0.07*	13.45	41
16 A-2	A	515	340		13.58	40
16 B-1	A				13.44	41
16 B-2	A	525	375		13.31	42
16 C-1	B				15.06	26
16 C-2	B	530	390		16.30	16
20 A-1**	A	-	-	0.16	12.40	53
20 A-2	A				15.78	20
20 B-1	A				15.46	23
20 B-2	A	625	425		16.58	14
20 C-1	B				13.97	36
20 C-2	B	570	410		16.12	18
21 A-1***	A			0.31	11.07	71
21 A-2	A	565	585		11.79	61
21 B-1	A				14.79	28
21 B-2	A	625****	625		10.21	86
21 C-1	B				12.49	52
21 C-2	B	605	630		11.80	61

A - As-extruded at 625 C (1157 F)

B - Vacuum annealed 730 C (1345 F), 15 min, oil quenched

* - These specimens were irradiated to 0.05 at. % burnup at the temperatures indicated and an additional 0.02 at. % burnup at about 450 C (842 F).

** - Capsule 20 specimens were enriched to 1.44 at. % U^{235} .

*** - Capsule 21 specimens were enriched to 2.88 at. % U^{235} .

**** - Due to the high fission heat several temperature excursions were experienced, several of which may have gone into the beta.

Second-Phase Distribution in Dilute Alloys of Uranium

Estimates have been made of the particle size distributions of precipitate particles in high-purity uranium containing small additions of iron and silicon. Calculations by the Schwartz-Scheil and Johnson-Saltykov⁽¹⁾ methods have provided useful comparisons with the Nicholson⁽²⁾ calculations used heretofore.

This particular phase of the dispersed particle study includes three materials: (A) high-purity dingot uranium, (B) composition A with small additions of iron and silicon, and (C) composition A with slightly larger additions of iron and silicon. The final composition of these materials is presented in Table 3.4. Heat treatments were designed to fulfill two particular

TABLE 3.4

SPECTROCHEMICAL ANALYSES DETERMINED AT HANFORD LABORATORIES

<u>Element</u>	<u>A (ppm)</u>		<u>B (ppm)</u>		<u>C (ppm)</u>	
	<u>Top</u>	<u>Bottom</u>	<u>Top</u>	<u>Bottom</u>	<u>Top</u>	<u>Bottom</u>
Iron	45	44	110	105	180	190
Silicon	18	21	50	54	95	92
Nickel	5	5	1	1	10	10
Carbon	13	24	9	9	19	15
Nitrogen	11	14	10	13	10	12
Hydrogen	2.5		2.4		2.8	

requirements: • bring the elemental components of the intermetallic second-phase into solution in the matrix and • precipitate the intermetallics as a finely dispersed second phase. Three temperatures were selected for solution treatments, in the alpha, beta, and gamma range, respectively, and two temperatures were selected for precipitation treatments in the low and medium alpha range. The first letter in the specimen identification code identifies the composition, with A being the pure material, etc. The second

1. F. N. Rhines and R. T. DeHoff. Quantitative Metallography, McGraw-Hill Book Company, New York, New York. (In Press)
2. W. L. Nicholson. Unpublished Data, General Electric Company, Richland, Washington.

letter identifies the solution treatment and the third letter, the precipitation treatment as indicated below.

Solution treatment = A - 7 hr 643 C (1187 F)

B - 5 hr 730 C (1346 F)

C - 2 hr 800 C (1472 F)

Precipitation treatment = A - 2 hr 538 C (1000 F)

B - 1 hr 590 C (1094 F)

The absence of a solution or precipitation treatment designator indicates the absence of that treatment, accordingly.

The results of the initial Nicholson calculations which were presented in the linear plot of Figure 3.3, HW-81269 were recalculated in that an error was found in the correction for the nonzero resolution point. Also, it was concluded that the high density of particles which appeared in these curves in the fine particle range adjacent to the resolution point was due to many particles being counted which were actually of a size below the resolution point. The revised estimates of the distributions for Specimens C, CA and CAB have been corrected in both of these respects. Also, estimates for Specimens AB and CBB have been added. Figure 3.28 presents a logarithmic plot of these distribution estimates. The ordinate on this plot is

$$y = \frac{\begin{array}{l} \text{(Calculated number of particles per cubic} \\ \text{centimeter which appeared with observed} \\ \text{radius, } r_{oi}, \text{ in the electron micrograph)} \end{array}}{\begin{array}{l} \text{(cell width in units of particle diameter)} \end{array}} = \frac{\text{particles/cc}}{\text{micron}}$$

A smooth curve was drawn through the points which were plotted at the cell midpoint of each cell. The curve was fitted to the data on a logarithmic plot because the nature of the distribution was most suited to this type of treatment. The curve may be accepted as an approximation to the curve with ordinates equal to

$$y_1 = \frac{\begin{array}{l} \text{(Calculated number of particles per cubic} \\ \text{centimeter of true radius } r_i) \end{array}}{\begin{array}{l} \text{(Cell width in units of particle diameter)} \end{array}}$$

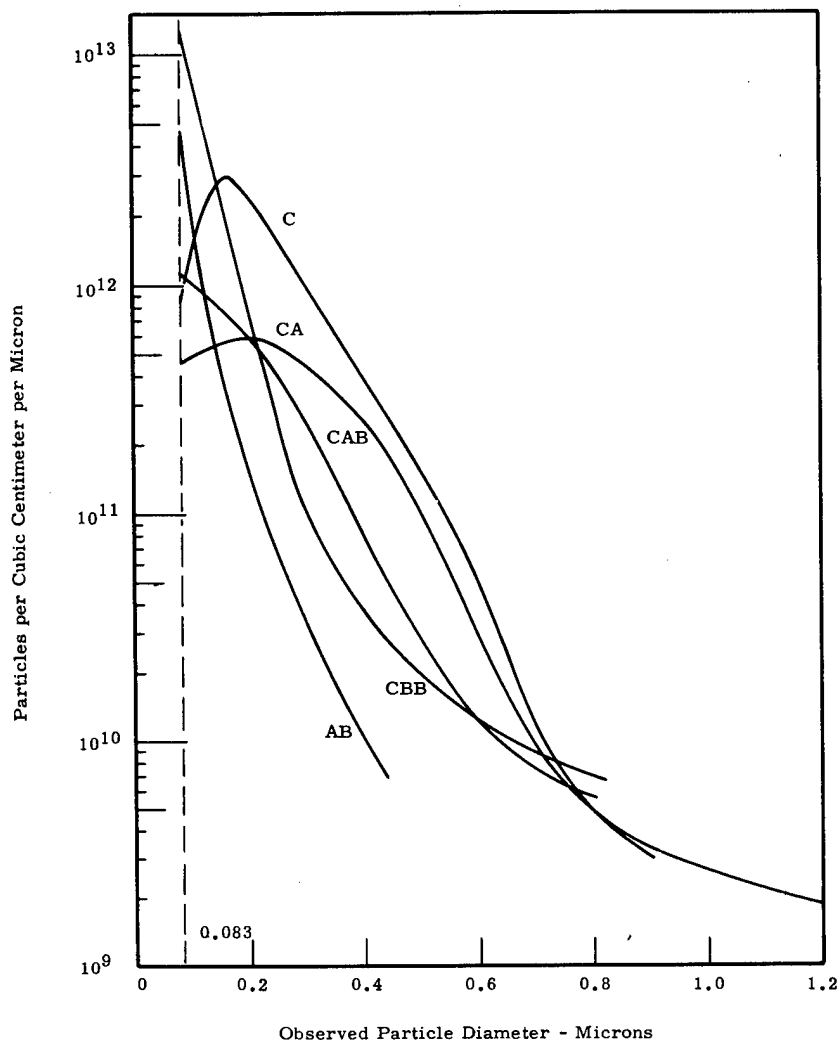


FIGURE 3.28

Particle Size Distributions of Precipitate Particles
in Dilute U + Fe-Si Alloys, as Calculated by the Nicholson Method

The particle size distribution curves are shown replotted in Figure 3.29 on a linear scale. These curves are the most meaningful, in that they may be integrated over any arbitrary range of particle size to yield directly the number of particles per cubic centimeter in that size range. Therefore, important information concerning the effect of heat treatment on the dispersed phase can be gained by observing the area beneath the respective curves. Specimen C, according to the Hanford

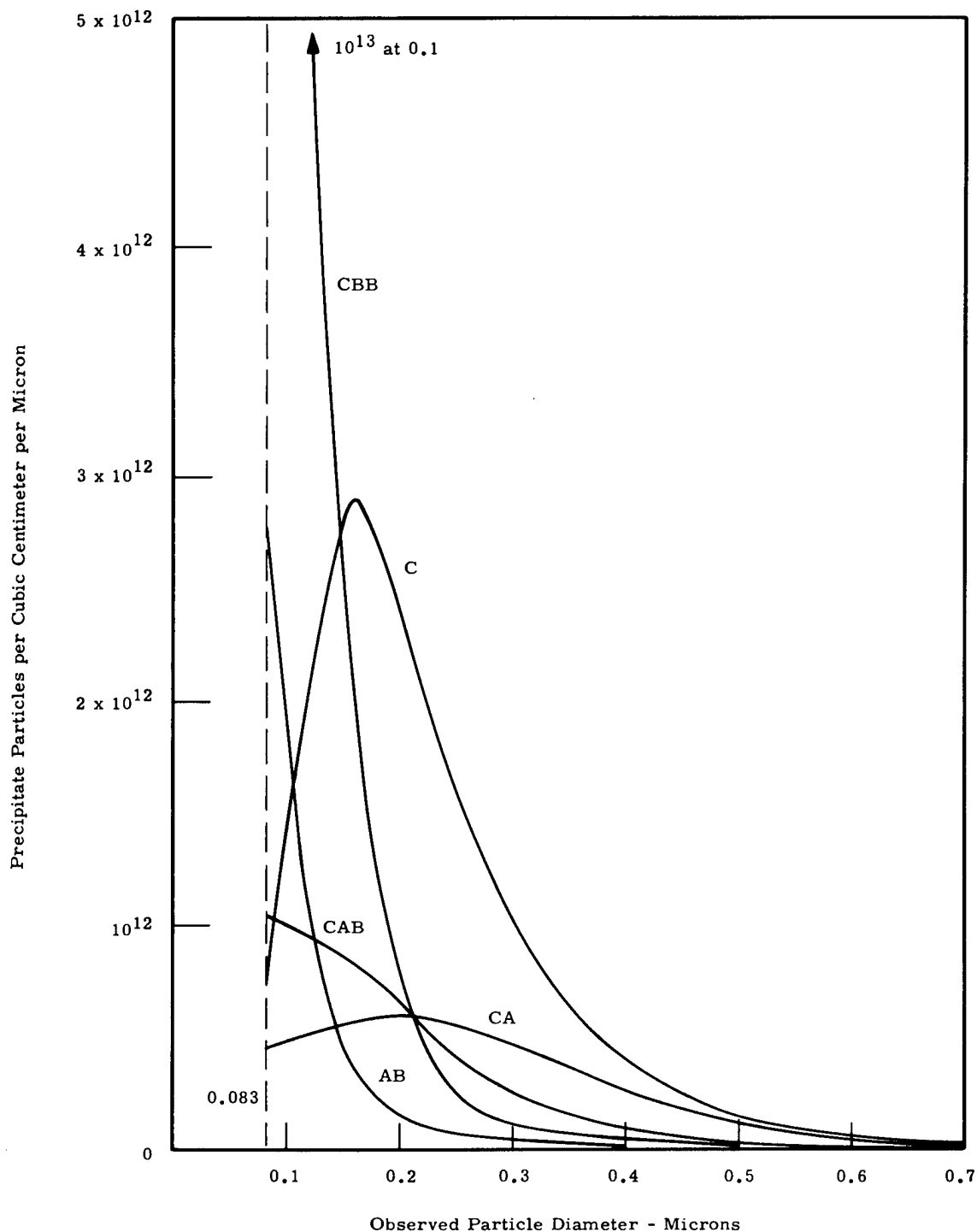


FIGURE 3.29

Linear Plot of Particle Size Distributions of Precipitate Particles in Dilute U + Fe-Si Alloys, as Calculated by the Nicholson Method

analysis, contained approximately 180 ppm iron and 90 ppm silicon. This specimen, which is in the alpha-rolled condition, exhibits a density peak at an observed particle diameter of 0.16μ and a total integrated particle density of 5.15×10^{11} particles/cc (Table 3.5). Curve CA represents the

TABLE 3.5
TOTAL PARTICLE DENSITY OBTAINED
FROM GRAPHICAL INTEGRATION OF DENSITY CURVES

<u>Specimen</u>	
C	$1030 (5 \times 10^8) = 5.15 \times 10^{11}$ particles/cc
CA	$376 (5 \times 10^8) = 1.88 \times 10^{11}$ particles/cc
CAB	$314 (5 \times 10^8) = 1.57 \times 10^{11}$ particles/cc
CBB	$829 (5 \times 10^8) = 4.15 \times 10^{11}$ particles/cc
AB	$221 (5 \times 10^8) = 1.11 \times 10^{11}$ particles/cc

result of solution treating the alpha-rolled specimen in the high alpha range. Apparently the majority of the fine particles were either taken into solution or agglomeration took place. While the peak remains at approximately the same particle size, it is significantly reduced in height. The total integrated particle density has been reduced to 1.88×10^{11} particles/cc. Precipitation treatment of the alpha-rolled and solution-treated material at 590 C (1094 F) results in the distribution of Curve CAB. The larger particles, above 0.2μ , have undergone further dissolution while some finer particles have precipitated. The total integrated particle density, however, has dropped to 1.57×10^{11} particles/cc, less than the solution-treated specimen. Apparently, the alpha range solution treatment is inadequate. The density curve of Specimen CBB, which was alpha-rolled and solution-treated in the beta range, followed by a precipitation treatment at 590 C (1094 F), emphasizes the benefits of a sufficiently high solution treatment. While the total integrated particle density is only 4.15×10^{11} particles/cc, slightly less than that of Specimen C, the majority of these are less than 0.2μ in diameter and the peak occurs below the resolution point, therefore, the actual total may be significantly higher. Specimen AB was included in this initial presentation strictly on the

basis of availability, but it makes an interesting comparison with the higher alloy specimens. This material contains only 45 ppm iron and 20 ppm silicon. This specimen, which was observed in the beta solution treated condition, has a total integrated particle density of 1.11×10^{11} , less than any of the higher alloy specimens. However, like the other beta solution treated specimen, it also has a density peak which is below the resolution point. This is an indication that the quenching rate is not fast enough to hold the intermetallic constituents in solution.

The calculated volume fraction of precipitate particles for the respective specimens is presented in Table 3.6. For an alloy content of 180 ppm iron

TABLE 3.6
TOTAL CALCULATED VOLUME FRACTION
OF PRECIPITATE PARTICLES

<u>Specimen</u>	<u>Volume Fraction</u>
C	0.0126
CA	0.0106
CAB	0.0038
CBB	0.0046
AB	0.0022

and 90 ppm silicon, the maximum possible volume fraction, i. e., no solubility, would be 0.008. However, some solid solubility would reduce this maximum and also, the presence of intermetallics and compounds formed by impurity materials would contribute to the measured quantity. Table 3.6 shows that volume fractions both above and below this level were encountered. Apparently, Specimens C and CA contained a significant quantity of these additive contributions. This was particularly true of CA which had an unreasonably high calculated volume fraction due to several particles greater than 1μ appearing in the counted data. With the exception of these noted discrepancies, the volume fraction calculations are in line with expectation.

Figure 3.30 presents a comparison of the results of three different methods of calculation of the particle size distribution curve for Specimen C, for which the particle count of 306 particles was greater than any of the other specimens counted. All give approximately the same shape of curve, with the Johnson-Saltykov method yielding slightly higher numbers than the Schwartz-Scheil. The Nicholson calculation, however lies significantly beneath the other two, a factor of approximately two less than the Johnson-Saltykov.

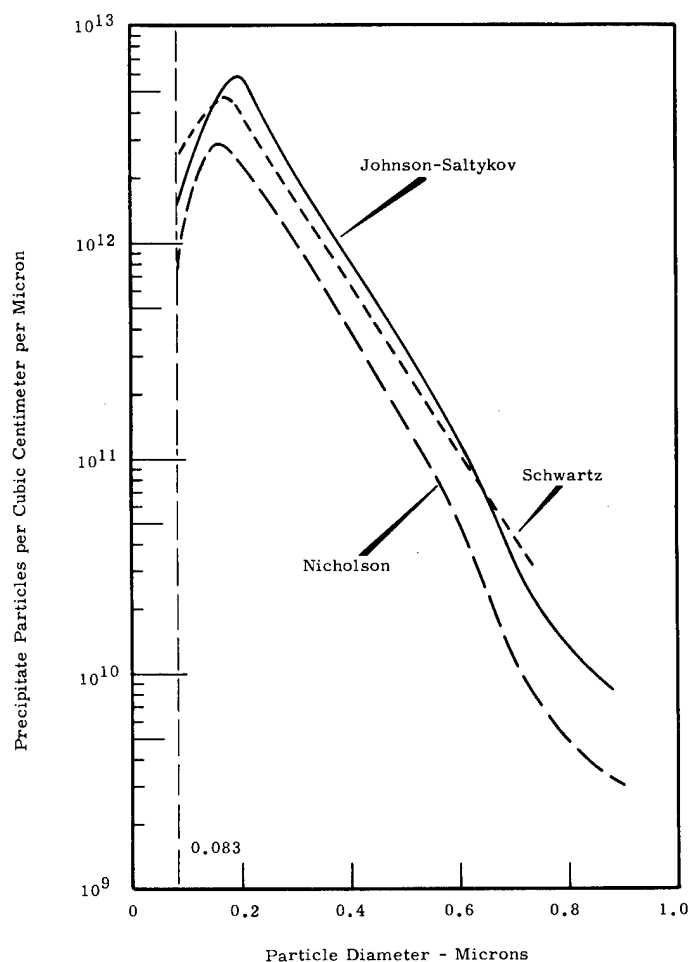


FIGURE 3.30

Comparison of Results Yielded by Different Methods
of Calculating Particle Size Distribution
of Precipitate Particles in Alpha-Rolled U-180 ppm Fe-90 ppm Si Alloy

The interrelationships between the various calculated distributions point out some questions which should be resolved in order to provide a firm foundation for further work. The Nicholson calculation estimates the density of particles in each cell which presents a particular observed radius in the electron micrograph. On the other hand, the Johnson-Saltykov and Schwartz-Scheil methods estimate the density of particles of a particular true diameter. Therefore, the Nicholson curve should be of somewhat different shape than the others. Particularly, it should yield a high-density of particles in the small particle region. In addition, the factor of two difference between the Nicholson and other methods in Figure 3.30 is also, at this point, unexplained. However, it should be noted that in a distribution which can readily be changed by one or more factors of 10 by an adjustment in heat treating schedule, a factor of two is not necessarily significant.

The calculated distributions of Specimens CAB, CBB, and AB, in Figure 3.29 indicate the necessity of lowering the nonzero resolution point in order to bring the peaks of the distributions of these alloys into the range of investigation. Making measurements on the finer particles requires micrographs of higher magnifications, i. e., 30,000X or 60,000X. In order to make this possible it will be necessary to further develop the surface preparation technique either by further development of the electrolytic process or by vacuum cathodic etching. Such further developments in surface preparation and accompanying reduction of the resolution point should make it possible to select the optimum combination of heat treatments to gain a high density of fine particles in the U-Fe-Si system, and also allow the technique to be extended to other systems.

PLUTONIUM PHYSICAL METALLURGY - R. D. Nelson, F. E. Bowman,
H. E. Kissinger, and B. Mastel

The objective of this program is to conduct basic studies on the properties of high-purity unalloyed and alloyed plutonium. Studies will include investigation of phase transformation, phase stabilization, deformation, fracture, texturing, internal stresses, microcracking, grain growth, recovery and recrystallization, and measurement of mechanical and physical properties. The unique structure of several of the plutonium allotropes and their narrow temperature span of stability leads to characteristics and anomalies which, if explained, will contribute to the general area of solid state science.

Steady-State Creep of Plutonium

The investigation of the steady-state creep characteristics of the six allotropes of plutonium has been completed with the exception of certain anomalies. The creep tests were performed under isothermal conditions as well as under variable temperature conditions. Representative results of the steady-state creep behavior of each allotrope are given in Figure 3.31.

Sherby⁽¹⁾ has derived an empirical expression for steady-state creep of metals. This expression is $\dot{\epsilon} = SL^2D \left(\frac{6}{E} \right)^5$, where S is a universal constant having a value of 10^{29} cm^{-4} for high temperature creep (i. e., the test temperature, T is greater than one-half the absolute melting temperature, T_m), L is the grain diameter in cm, and $D = D_0 \exp \frac{(K_0 + V)}{T_m}$. In the expression for D, D_0 is a universal constant equal to $1 \text{ cm}^2/\text{sec}$, V is the valence, and K_0 is a constant that depends solely on crystal structure. The term $(K_0 + V)/T_m$ might be considered equal to Q/R , where R is the gas constant. The effective melting temperature, T_m , of each allotrope has been calculated according to the method derived by Ardel.⁽²⁾ Values of activation energy and effective melting temperatures of each phase are given in Table 3.7.

1. O. D. Sherby. "Factors Affecting the High Temperature Strength of Polycrystalline Solids," Acta Met., vol. 10, p. 135. 1962.
2. A. J. Ardel. "On the Calculation of Melting Temperatures of Low Temperature Phases of Polymorphic Metals," Acta Met., vol. 11, p. 591. 1963.

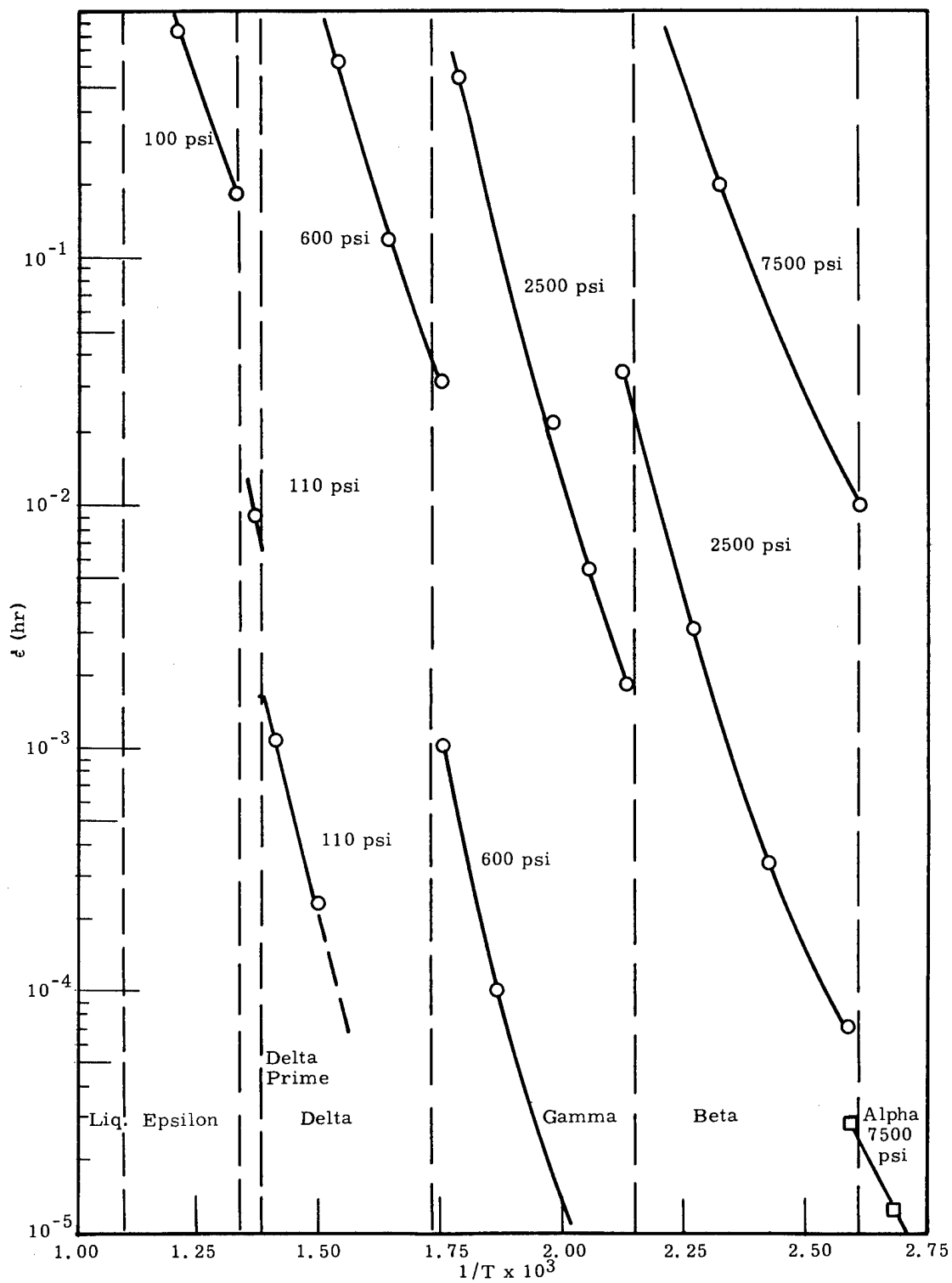


FIGURE 3.31

Temperature Dependency of Plutonium Creep

TABLE 3.7

EFFECTIVE MELTING TEMPERATURE AND ACTIVATION ENERGIES
FOR CREEP OF EACH OF THE ALLOTROPES OF PLUTONIUM

Phase	Effective Melting Temperatures		Steady-State Creep Activation Energy K/cal/g-atom
	C	F	
Alpha	290	554	20
Beta	475	887	28
Gamma	530	986	34
Delta	570	1058	30
Delta Prime	570	1058	29
Epsilon	640	1184	25

The most notable of the anomalies is the significantly higher creep rate of the beta phase after $\alpha \rightarrow \delta$ transformation than after $\alpha \rightarrow \beta \rightarrow \gamma \rightarrow \delta$ transformations. The steady-state creep rate of the beta phase formed directly from alpha is $1 \times 10^{-2} \text{ hr}^{-1}$ at 185 C (365 F) and 2700 psi. At the same temperature and stress the creep rate of the beta formed directly from gamma is $6 \times 10^{-5} \text{ hr}^{-1}$. The times and temperatures at which the samples were held in each phase are given in Figure 3.32. The steady-state creep rate of gamma at the same conditions is also given.

The creep rate of the gamma phase formed from the beta phase is the same as the gamma formed from delta. For example at 300 C (572 F) and 1500 psi, the steady-state creep rates of the gamma phase formed from the beta phase and the delta phase were, respectively, 1.9×10^{-2} and $1.7 \times 10^{-2} \text{ hr}^{-1}$, Figure 3.33. The steady-state creep rate of the delta phase at the same conditions is also given.

The anomalous behavior of the beta phase has been examined as a function of several transformation rates, temperatures, and pressures; the anomaly still persists. The densities of the beta phase at 140 C (284 F) after each transformation were the same within $\pm 0.01 \text{ g/cm}^3$.

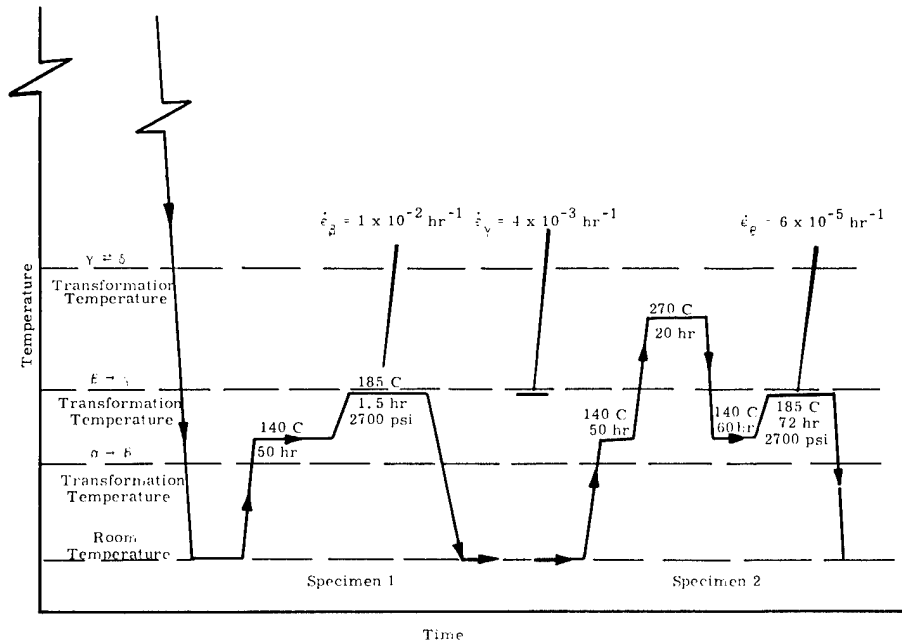


FIGURE 3.32

Schematic Diagram Showing the Steady-State Creep Rate of Beta at 2700 psi after $\alpha \rightarrow \beta$ and $\alpha \rightarrow \beta \rightarrow \gamma \rightarrow \beta$ Transformation

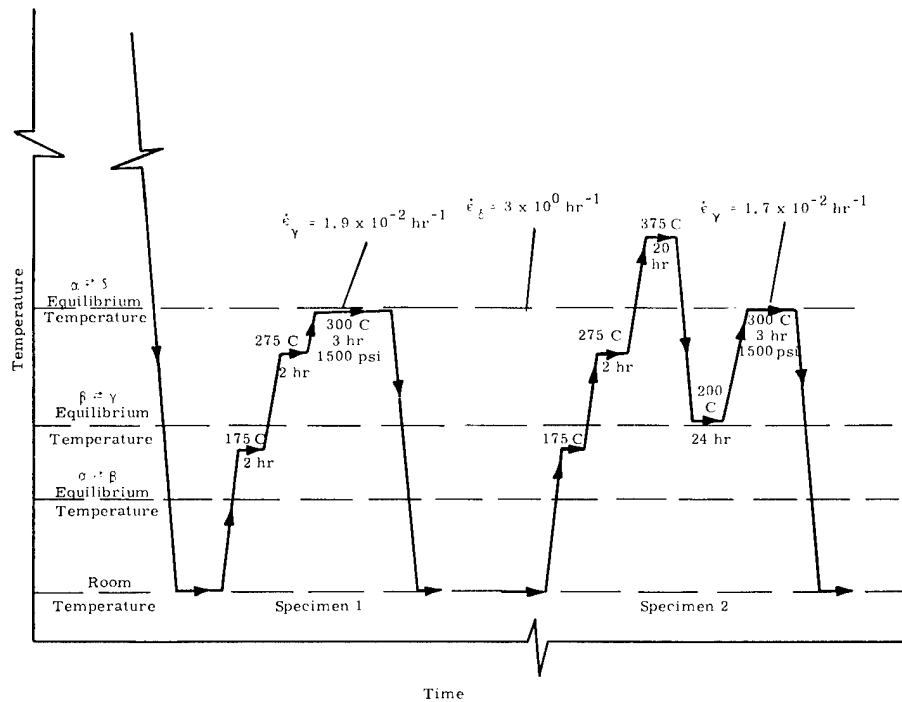


FIGURE 3.33

Schematic Diagram Showing the Steady-State Creep Rate of Gamma at 1500 psi after $\beta \rightarrow \gamma$ and $\delta \rightarrow \gamma$ Transformations

Plutonium Research Glovebox

The physical metallurgy research glovebox has been installed and placed in operation, Figure 3. 34. The functions in the glovebox are vacuum induction melting and casting, vacuum cathodic etching, electrical resistivity measurements, elevated temperature metallography, and replicating of etched and fractured surfaces for electron microscopy.

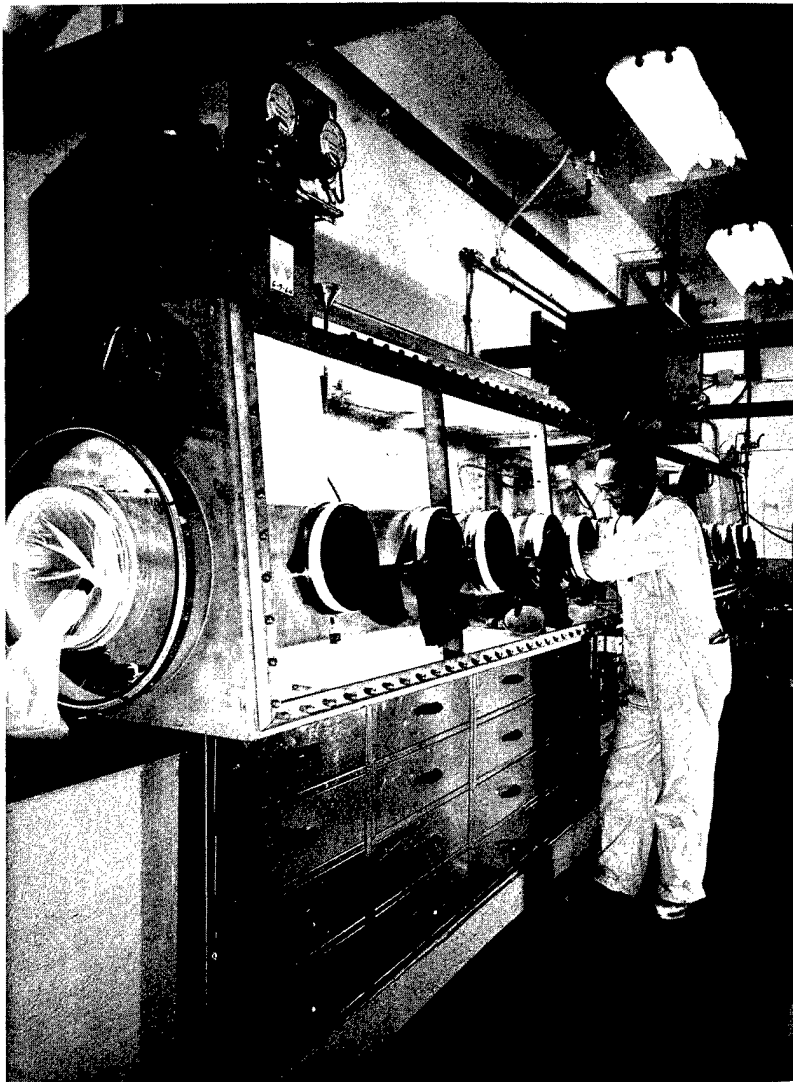


FIGURE 3. 34

Plutonium Physical Metallurgy Research Glovebox

Metallography

Metallographic etching techniques have been extended to include vacuum cathodic etching, Figure 3.35, and alternating current electrolytic etching using a nitric acid-methyl alcohol solution. Both techniques develop a microstructure that can be observed by bright field illumination. Representative microstructures obtained by these etching techniques and by electrolytic etching for polarized light illumination are shown in Figures 3.36 to 3.38. The microstructures are of the same electrorefined metal. The use of a nitric acid-ethyl alcohol-water electrolyte for developing a microstructure for bright field examination has been abandoned.



FIGURE 3.35

Cathodic Vacuum Etching Apparatus

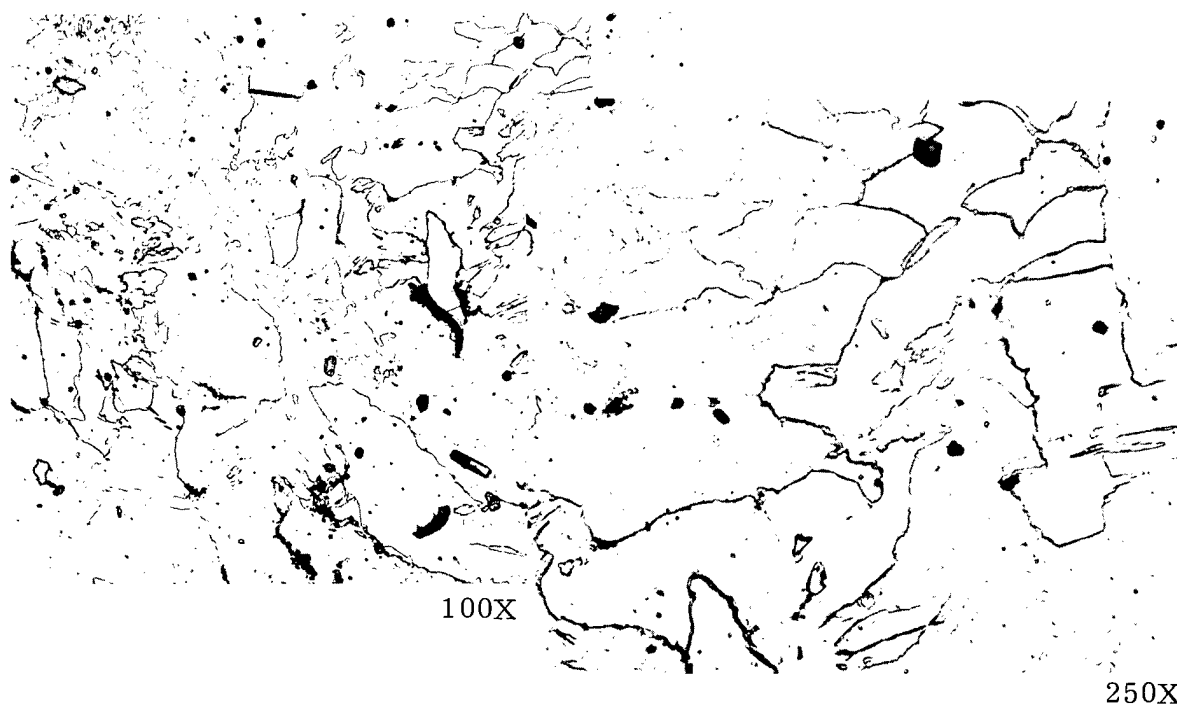


FIGURE 3.36

Microstructure of Electrorefined Plutonium, Cathodic Vacuum Etched
45 min at 3 mamp and 3500 v at a Pressure of 1.5×10^{-2} Torr

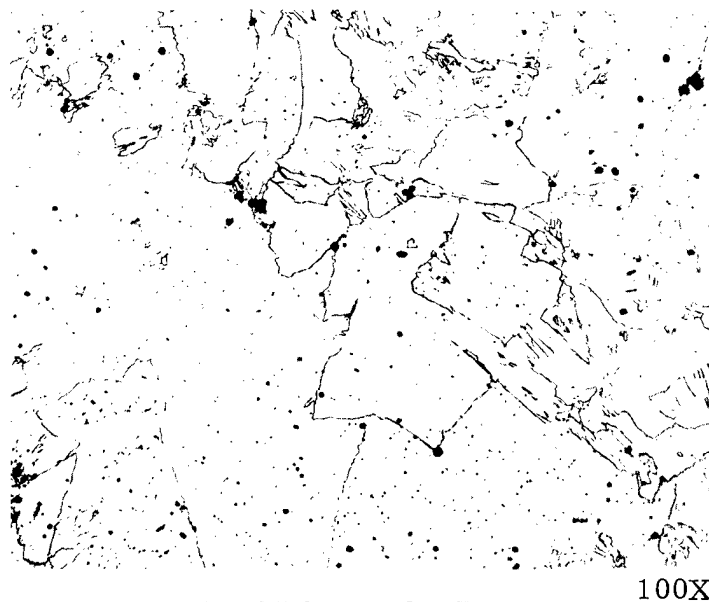
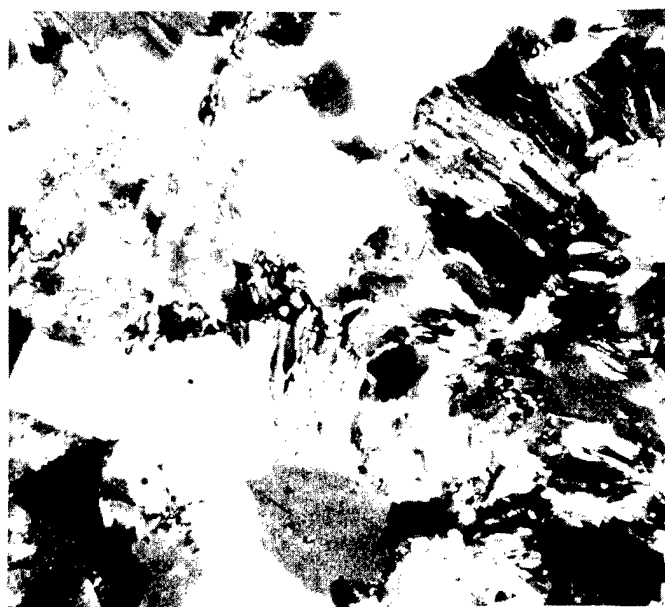


FIGURE 3.37

Electrolytically Etched 60 sec at 12 v ac with a Current Density
of 6 amp/cm^2 in. An Electrolytic Etchant Consisting
of 90% Methyl Alcohol and 10% Nitric Acid
(Same metal as Figure 3.36)

Neg. No. R4713; R4714; R4244

AEC-GE RICHLAND, WASH.



100X

FIGURE 3.38

Electropolished 60 sec at 65 v in an Electrolytic Etchant Consisting of 23% Tetraphosphoric Acid, 17% Water and 60% 2-Ethoxyethanol (Same metal as Figures 3.36 and 3.37)

The microstructures obtained by the three techniques are quite similar. The grain boundaries are somewhat distinct and well defined by bright field illumination. The grain size under bright field illumination is comparable to that observed under polarized light illumination.

The vacuum cathodic etched microstructure was obtained by maintaining a current of 3 mamp for 45 min at 3500 v dc in a Krypton gas at a pressure of 1.5×10^{-2} ton. No grain boundaries were observed after 1 hr and 45 min at 0.5 mamp.

The $\alpha \rightarrow \beta$ transformation during etching was avoided by keeping the sample below the transformation temperature with liquid nitrogen. Small alpha grains would have been observed if the $\alpha \rightarrow \beta \rightarrow \alpha$ transformations had occurred. When etching was performed without the liquid nitrogen coolant, bands of small alpha grains were observed that had formed during the $\alpha \rightarrow \beta \rightarrow \alpha$ transformations.

Vacuum cathodic etching in this manner appears to be very good for developing the microstructure of plutonium for optical and electron microscopy. However, this technique requires further development.

Transformation Kinetics

The $\beta \rightarrow \alpha$ transformation kinetics of electrorefined and vacuum-cast wafers were investigated at -196°C (-321°F). The thickness of the wafers was 0.005 in. and the diameter was 1 in. The incubation time was less than 1 sec and the time at which the transformation was essentially complete was 5 sec. These data are significantly different from the early work that showed the $\beta \rightarrow \alpha$ transformation to be somewhat sluggish at -196°C (-321°F).

Physical damage in the form of internal voids was essentially absent after nine $\alpha \rightleftharpoons \beta$ transformation cycles. For example, the density at room temperature before cycling was 19.58, whereas after cycling the density was 19.57, indicating no appreciable damage. No investigation was made to determine the extent of phase retention.

Deformation and Fracture Mechanisms

A single crystal orienter adapted for use as a pole figure goniometer has been installed on the glovebox enclosed X-ray diffractometer. It was apparent from the high absorption coefficient of plutonium for X-rays with wave lengths in the 1.5 \AA range that only reflection techniques could be employed in pole figure work. The characteristics of the alpha plutonium diffraction pattern are such as to render the shorter, more penetrating wave lengths unsuitable because of the resulting variations of the major lines. It was, therefore, essential that the angular dependence of the absorption correction to be applied to the diffracted line intensity be established. This requires a randomly oriented fine-grained material. It was rather surprising to find that such a material was not readily obtained. The normal as-cast material gave evidence of distinct "graininess" despite the fact that metallographically the grain size appeared to be in the micron range. After several heat treatments it was found that only by quenching from the gamma phase could a sample be obtained which yielded a relatively constant line intensity when rotated in its own plane.

The use of such a quenched sample revealed that plutonium specimens could be rotated only 30° from the vertical at which position the absorption corrections become excessive. In order then to completely determine the pole figure it will be necessary to employ four specimen wafers; the rolling plane surface, the transverse section surface and surfaces at 30° to each of these. It is believed that such a system will permit the data for a complete pole figure to be obtained with a minimum amount of specimen machining.

Material for this work has been successfully rolled from castings made from the electrorefined Los Alamos Scientific Laboratory material. These castings were made in the newly installed vacuum induction furnace using magnesium oxide crucible molds. The metal is charged in the mold hot-top and the entire system heated by means of a tantalum susceptor. As the charged metal fuses it runs into the mold cavity. By this means the potential contamination resulting from a crucible melt with subsequent pouring is eliminated. As a result of the use of the present method, a casting $1 \times 4 \times 0.180$ in., having a density of 19.57 g/cm^3 , was obtained. This is a bit thicker than was desired. The thickness resulted from the fact that one of the first slip-cast molds made to the present design was employed and complete dimensional control had not been established.

In actual rolling, however, this additional thickness did not appear to exert the influence on rolling characteristics which had been noticed in earlier rolling investigations. Previously it had been impossible to reduce castings greater than 0.125 in. in thickness by more than about 10%. With the present material, a total reduction of 90% was accomplished without excessive edge cracking. Rolling was done in the two high enclosed Stannot mill with 6×8 in. rolls operating at 16 surface ft/min. The rolls and table were heated to 80°C (176°F). Reductions of essentially 10% per pass were accomplished, with 24 passes being required to effect the reduction from 0.180 to 0.017 in.

As mentioned earlier, it had not been found possible to roll the more conventional production material in castings greater than about 0.125 in. in thickness. The present success with 0.180 in. thick castings can at present only be attributed to the higher purity of the material. Further work will have to be done, however, before a definite statement in this regard is warranted. Attempts will be made at a later date to determine the thickness limits, if any, which exist for casting thickness in the case of the high-purity material.

It has been suggested previously that the rolling characteristics were significantly affected by self-damage mechanisms. This was based upon observations that material which had aged some 90 days after casting could no longer be rolled. Further evidence supporting this conclusion has been obtained. A slab casting about 0.110 in. thick which had been stored 4 months could not be reduced 10% prior to catastrophic cracking and fracture. This was despite the fact that similar castings made from the same heat had been successfully reduced 90% shortly after casting. Further data in this regard is to be obtained with the high-purity material. One-half of the casting, which has just recently been rolled, has been set aside to age. Its rolling characteristics under conditions which have been found successful in the present experiment will be employed on this piece after several months aging.

An investigation of the fiber texture existing in the columnar grained alpha plutonium produced by transformation from beta under pressure has been initiated. Insufficient data exists at present to prepare a pole figure, although it has been possible to tentatively identify the plane which appears most active in this specialized type of transformation. Figures 3.39 and 3.40 indicate the major characteristics of the diffraction patterns obtained from surface parallel and perpendicular to the direction of applied stress. It appears that the intensity of the $(20\bar{3})$ plane reflection is most sensitive to direction relative to that of stress application. It lies parallel to the stress direction, according to the evidence at hand. However, it is evident

that to obtain the details of the texture established, either by rolling or by transforming under pressure, it will be necessary to make an exhaustive study of several lines in the diffraction pattern. It is hoped that a detailed knowledge of this transformation texture will yield a valuable light on the transformation mechanism as well as upon the crystallographic relationship between beta and alpha plutonium.

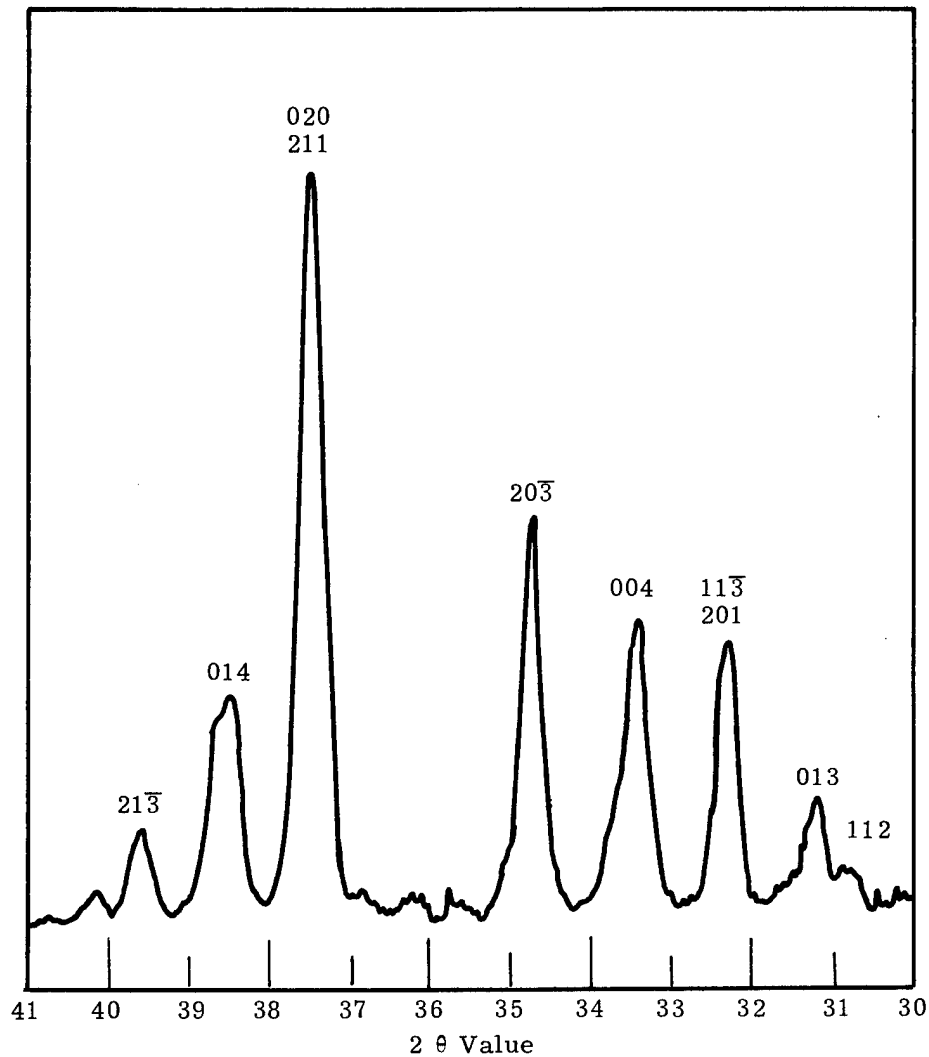


FIGURE 3.39

Alpha Plutonium Transformed Under Load Diffraction Pattern
from Surface Parallel to Direction of Applied Stress

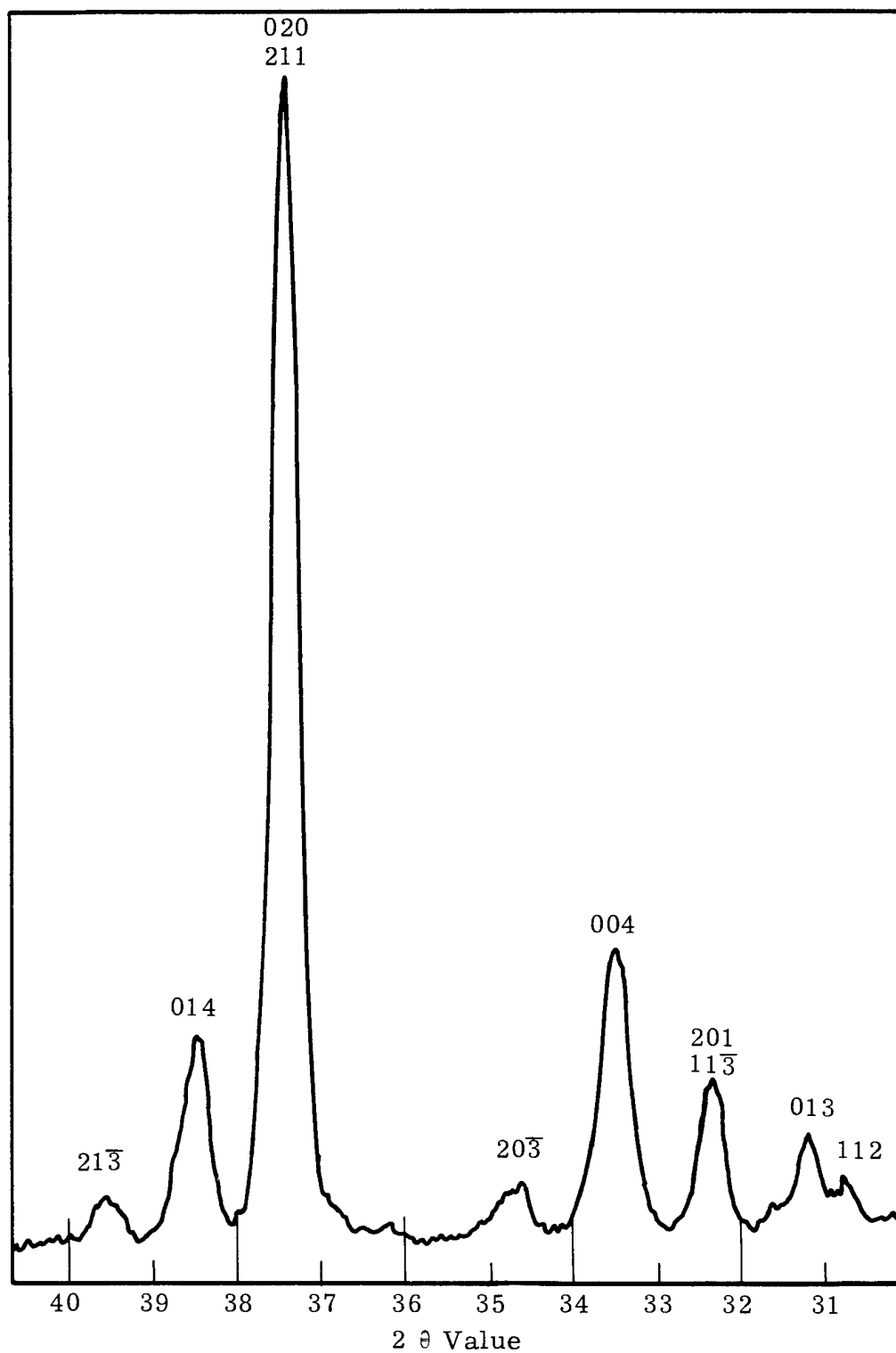


FIGURE 3.40

Alpha Plutonium Transformed Under Load Diffraction Pattern
from Surface Perpendicular to Direction of Applied Stress

REACTOR METALS RESEARCH

ALLOY SELECTION - T. T. Claudson

As a part of the alloy selection portion of the Irradiation Effects on Reactor Metals Program, corrosion and oxidation tests are being performed on nickel-base alloys suitable for various reactor applications. Two series of tests have been completed by the Chemical Metallurgy personnel at Hanford Laboratories. As reported in the previous quarterly report, specimens were tested in two environments: 15 mm Hg water vapor in helium at 1500 F (815 C), 1700 F (921 C), and 1900 F (1030 C), and in 1200 F (650 C) deoxygenated steam containing less than 50 ppb oxygen flowing at 2 liters/hr. The specimens were exposed to water vapor for 100, 200, and 300 hr and in steam for 336, 772, 1000, and 1680 hr. Figures 4.1 and 4.2 show the data collected for specimens exposed to 1200 F (650 C) steam. All alloys except Hastelloy R-235, Inconel 702, and Hastelloy N showed weight gains. These three alloys exhibited substantial losses in weight varying between 10 and 40 mg/cm² after 1680 hr.

Of the remaining alloys showing weight gains Hastelloy X-280, Inconel 600, Incoloy 800, and Inconel 718 were superior in corrosion resistance. Weight gains of less than 0.35 mg/cm² were found after 1680 hr as shown in Figure 4.1. Haynes 25, Hastelloy C, and Inconel 625 all showed weight gains between 20 and 40 mg/cm² after an equal period of time as seen in Figure 4.2. Metallographic examinations are presently underway to determine the extent of oxide penetration.

Figures 4.3, 4.4, and 4.5 summarize the data for nickel-base alloys exposed to 15 mm Hg water vapor in helium at 1500 F (815 C), 1700 F (921 C), and 1900 F (1030 C), respectively. Hastelloy N exhibited the best overall performance in these environments. Generally, a tight adherent oxide film was produced with a slight amount of intergranular penetration only at 1900 F (1030 C). Hastelloy X-280 and Hastelloy C followed Hastelloy N in oxidation resistance exhibiting the same type of oxidation behavior.

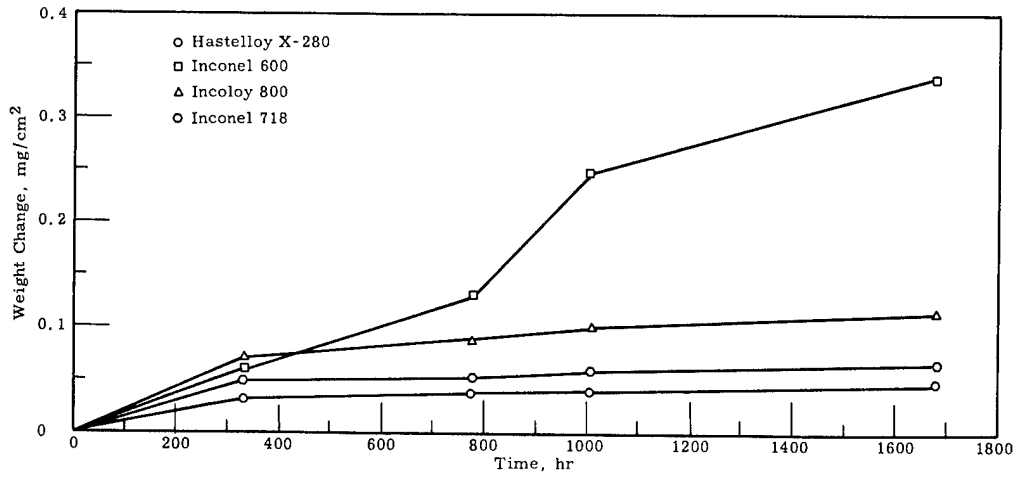


FIGURE 4.1

Corrosion of Super Alloys in 650 C Deoxygenated Steam
Containing < 50 ppb Oxygen Flowing at 2 liters/hr

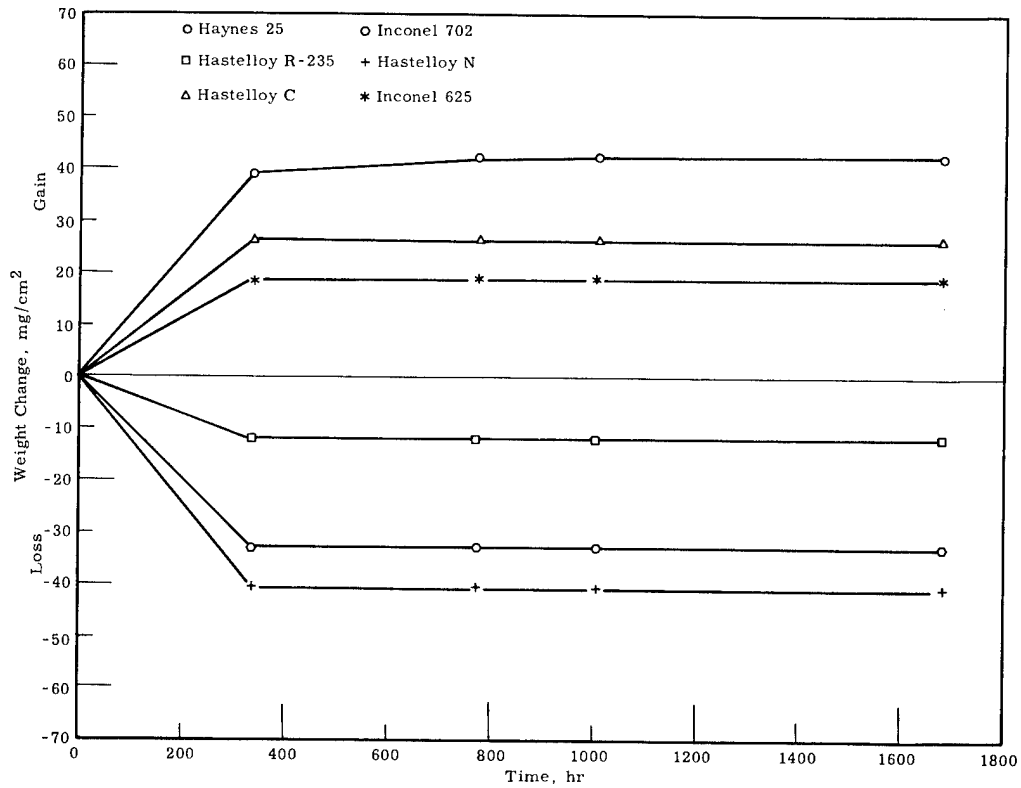


FIGURE 4.2

Corrosion of Super Alloys in 650 C Deoxygenated Steam
Containing < 50 ppb Oxygen Flowing at 2 liters/hr

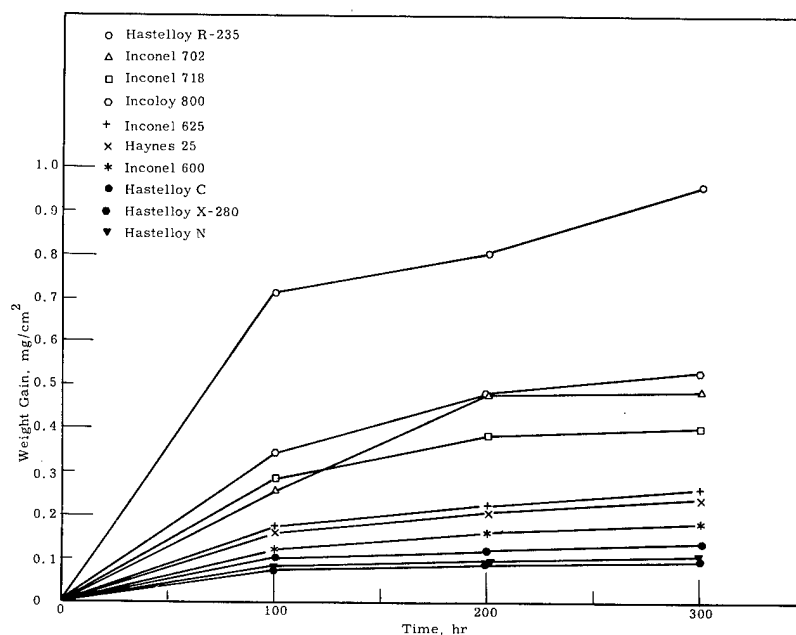


FIGURE 4.3

Oxidation of High Temperature Alloys
Exposed to 15 torr H₂O in Helium at 1500 F
Flow Rate = 1 ft³/hr

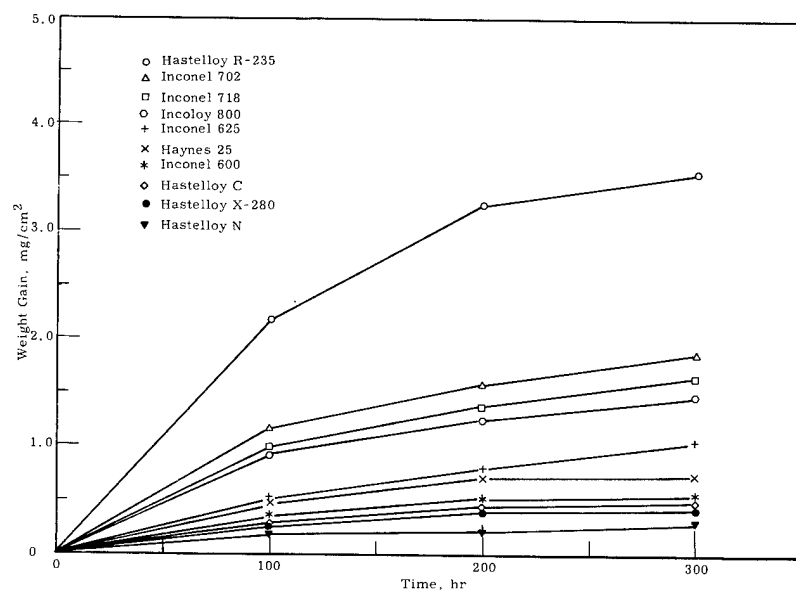


FIGURE 4.4

Oxidation of High Temperature Alloys
Exposed to 15 torr H₂O in Helium at 1700 F
Flow Rate = 1 ft³/hr

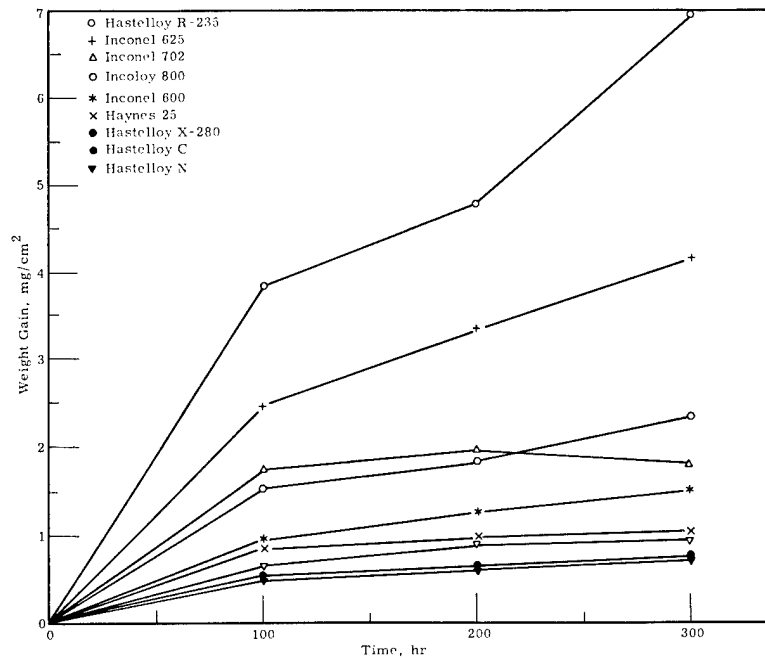


FIGURE 4.5

Oxidation of High Temperature Alloys
Exposed to 15 torr H₂O in Helium at 1900 F
Flow Rate = 1 ft³/hr

Inconel 718 exhibited weight gains for the 1500 F (815 C) and 1700 F (921 C) test but lost a substantial amount of weight for the 1900 F (1030 C) test. Photomicrographs show a thin layer of surface oxide with small amounts of intergranular penetration at 1500 F (815 C). These conditions increase in severity at 1700 F (921 C) and finally show signs of the surface oxide breaking at 1900 F (1030 C). The weight loss after 300 hr at 1900 F (1030 C) was 13.8 mg/cm².

Materials which showed signs of severe intergranular penetration at each level of temperature were Incoloy 800, Inconel 702, and Hastelloy R-235. Total oxide penetration observed was 4.5, 1.5, and 3.5 mils, respectively.

The Haynes 25, Inconel 600, and Inconel 625 all exhibited good oxidation resistance at all temperature levels. Tight adherent oxide coating formed which increased in thickness with increasing temperature. While Inconel 600 was superior to Haynes 25 at 1500 F (815 C) and 1700 F (921 C), the opposite was true at 1900 F (1030 C).

Mechanical Property Testing

To evaluate the effects of irradiation upon the mechanical properties of high temperature alloys, tensile specimens of Inconel 600, Inconel 625, Inconel 702, Inconel 718, Incoloy 800, Hastelloy C, Hastelloy N, Hastelloy R-235, Hastelloy X-280, and AISI 406 SS are being irradiated at 50 C (120 F), 280 C (536 F), 580 C (1076 F), and 740 C (1360 F) at various exposures. Of the two test temperatures to be used, room temperature and 700 C (1292 F), only the room temperature tests have been completed. A new high temperature tensile test furnace is presently being installed in the Radiometallurgy Laboratory for the 700 C (1292 F) tests.

The data showing the effects of irradiation temperature upon the room temperature tensile properties of Hastelloy X-280, Hastelloy N, Hastelloy C, Inconel 625, Inconel 718, and Hastelloy R-235 are given in Figures 4.6 through 4.11 and summarize the data to date on these alloys irradiated to an exposure of 5×10^{19} nvt ($E > 1$ Mev). Figure 4.6 shows the engineering tensile curves for Hastelloy X-280 irradiated at 740 C (1360 F) and 280 C (536 F). The irradiation at 740 C (1360 F) resulted in a 23% reduction in yield strength, a 34% reduction in uniform elongation, a 57.5% decrease in reduction in area, and a 5% increase in ultimate strength over those values for the 280 C (536 F) irradiation.

Similar results are shown in Figures 4.7 and 4.8 for Hastelloy N and Hastelloy C, solution hardenable alloys. Data shown in Figure 4.8 are for Hastelloy C irradiated at 580 C (1076 F) and 740 C (1360 F) and show a 12% decrease in yield strength, a 64% decrease in uniform elongation, and a 48% decrease in reduction in area. Very little effect in ultimate strength was found.

The data presented for Hastelloy N in Figure 4.7 show a marked change in properties of material irradiated at 740 C (1360 F) as compared to that irradiated at 280 C (536 F). These changes occur primarily in the ultimate strength and ductility properties of the material. A 30% reduction in ultimate strength was noted in the 740 C (1360 F) irradiation as compared to the 280 C (536 F) irradiation. Sharp decreases were also noted in the percent uniform elongation and reduction in area values in the 740 C (1360 F) irradiations.

bp 4.9

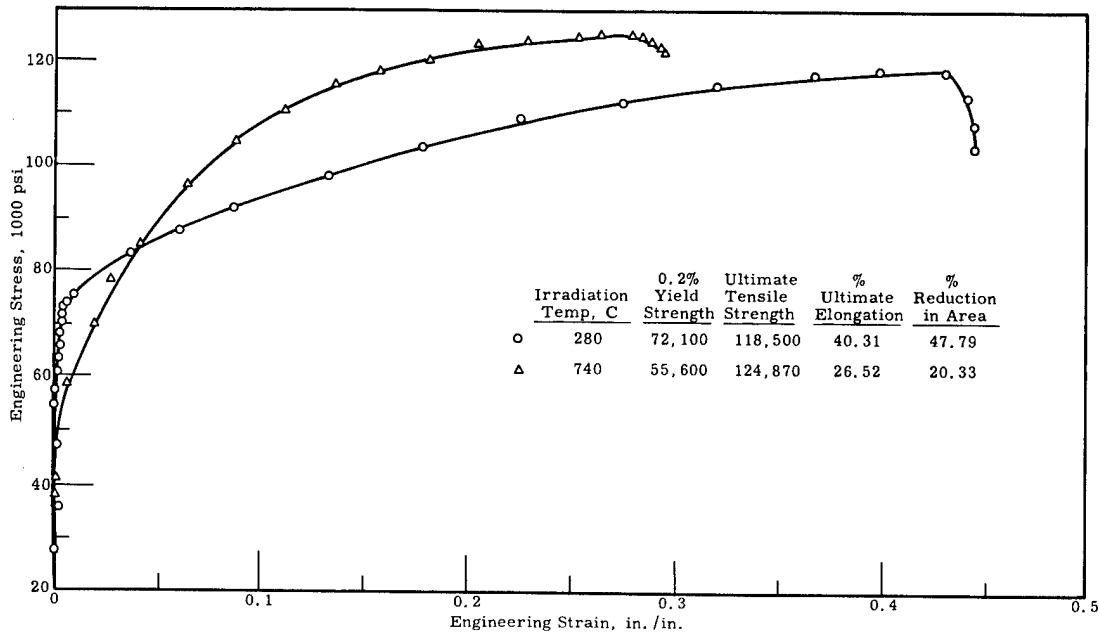


FIGURE 4.6

Effects of Irradiation Temperature
upon the Room Temperature Properties of Hastelloy X-280
Irradiated to an Exposure of 5×10^{19} nvt ($E > 1$ Mev)

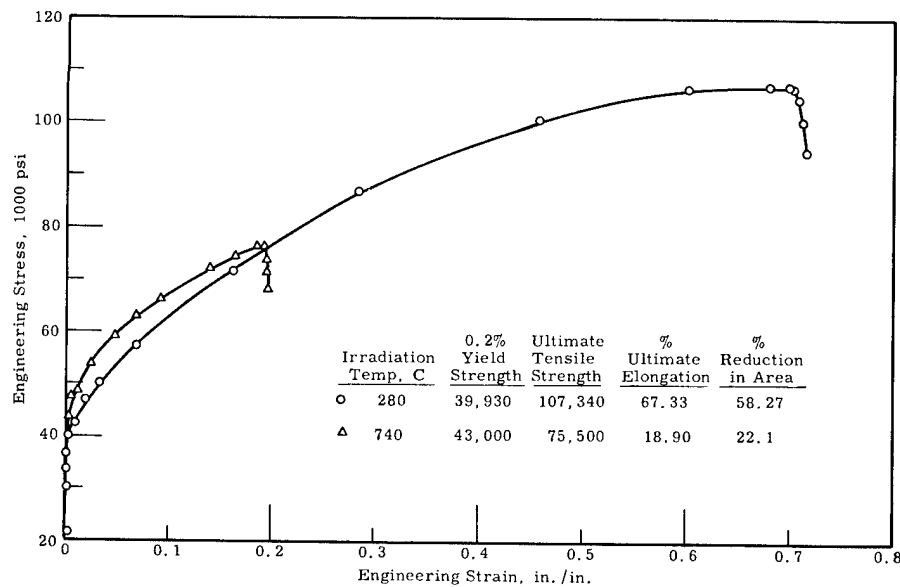


FIGURE 4.7

Effects of Irradiation Temperature
upon the Room Temperature Properties of Hastelloy N
Irradiated to an Exposure of 5×10^{19} nvt ($E > 1$ Mev)

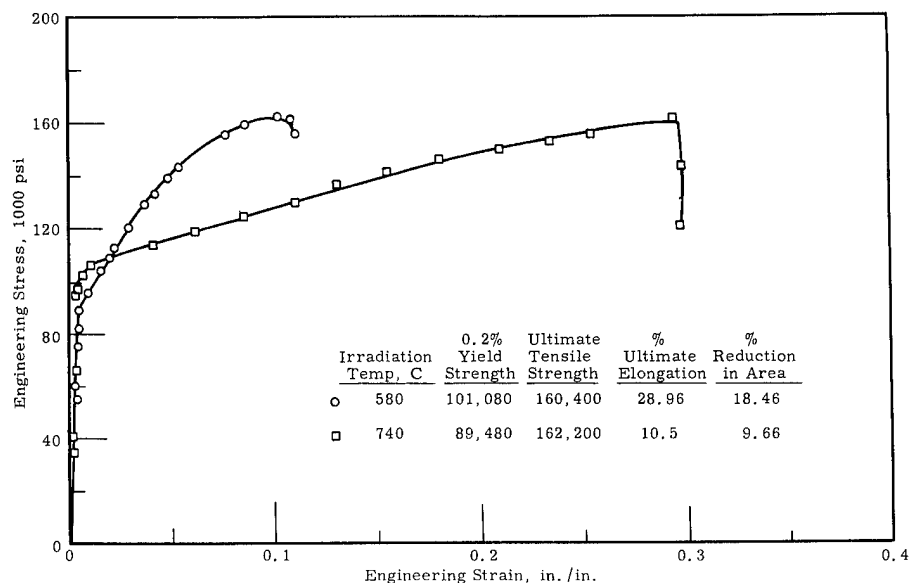


FIGURE 4.8

Effects of Irradiation Temperature upon the Room Temperature Properties of Hastelloy C Irradiated to an Exposure of 5×10^{19} nvt ($E > 1$ Mev)

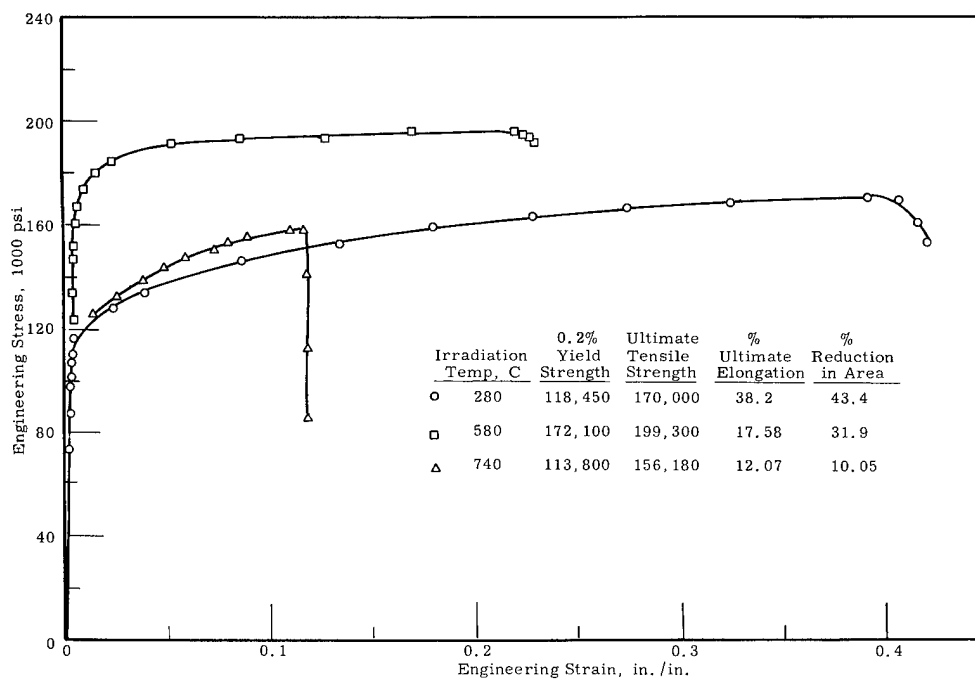


FIGURE 4.9

Effects of Irradiation Temperature upon the Room Temperature Properties of Inconel 625 Irradiated to an Exposure of 5×10^{19} nvt ($E > 1$ Mev)

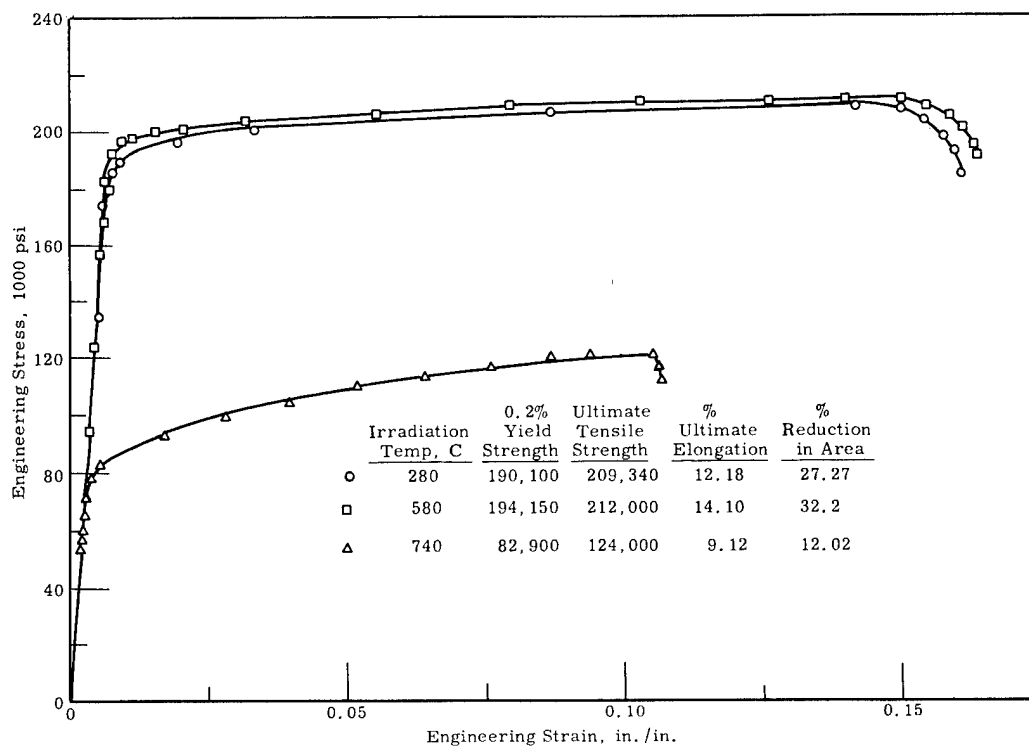


FIGURE 4.10

Effects of Irradiation Temperature
upon the Room Temperature Properties of Inconel 718
Irradiated to an Exposure of 5×10^{19} nvt ($E > 1$ Mev)

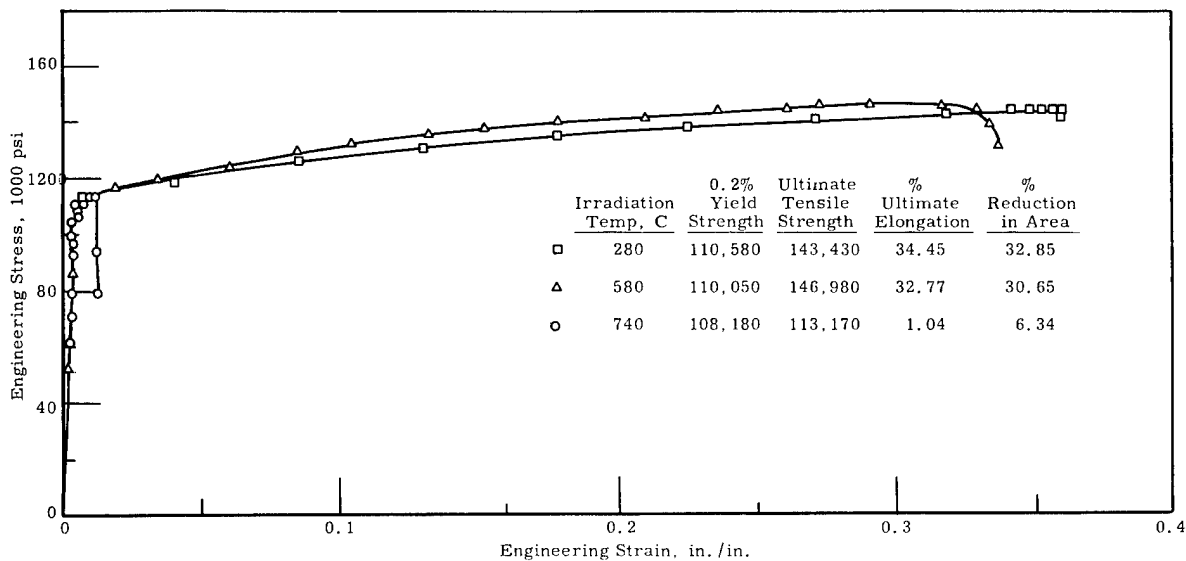


FIGURE 4.11

Effects of Irradiation Temperature
upon the Room Temperature Properties of Hastelloy R-235
Irradiated to an Exposure of 5×10^{19} nvt ($E > 1$ Mev)

The three precipitation hardenable alloys Inconel 625, Inconel 718, and Hastelloy R-235 have been irradiated at 280 C (536 F), 580 C (1076 F), and 740 C (1360 F) to an exposure of 5×10^{19} nvt ($E > 1$ Mev). Data for these alloys are shown in Figures 4.9, 4.10, and 4.11, respectively. In comparing these figures it is evident that a marked decrease in ductility is associated with the 740 C (1390 F) irradiation as compared to the 580 C (1076 F) and 280 C (536 F) irradiations. This is especially true in the case of Hastelloy R-235 where the percent uniform elongation decrease from 34.45% in the case of the 280 C (536 F) irradiation to 1.04% in the case of the 740 C (1390 F) irradiation. For both the Inconel 718 and Hastelloy R-235 very little change was found between the 280 C (536 F) and 580 C (1076 F) irradiations. Significant changes were, however, found in the case of the Inconel 625. These changes were noted in a 46% increase in yield strength, a 50% decrease in uniform elongation, and a 25% decrease in reduction in area.

In comparing the data presented in these figures it seems evident that the higher temperature irradiations affect the mechanical properties of these alloys to a considerable extent. In the case of the solution hardenable alloys considerable reductions in ductility were found between the 280 C (536 F) and 740 C (1390 F) irradiations. Two precipitation hardenable alloys, Hastelloy R-235 and Inconel 718 showed major differences only at the 740 C (1390 F) irradiation temperature. Little or no change between the 280 C (536 F) and 580 C (1076 F) exists indicating that excess thermal aging and radiation damage of the alloys has not yet occurred. At 740 C (1390 F) the effects of thermal aging and radiation damage have caused a marked reduction in the strength and ductility properties. This would seem to indicate a temperature limitation in the use of these alloys for reactor application and indicate the need for similar data on specimens irradiated above the normal aging temperatures for these alloys.

Specimens of Inconel 600 and Incoloy 800 were irradiated at 740 C (1390 F) to an exposure of 5×10^{19} nvt in the annealed, annealed and solution treated, and 20% cold-worked condition. In addition, specimens of Inconel 625 were irradiated at the same conditions in the annealed and in the solution treated and aged condition. The data obtained to date for these

alloys are shown in Figures 4.12 through 4.14. Recovery of the 20% cold-worked specimens of Inconel 600 and Incoloy 800 was almost complete at 740 C (1390 F) irradiation temperature as seen in Figures 4.12 and 4.13.

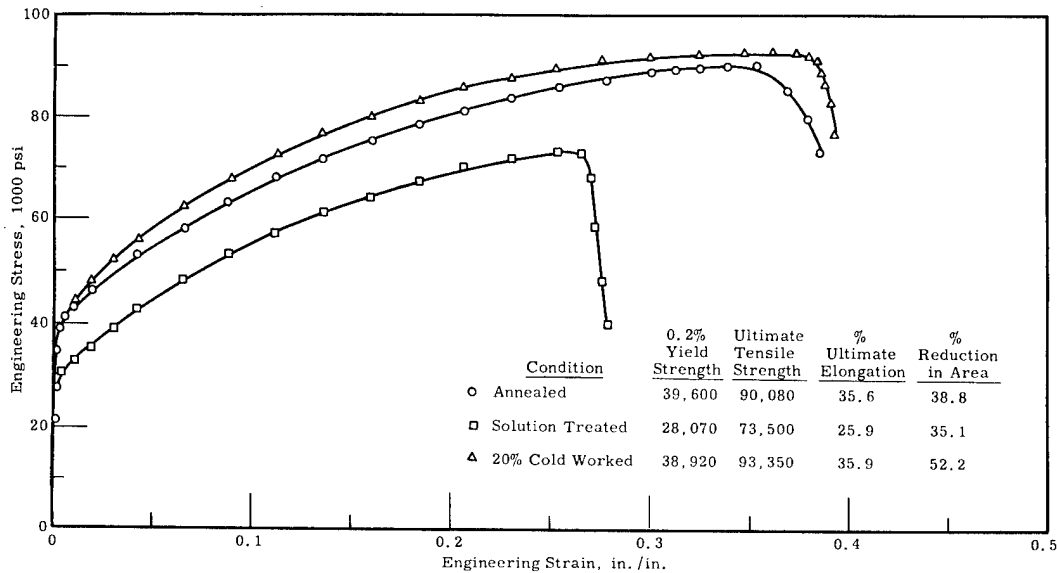


FIGURE 4.12

Effects of 740 C Irradiation on the Room Temperature Properties of Inconel 600 in the Annealed, Solution Heat Treated, and Cold-Worked Condition (5×10^{19} nvt, $E > 1$ Mev)

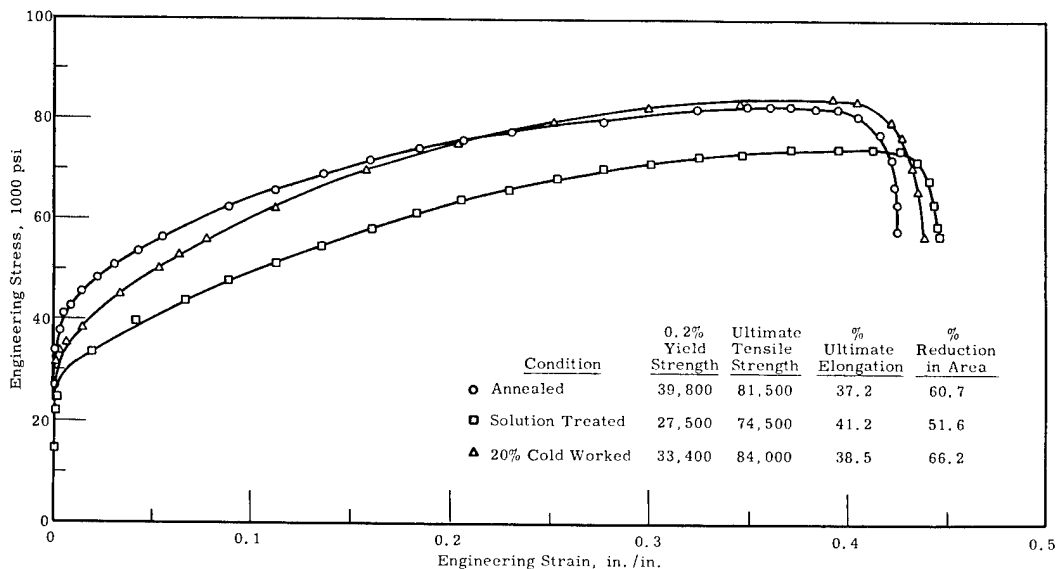


FIGURE 4.13

Effects of 740 C Irradiation on the Room Temperature Properties of Incoloy 800 in the Annealed, Solution Heat Treated, and Cold-Worked Condition (5×10^{19} nvt, $E > 1$ Mev)

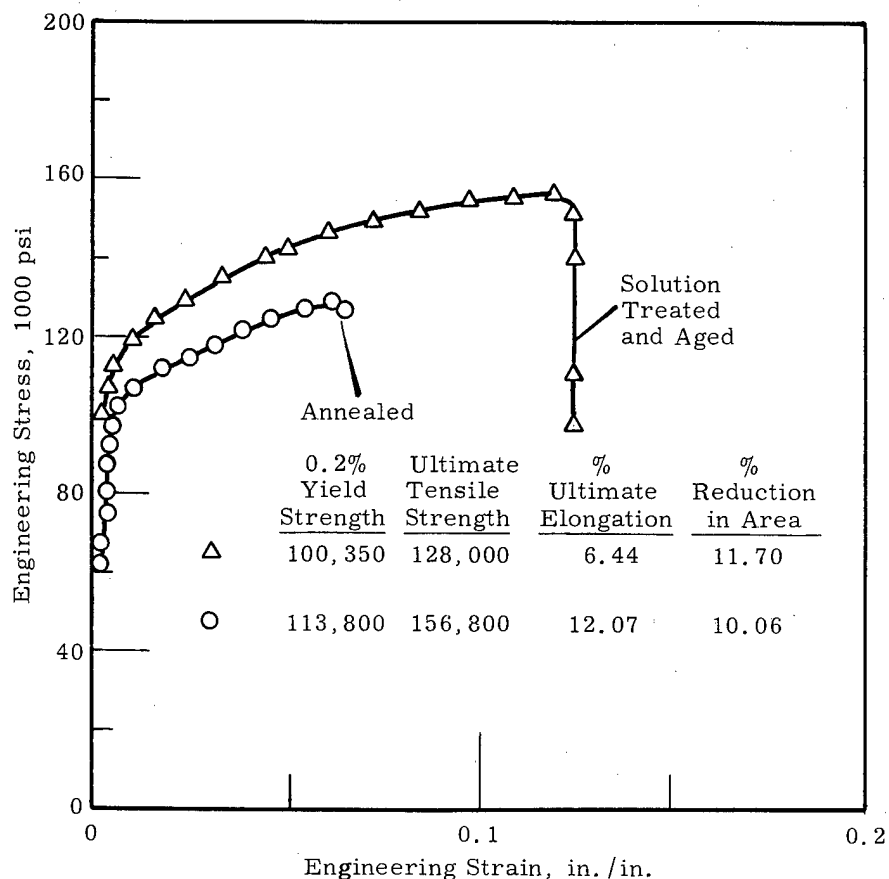


FIGURE 4.14

Effects of Irradiation upon the Room Temperature Properties of Inconel 625 in the Annealed and Solution Treated, Aged Condition Irradiated at 740 C to an Exposure of 5×10^{19} nvt ($E > 1$ Mev)

Comparison of the annealed and heat treated conditions of Inconel 625 in Figure 4.14 shows a stronger and more ductile material for the solution treated and aged condition. While the reduction in area values were about the same, the percent uniform elongation value in the annealed condition was only 6.4% as compared to 12% in the heat-treated condition. Comparison of all these data with the out-of-reactor control data will be made in the near future as the data become available.

IN-REACTOR MEASUREMENTS OF MECHANICAL PROPERTIES -
J. J. Holmes, D. H. Nyman, and J. A. Williams

The objective of this in-reactor measurements program is to define the effects of fast neutron irradiation on the mechanical properties of reactor structural materials. A study of in-reactor creep of 20% cold-worked Zircaloy-2 has been completed. At the present time the in-reactor creep properties of AISI 304 SS are being investigated.

In-Reactor Measurements

Two in-reactor creep tests at 500 C (932 F) and stresses of 20,000 and 30,000 psi are in progress. The test at 20,000 psi is showing a creep rate below the minimum resolvable rate of 2.5×10^{-7} /hr. During the one outage which has occurred in the course of this test a slight increase in creep rate was noted, but it is not possible to say at this time that the increase is statistically significant. A long outage period will be required to determine the significance of the indicated increase. The out-of-reactor test at 20,000 psi and 500 C (932 F) failed prematurely after 150 hr of testing. This premature failure must not be considered as typical of AISI 304 SS since data from the literature show that failure could not be even realized at 20,000 psi and 500 C (932 F) for times as great as 10^5 hr. A second out-of-reactor test at 20,000 psi and 500 C (932 F) is being prepared.

The in-reactor test at 30,000 psi and 500 C (932 F) showed a lower creep rate than the out-of-reactor test up to about 45 hr when a controller failure caused a 75 C (103 F) increase in temperature for about 5 min in the in-reactor test. After returning to 500 C (932 F) the creep rate observed was 4.5×10^{-7} /hr. The out-of-reactor test shows a creep rate of 2.6×10^{-6} /hr at comparable times. It should be pointed out that the out-of-reactor and in-reactor tests are not directly comparable because of the temperature pulse of the in-reactor test. If

$$\epsilon = f(\theta), \quad \theta = \exp -\frac{\Delta H}{Rt}$$

t = time hours

ΔH = activation energy for creep

Accurate comparison between the in-reactor and out-of-reactor tests can be made when a value for ΔH becomes available. In the meantime another out-of-reactor test will be started which will be given the same temperature pulse as that observed in-reactor. This should provide a direct comparison.

An in-reactor test at 30,000 psi stress and 550 C (1022 F) has been conducted. The test was terminated after about 600 hr of testing because of a heater failure. Up to that point the in-reactor and out-of-reactor creep curves were almost identical. No significant difference was observed.

IRRADIATION FACILITIES OPERATION - J. E. Irvin

The purpose of this phase of the program is to provide for the timely accomplishment of irradiating, testing, and subsequent processing of the data obtained from a number of different structural materials. Irradiations will be performed in aqueous, gaseous, and molten metal environments. Elevated temperature irradiations and tests will be emphasized. Special tests applicable to both irradiated and unirradiated specimens will be developed.

Facilities Operation

With the conclusion of ETR Cycles 62 and 63, three additional quadrants were discharged from the G-7 Hot Water Loop. The contents and estimated neutron fluxes and exposures (> 1 Mev) for these quadrants are given in Table 4.1. One quadrant of specimens exposed in the out-of-reactor loop during Cycle 60 was also discharged. Summaries of the operating history of the ETR, the G-7 Hot Water Loop, and the out-of-reactor loop are given in Tables 4.2 and 4.3.

During the latter part of ETR Cycle 62, a flow control valve leading to one of the heat exchangers became inoperative. With the valve stuck in one position, the maximum temperature obtainable in the G-7 Loop was between 450 F (232 C) and 500 F (260 C). Therefore, the temperature efficiency for this cycle was only 57% which is far below that normally achieved. The valve was replaced during the ETR Cycle 63 shutdown and normal operation was resumed during the following cycle.

TABLE 4.1

QUADRANT DISCHARGES FOR ETR CYCLE 63

<u>Quadrant Number</u>	<u>Number and Type of Specimen</u>	<u>Estimated Flux, nv*</u>	<u>Estimated Exposure, nvt*</u>
104	18 Nickel-Base Tensiles	4.5×10^{13}	8.2×10^{20}
128	18 Nickel-Base Tensiles	6.5×10^{13}	7.2×10^{20}
135	18 Nickel-Base Tensiles	5.5×10^{13}	5.0×10^{20}

* Neutrons with energies greater than 1 Mev

Total number of specimens discharged, Cycles 62 and 63 = 54

Total number of specimens discharged to date = 2016

TABLE 4.2

OPERATING HISTORY OF ETR AND G-7 LOOP FACILITY

<u>Operating History</u>	<u>Cycle Number</u>	
	<u>61</u>	<u>62</u>
1. Reactor History		
Startup ^(a)	1-27-64	3-9-64
End of Cycle	3-1-64	4-11-64
Megawatt Days	4832	4903
Effective Days at 175 Mw	27.6	28.02
Number of Scrams ^(b)	12	7
Number of Shutdowns	3	2
2. G-7 Loop History		
Maximum Temperature	*	535 F
Effective Days Above 200 F	-	29.1
Effective Days at		
Operating Temperature	-	16.6
Operating Efficiency ^(c)	-	100.4%
Temperature Efficiency ^(d)	-	57.2%
(a) Includes flux run		
(b) Power drops below half-full power with immediate recovery		
(c) Effective days of loop operation above 200 F with respect to effective days of reaction operation at 175 Mw		
(d) Effective days of operation between 500 and 550 F with respect to days of operation above 200 F		
* The G-7 Loop was not operative during this cycle.		

TABLE 4.3

TEMPERATURE-TIME DISCHARGE SCHEDULE
FOR OUT-OF-REACTOR LOOP

<u>Loop History</u>	<u>Cycle Number</u>
	<u>60</u>
1. Time at Temperature (in hours)	
392 F	17.2
425 F	2.8
475 F	24.5
540 F	660.4
Total Time (in hours)	704.9
2. Specimen Discharge, Type and Number	
Nickel-Base (Tensiles)	12
Total Number of Specimens Discharged*	12
Total Number of Specimens Discharged to Date*	888
* Excludes corrosion blanks	

IRRADIATION DAMAGE TO ZIRCALOY-2 - J. E. Irvin

The purpose of this phase of the program is to investigate the combined effects of irradiation and reactor environment on the mechanical properties of Zircaloy-2. Special attention will be given to the determination of mechanical property changes produced by irradiation at elevated temperatures. Tests employing notched specimens will be used to determine the brittle fracture tendencies of the material.

Surveillance of NPR Tubing

Tensile tests were performed on specimens fabricated from NPR Zircaloy-2 tubes. Irradiated and unirradiated specimens were tested at room temperature after exposures in both the ETR G-7 Hot Water Loop and the out-of-reactor loop. The results obtained from these tests are given in Tables 4.4 and 4.5. Additional tests were performed at 300 C (572 F) and are currently being processed. Metallographic studies are in progress to determine the degree of hydride formation which occurs after prolonged exposures at approximately 300 C (572 F).

Several specimens were fabricated from each of three tubes for texture studies. The specimens are illustrated in Figure 4.15. A spiral-scanning technique with the pole figure goniometer shown in Figure 4.16 was used to determine the pole figures. The results of this study are given in Figures 4.17 through 4.26. The outer and inner surfaces of the tubes are located approximately at the zero and 180 degree positions in the pole figures, respectively.

Generally, the texture of these tubes is one in which there is a relatively strong preference for alignment of the (0002) basal planes parallel to the tube axis. There is also a definite preference for alignment of the $(10\bar{1}0)$ and the $(11\bar{2}0)$ prism planes perpendicular to the tube axis. The $(10\bar{1}1)$ pyramid planes are approximately equally distributed with the $\langle 10\bar{1}1 \rangle$ direction being inclined at an angle of about 30 degrees with the tube axis.

TABLE 4.4

**TENSILE PROPERTIES OF NPR ZIRCALOY-2 TUBING
IRRADIATED IN THE G-7 HOT WATER LOOP
(Irradiation temperature ~282 C)**

Material	Working Direction*	Material Condition**	Test Temp., C	Strength, 10 ³ psi 0.2% YS UTS	Percent Strain Uniform Necking	Reduction of Area, %	Plastic Work, ft-lb	Number of Tests
Quadrant 124 (2.2 x 10 ²⁰)***								
Zircaloy-2 NPR (AT-50)	T	30%	RT	102.9	107.9	3.1	3.4	31.6
Zircaloy-2 NPR (AT-50)	N	30%	RT	102.7	108.2	3.7	3.5	35.5
Zircaloy-2 NPR (HT-37)	T	16%	RT	97.9	104.7	2.9	1.6	27.5
Zircaloy-2 NPR (HT-37)	N	16%	RT	98.1	106.4	3.7	3.0	29.3
Zircaloy-2 NPR (CT-19)	T	14%	RT	94.7	100.3	3.0	3.0	31.4
Zircaloy-2 NPR (CT-19)	N	14%	RT	92.8	98.4	3.1	3.0	28.7
Quadrant 126 (5.4 x 10 ²⁰)***								
Zircaloy-2 NPR (AT-50)	T	30%	RT	111.5	113.3	2.5	3.4	31.8
Zircaloy-2 NPR (AT-50)	N	30%	RT	107.2	115.2	0.5	6.1	30.4
Zircaloy-2 NPR (HT-37)	T	16%	RT	103.8	110.7	2.7	2.0	28.6
Zircaloy-2 NPR (HT-37)	N	16%	RT	104.7	110.7	2.8	2.0	28.8
Zircaloy-2 NPR (CT-19)	T	14%	RT	104.8	107.0	1.5	2.5	28.0
Zircaloy-2 NPR (CT-19)	N	14%	RT	105.4	108.1	1.3	4.2	28.1

* All specimen axes correspond to tube axes. The "T" and "N" refer to the orientation of the specimen thickness.

** Amount of cold reduction prior to any autoclaving treatments

*** Estimated integrated exposure, nvt (> 1 Mev)

TABLE 4.5

**TENSILE PROPERTIES OF NPR ZIRCALOY-2 TUBING
EXPOSED IN OUT-OF-REACTOR LOOP**

Material	Working Direction	Material Condition	Test Temp., C	Strength, 10 ³ psi 0.2% YS UTS	Percent Strain Uniform Necking	Reduction of Area, %	Plastic Work, ft-lb	Number of Tests
Quadrant 116 (668.6 hr)*								
Zircaloy-2 NPR (AT-50)	T	30%	RT	69.0	88.5	9.0	9.1	45.0
Zircaloy-2 NPR (AT-50)	N	30%	RT	69.0	89.5	10.0	8.0	39.1
Zircaloy-2 NPR (HT-37)	T	16%	RT	65.2	88.3	9.5	5.5	34.5
Zircaloy-2 NPR (HT-37)	N	16%	RT	64.3	88.4	9.4	6.1	35.2
Zircaloy-2 NPR (CT-19)	T	14%	RT	56.8	77.0	10.7	5.9	38.9
Zircaloy-2 NPR (CT-19)	N	14%	RT	58.8	79.7	11.9	9.1	39.0
Quadrant 126 (1629 hr)*								
Zircaloy-2 NPR (AT-50)	T	30%	RT	69.5	90.2	9.7	7.7	38.9
Zircaloy-2 NPR (AT-50)	N	30%	RT	67.2	88.3	9.8	7.5	39.6
Zircaloy-2 NPR (HT-37)	T	16%	RT	64.8	88.8	12.3	6.7	36.6
Zircaloy-2 NPR (HT-37)	N	16%	RT	64.4	87.6	9.5	3.8	35.9
Zircaloy-2 NPR (CT-19)	T	14%	RT	62.3	76.0	8.4	4.6	39.6
Zircaloy-2 NPR (CT-19)	N	14%	RT	55.4	76.1	10.2	5.9	42.0
Zircaloy-2 NPR (CT-19)	N	14%	RT	55.4	76.1	10.2	5.9	42.0

* Total hours of exposure above 200 C (392 F)

The variation in tube fabrication history is quite pronounced and undoubtedly influences the resulting texture. Extrusion ratios varied from 8:1 to 29:1 and extrusion temperatures varied by at least 300 F (149 C). The complete fabrication history of these tubes is not presently available, but will be provided at a later date. Additional tests will be performed to better establish the texture of these tubes.

MATERIAL: Zircaloy-2 Tubing, 0.250 in. Thick $\begin{matrix} +0.012 \\ -0.000 \end{matrix}$

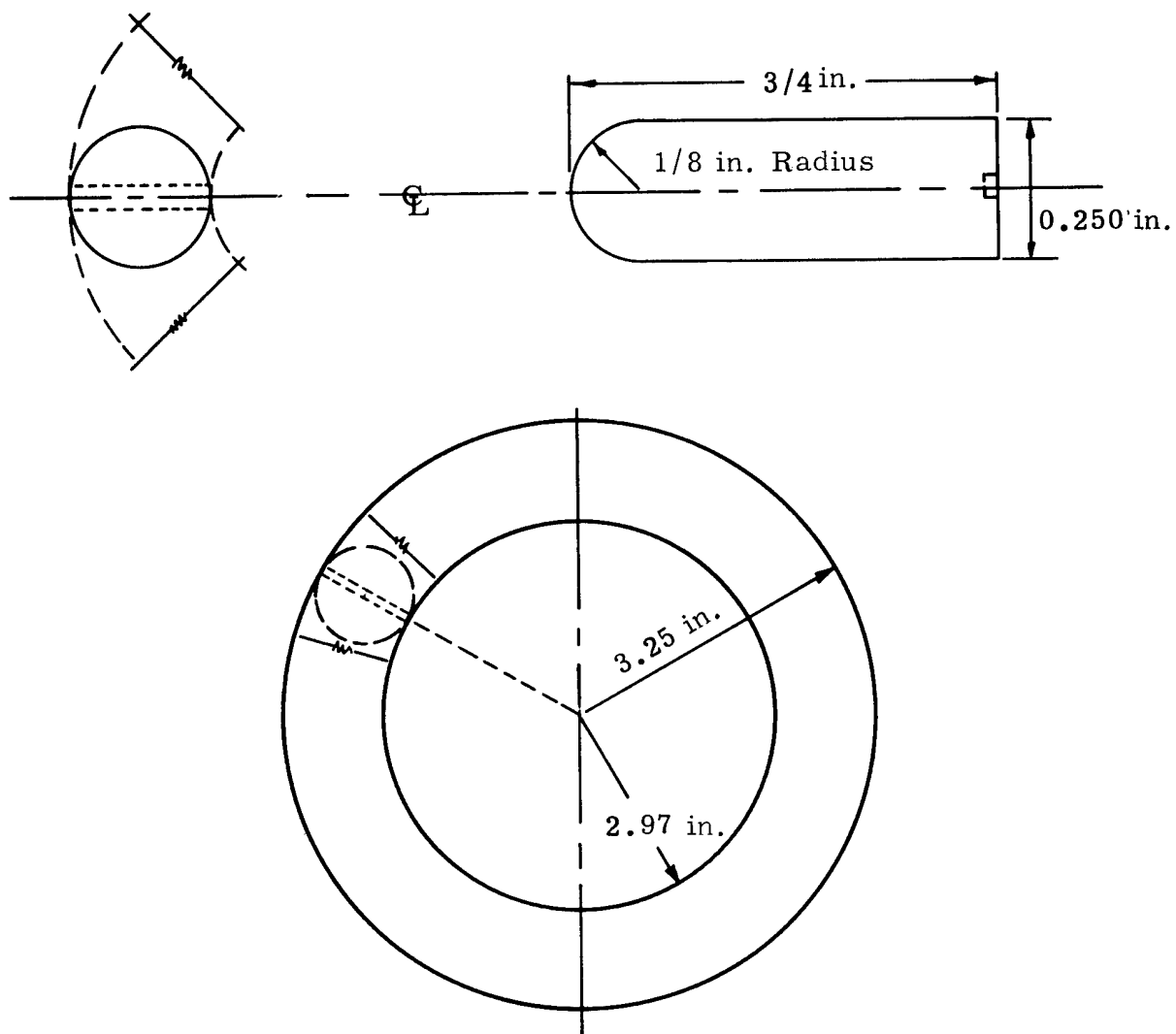


FIGURE 4.15

Specimen for Texture Study of NPR Tubing

Neg. No. 0631846-11

AEC-GE RICHLAND, WASH.

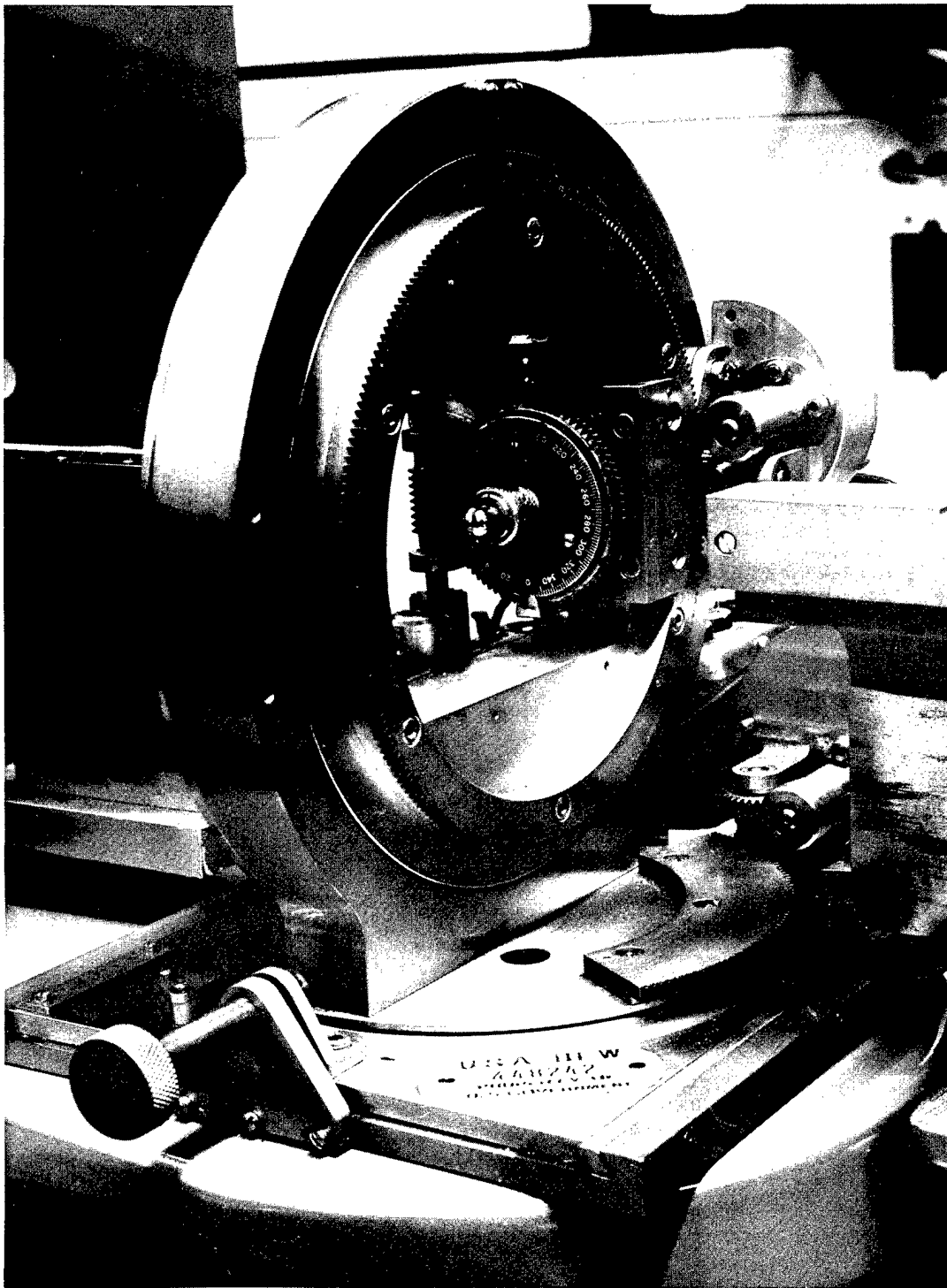


FIGURE 4.16

Pole Figure Goniometer

Neg. No. 0630519-1
AEC-GE RICHLAND, WASH.

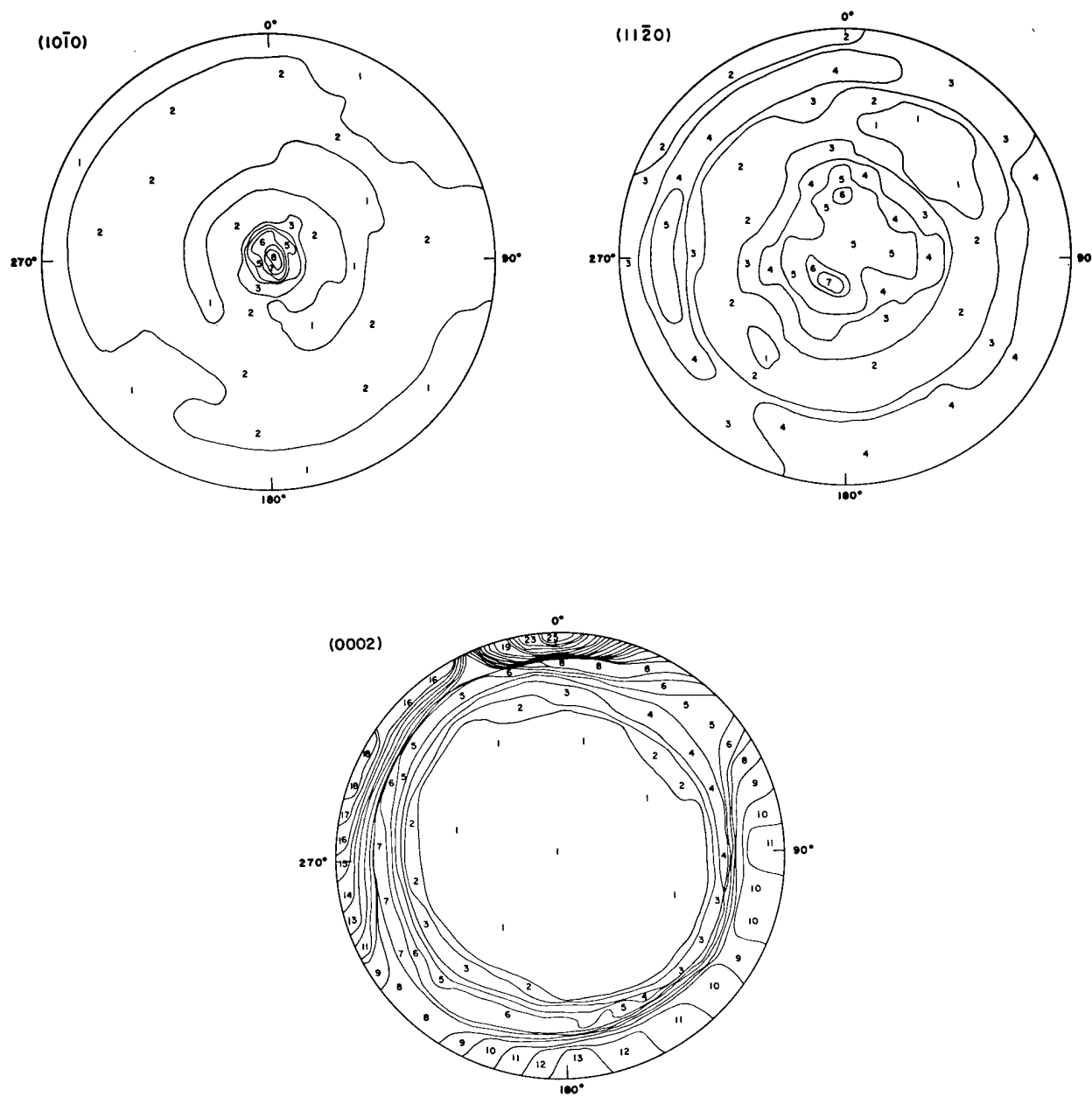


FIGURE 4.17
Pole Figures from Specimen 1
from NPR Tube AT-50

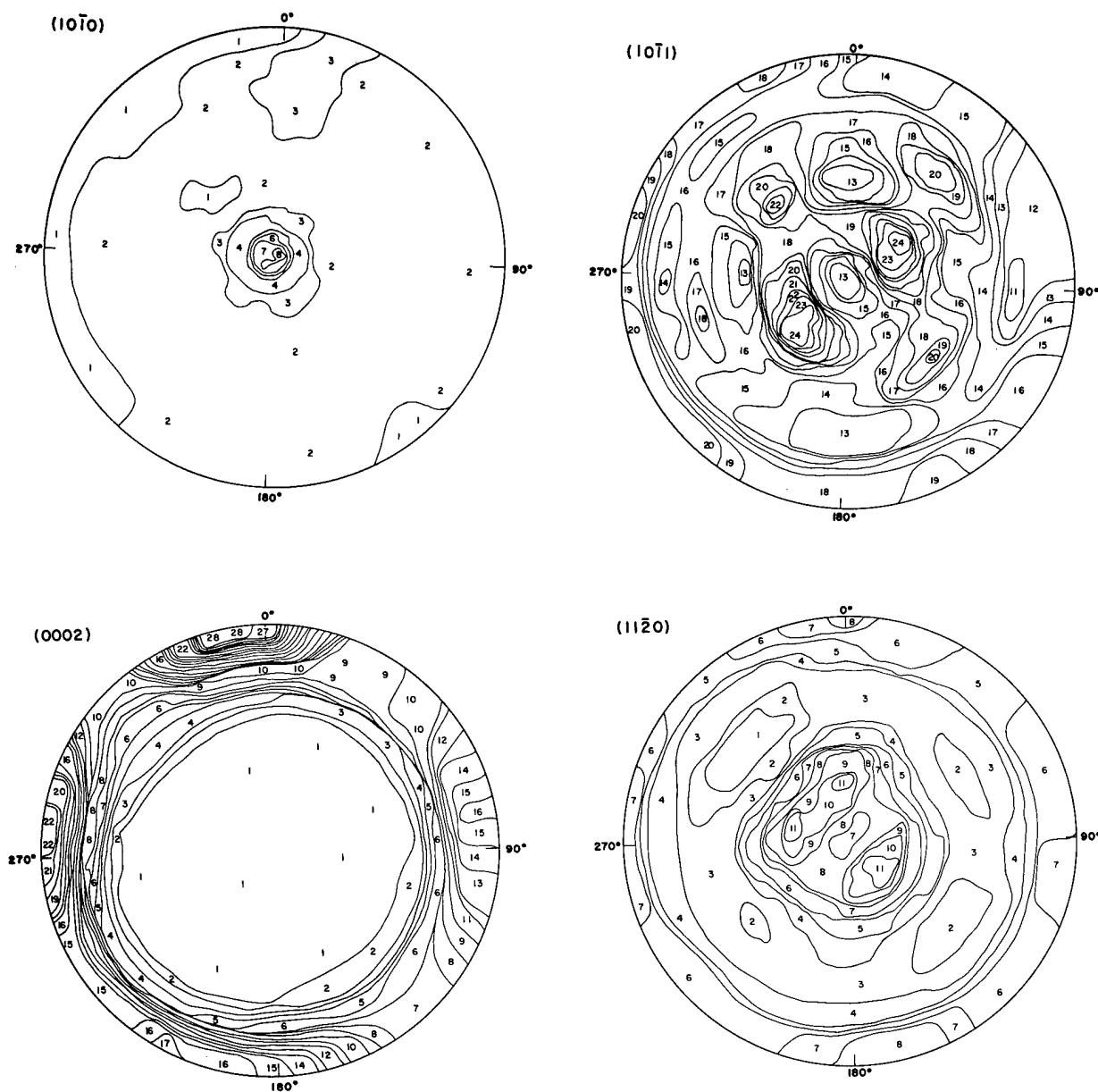


FIGURE 4.18

Pole Figures from Specimen 2
from NPR Tube AT-50

Neg. No. 0631846-2

AEC-GE RICHLAND, WASH.

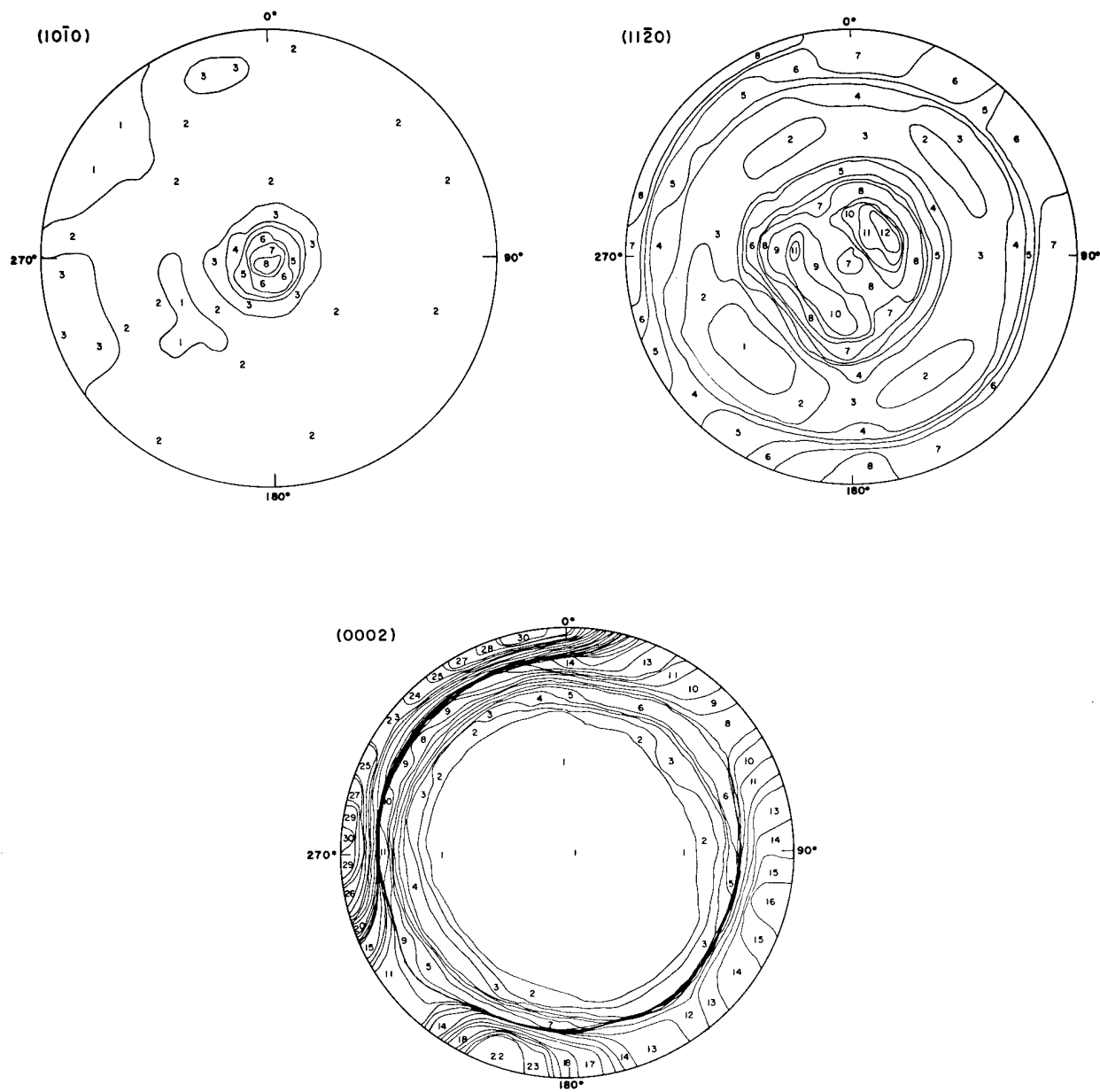


FIGURE 4. 19
Pole Figures from Specimen 3
from NPR Tube AT-50

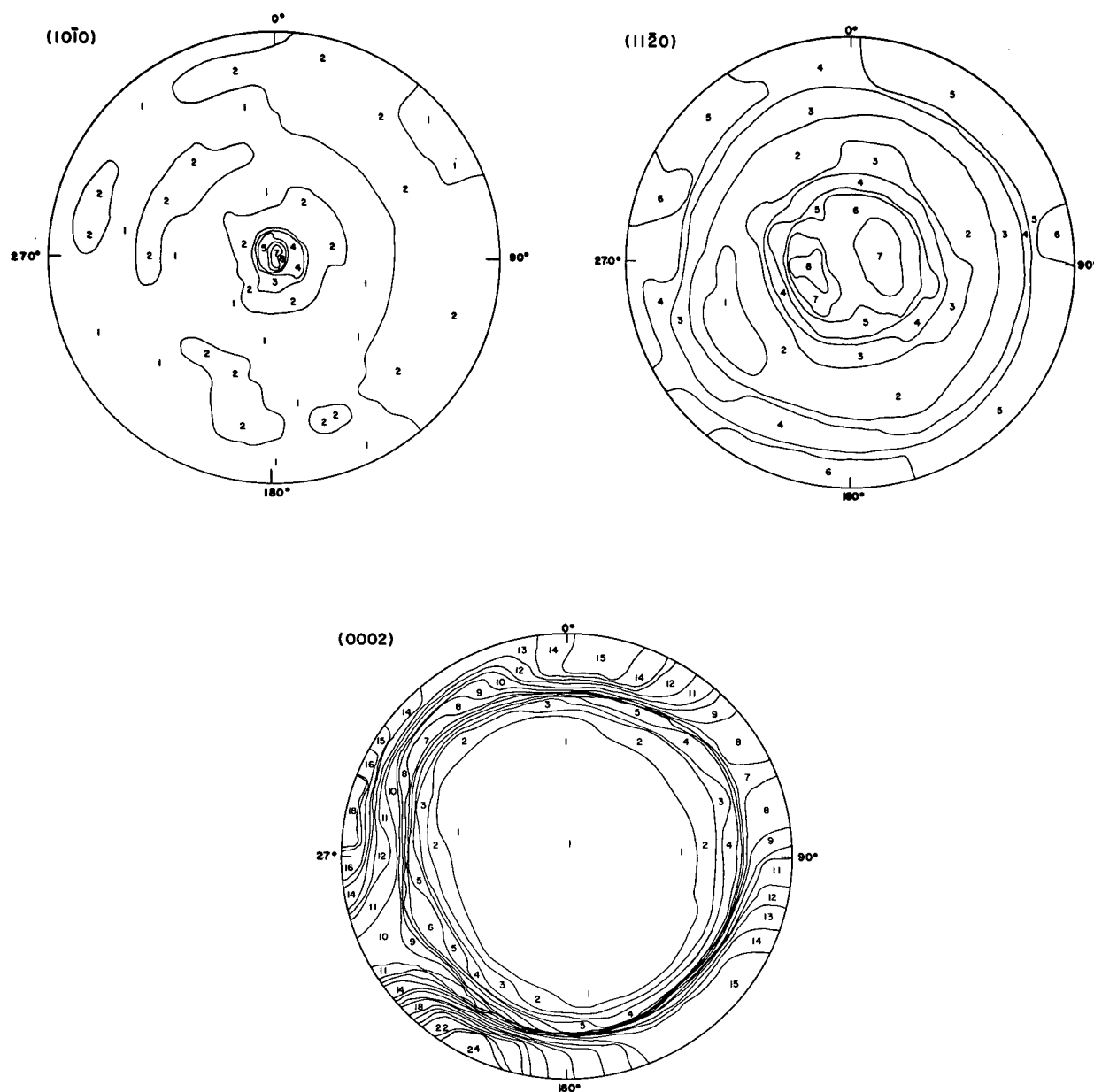


FIGURE 4.20
Pole Figures from Specimen 4
from NPR Tube AT-40

Neg. No. 0631846-3

AEC-GE RICHLAND, WASH.

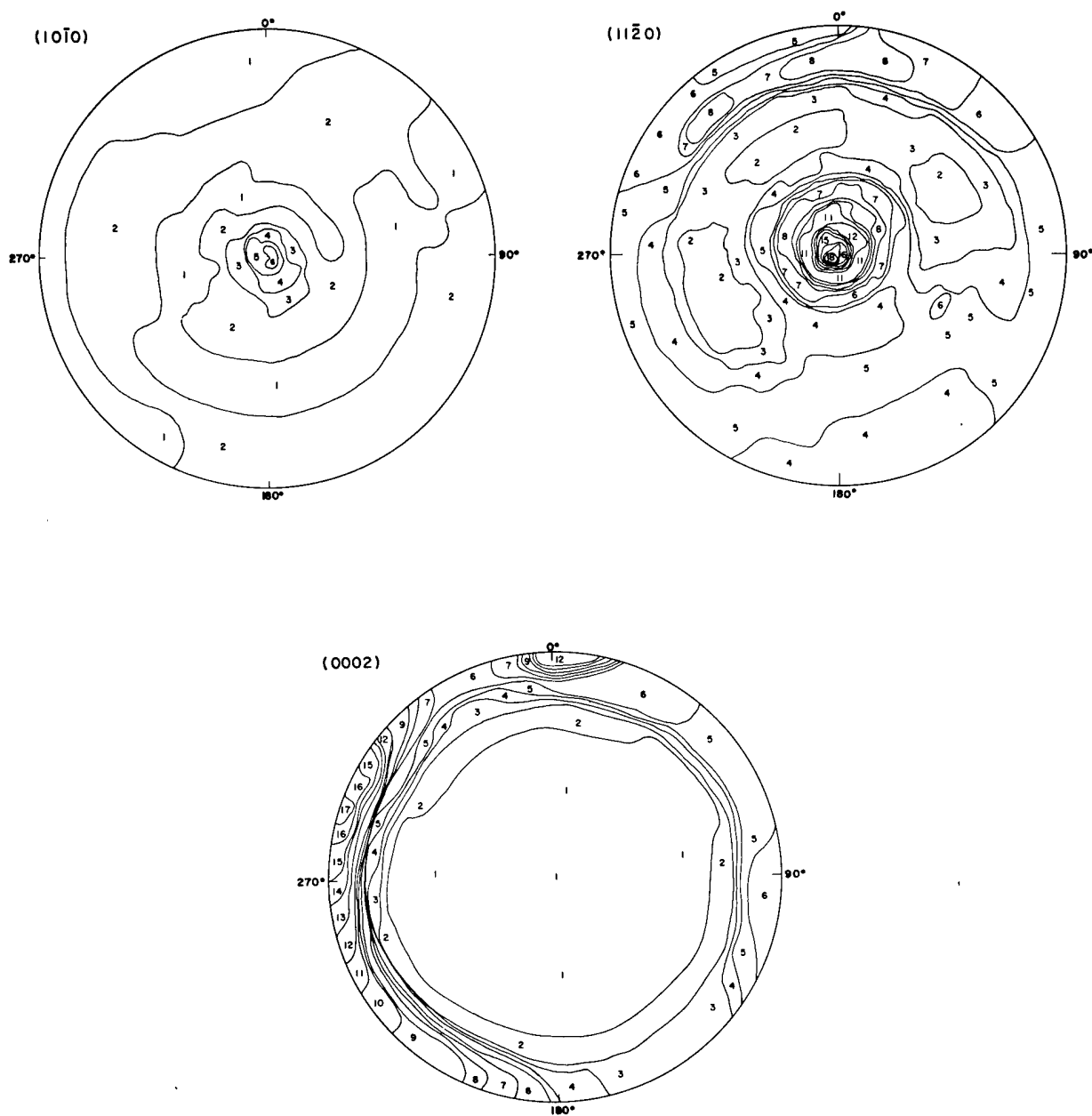


FIGURE 4.21
Pole Figures from Specimen 1
from NPR Tube HT-37

Neg. No. 0631846-6

AEC-GE RICHLAND, WASH.

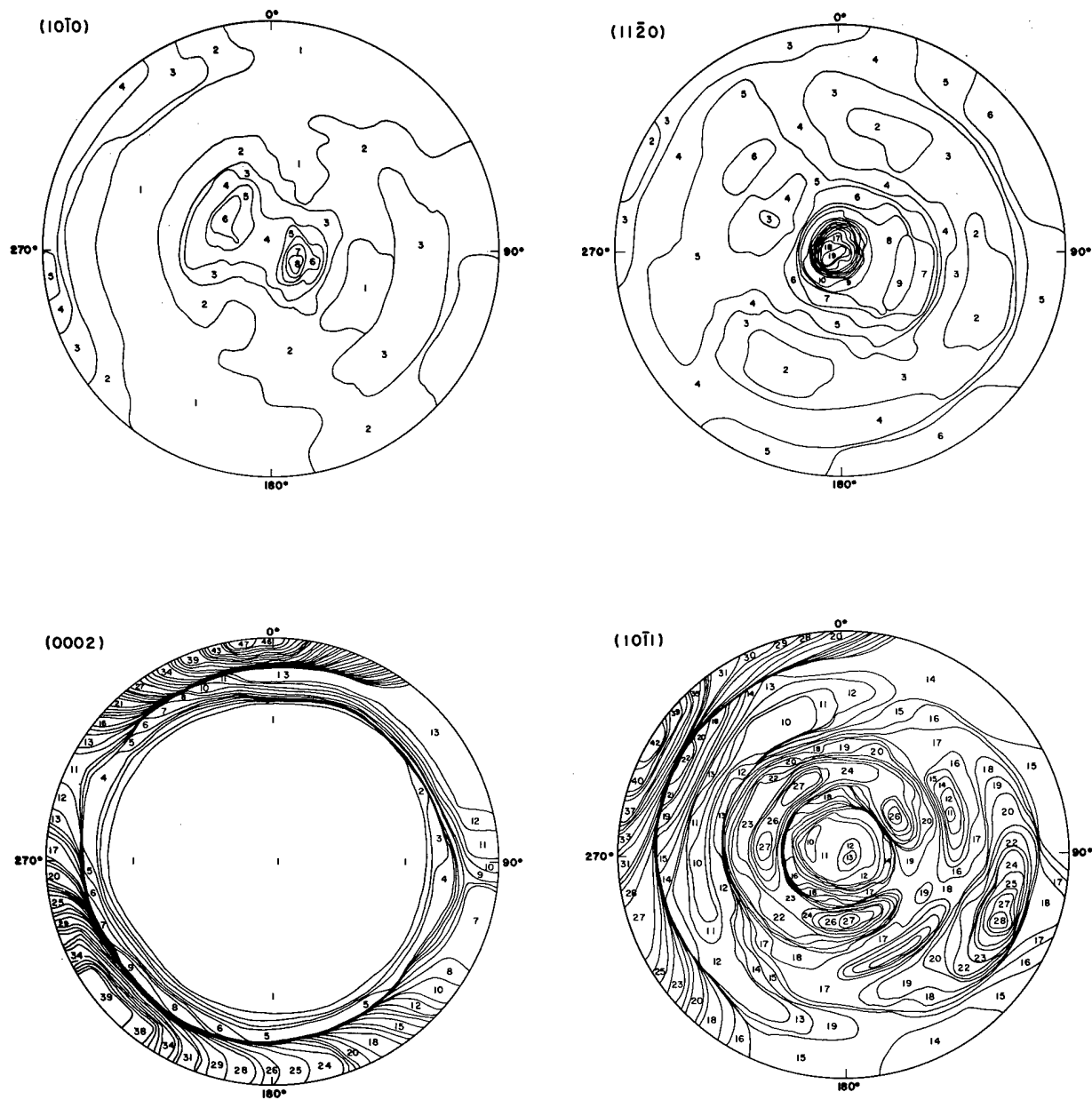


FIGURE 4.22

Pole Figures from Specimen 2
from NPR Tube HT-37

Neg. No. 0631846-9

AEC-GE RICHLAND, WASH.

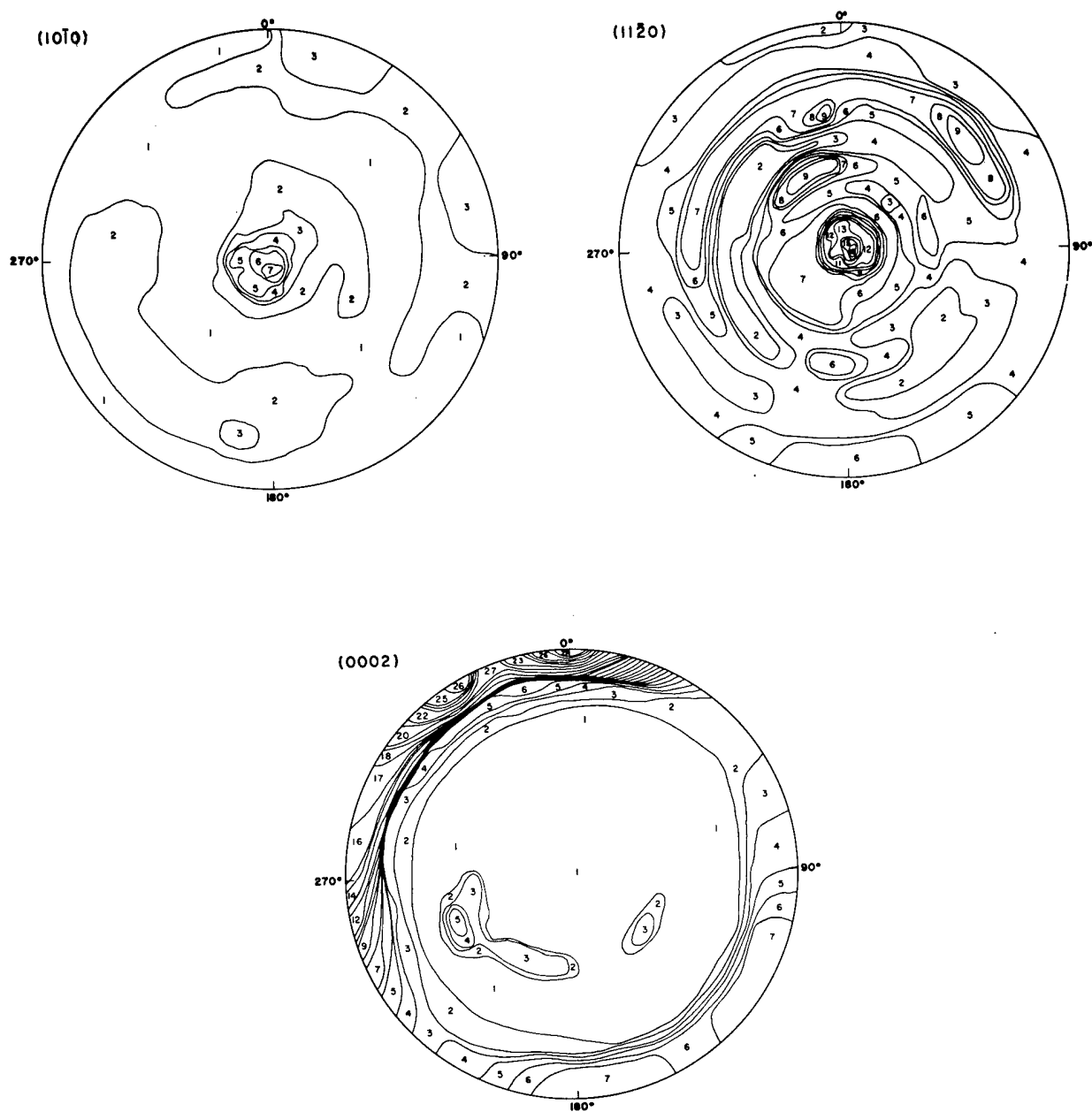


FIGURE 4.23
Pole Figures from Specimen 3
from NPR Tube HT-37

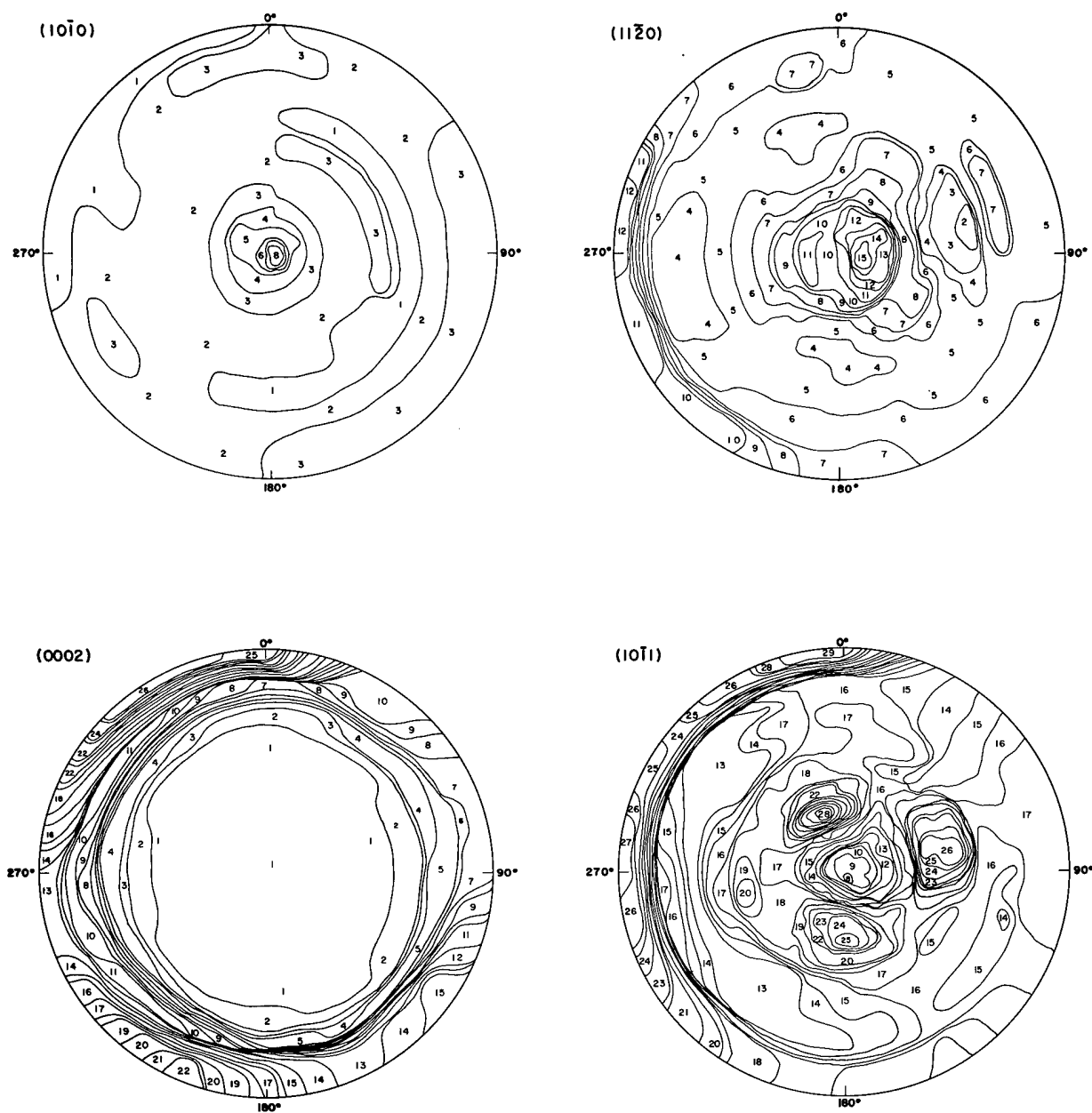


FIGURE 4.24

Pole Figures from Specimen 1
from NPR Tube CT-19

Neg. No. 0631846-5

AEC-GE RICHLAND, WASH.

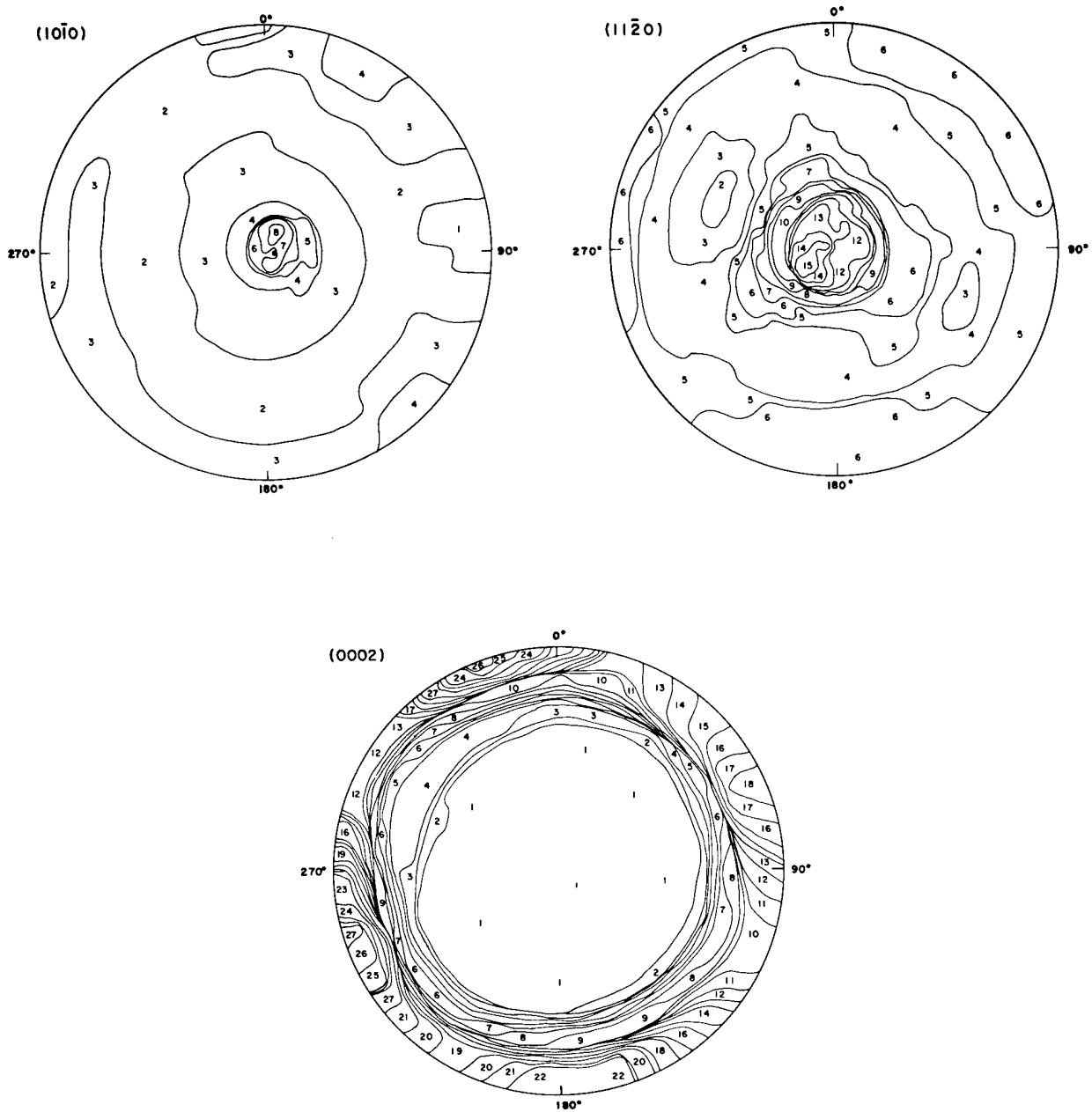


FIGURE 4. 25
Pole Figures from Specimen 2
from NPR Tube CT-19

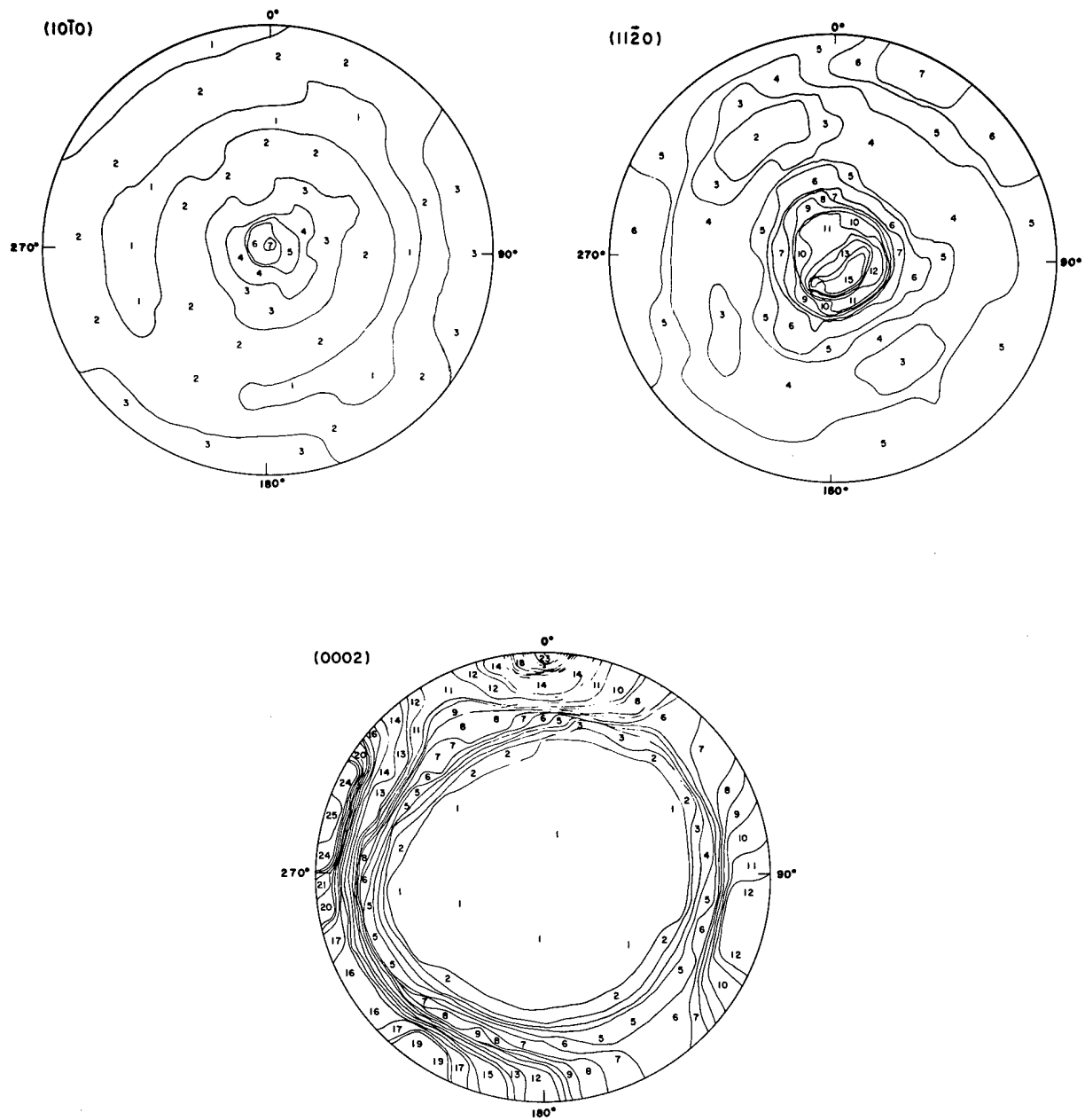


FIGURE 4.26

Pole Figures from Specimen 3
from NPR Tube CT-19

IRRADIATION DAMAGE TO STAINLESS STEELS - J. E. Irvin

The purpose of this phase of the program is to determine the combined effects of irradiation and reactor environment on stainless steels. Changes in mechanical properties will be determined for several irradiation and testing temperatures. Particular emphasis will be placed on establishing under what conditions of service these alloys are metallurgically unstable and to determine the mechanisms by which radiation-induced property changes occur.

Austenitic Stainless Steels

The results of tensile tests performed at room temperature on AISI 348 and 304 SS specimens irradiated at 50 C (122 F) and 290 C (554 F) are illustrated graphically in Figures 4.27 through 4.30. Although the increase in strength and decrease in ductility is initially greater for these materials irradiated at 50 C (122 F), a crossover occurs at relatively nominal exposures. Thereafter, the 290 C (554 F) irradiations show a greater increase in strength and decrease in ductility than the specimens irradiated at 50 C (122 F). A paper⁽¹⁾ was given at the ASTM "Symposium on Flow and Fracture Behavior of Metals and Alloys in a Nuclear Environment," in Chicago, Illinois, in which the conclusions drawn from data obtained to date were presented.

The amount of mechanical properties recovery as a function of annealing temperature for 25% cold-worked AISI 348 SS is given in Figure 4.31. Several specimens were annealed at each temperature from 350 C (662 F) to 850 C (1562 F) for 4 hr. A slight increase in strength and decrease in ductility are observed for specimens annealed between 350 C (662 F) and about 600 C (1115 F) as compared with the cold-worked condition. These property changes have also been observed for both annealed and 25% cold-worked AISI 348 and 304 SS exposed in the out-of-reactor loop at 282 C (540 F) for several hundred hours. The strengthening is due

-
1. J. E. Irvin, A. L. Bement, and R. G. Hoagland. The Combined Effects of Temperature and Irradiation on the Mechanical Properties of Austenitic Stainless Steels, HW-SA-3221. April 15, 1964.

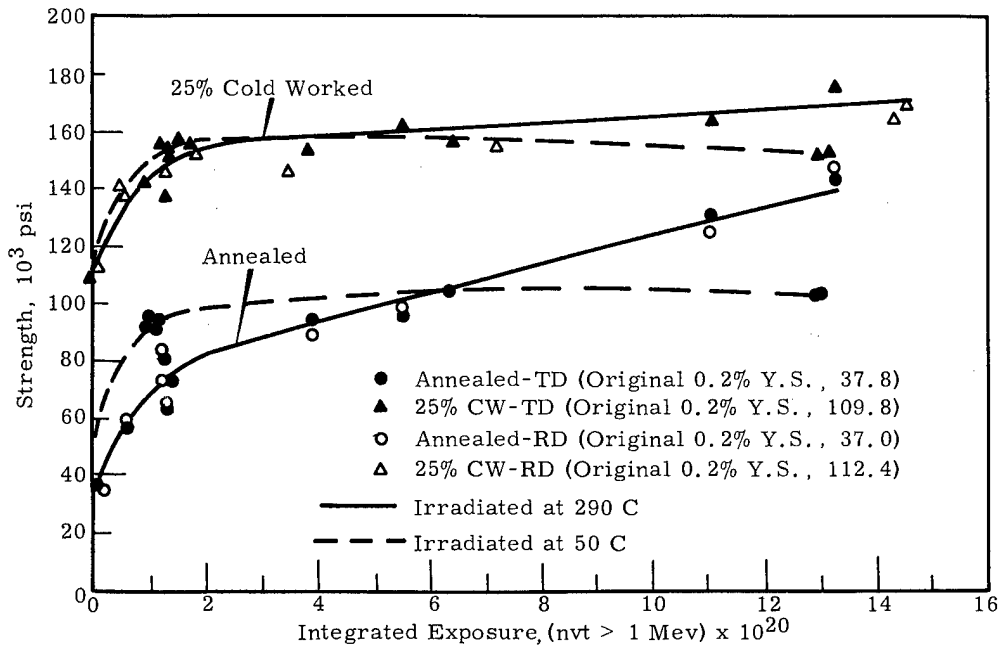


FIGURE 4.27

Effects of Irradiation on Room Temperature Yield Strength of AISI 348 Stainless Steel

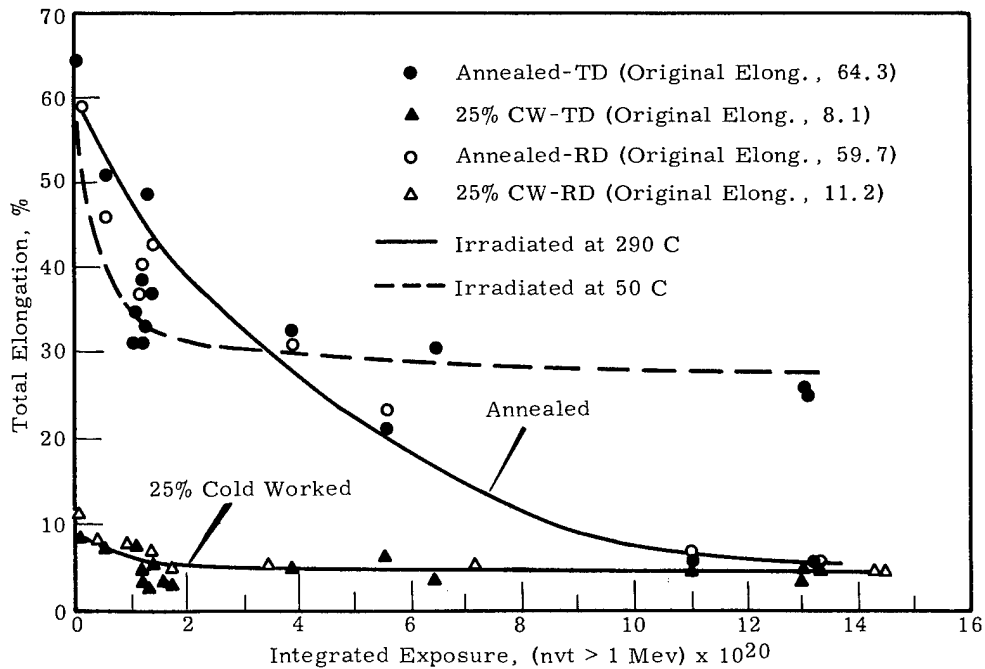


FIGURE 4.28

Effects of Irradiation on Room Temperature Ductility of AISI 348 Stainless Steel

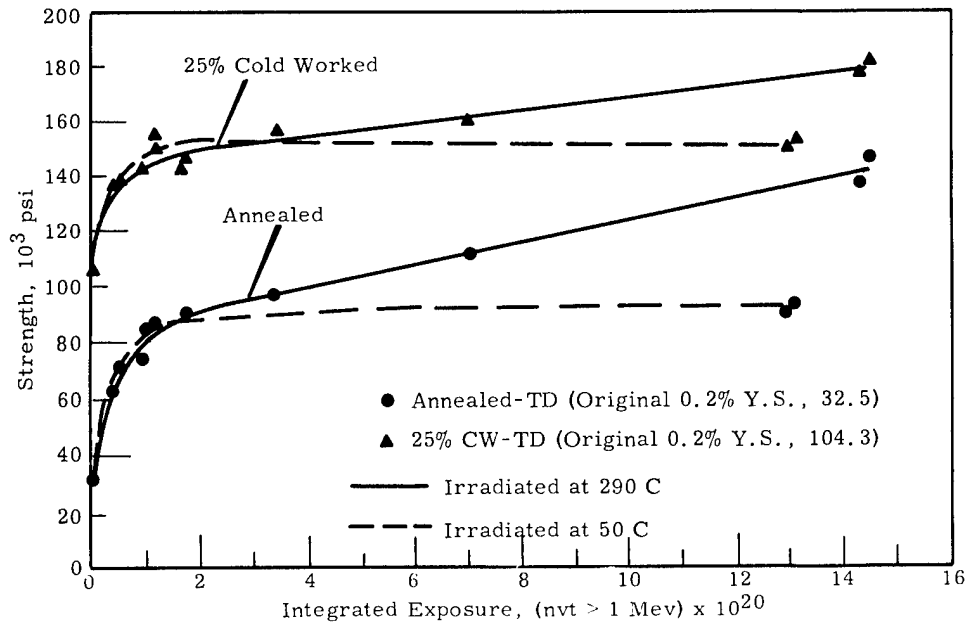


FIGURE 4.29

Effects of Irradiation Room Temperature Yield Strength
of AISI 304 Stainless Steel

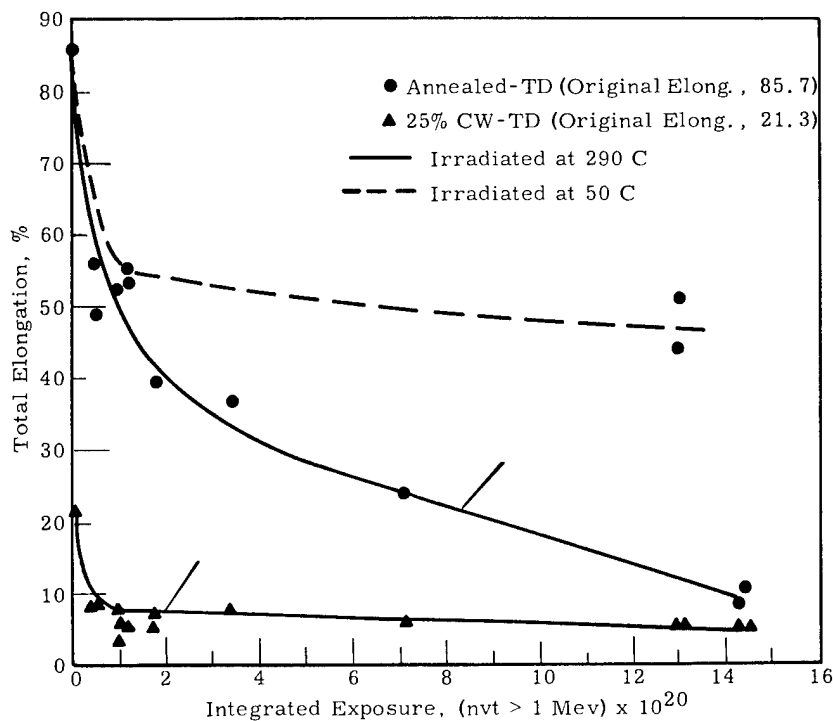


FIGURE 4.30

Effects of Irradiation on Room Temperature Ductility
of AISI 304 Stainless Steel

to the transformation of metastable austenite to a more stable phase. Magnetic measurements as well as X-ray diffraction and electron microscopy studies are being used to determine the identity and the quantity of the new phase or phases.

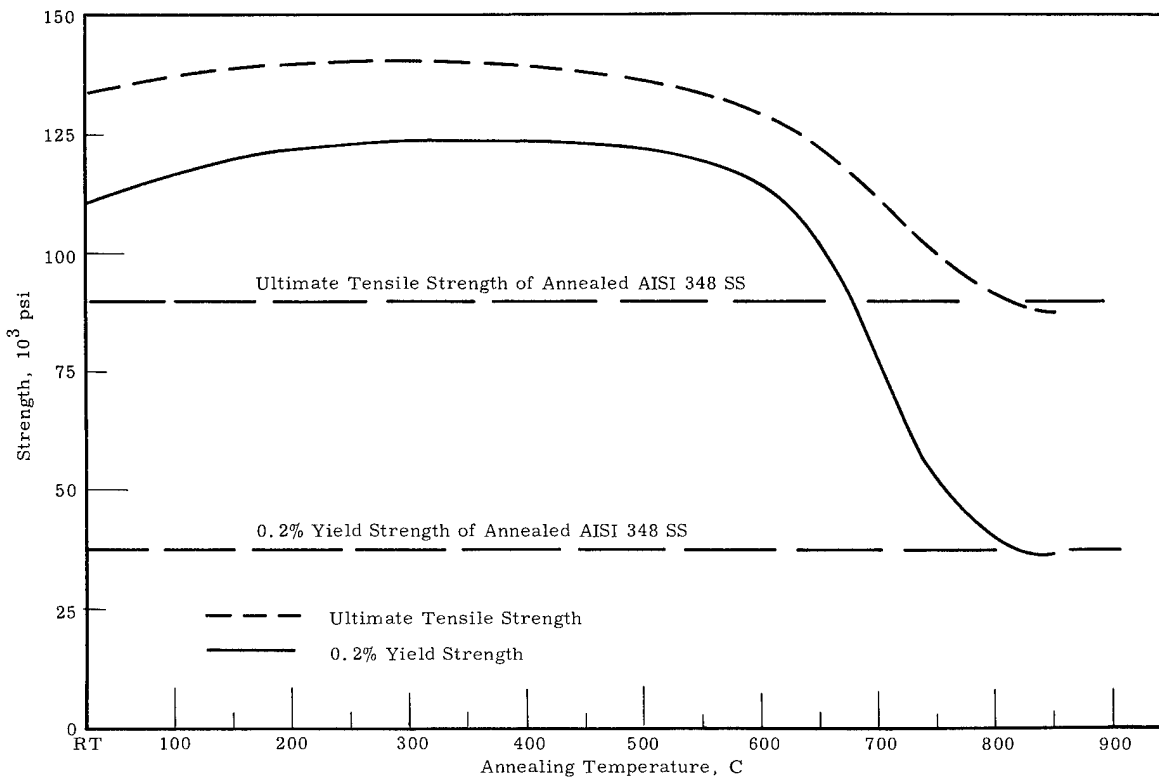


FIGURE 4.31

Mechanical Properties Recovery of AISI 348 Stainless Steel
(All specimens were 25% cold-worked by rolling;
transverse specimens only; 4 hr anneals)

Significant recovery of mechanical properties of the 25% cold-worked material does not occur until an annealing temperature greater than 600 C (1115 F) has been reached. Complete recovery of strength and ductility occurs after a 4 hr anneal at about 800 C (1472 F) or greater.

AISI 348 SS specimens in the annealed and 25% cold-worked condition were irradiated in a gaseous environment at temperatures between 700 C (1295 F) and 775 C (1430 F). Room temperature tests show that

full recovery of 25% cold-worked material has occurred. The strength and ductility at room temperature of both the annealed and 25% cold-worked materials are equal after irradiation at 775 C (1430 F). Yield strength for the irradiated materials was less than that for the annealed AISI 348 SS in the unirradiated condition. A 15% reduction in total elongation was noted for materials irradiated in both the annealed and 25% cold-worked condition, when compared with the tensile properties of the unirradiated material in the annealed condition.

AISI 406 SS specimens in the annealed, 15, and 23% cold-worked conditions, from both the transverse and longitudinal directions, were irradiated and tested under the same conditions. Greater evidence of recovery and recrystallization was evident for all conditions of the material. The strength was less and the ductility was greater for all the irradiated material when compared with the annealed material in the unirradiated condition. Further tests and metallographic studies are being performed on these materials to characterize effects of neutron irradiation at elevated temperatures.

IRRADIATION DAMAGE TO NICKEL-BASE ALLOYS - I. S. Levy and
K. R. Wheeler

The combination of oxidation resistance and high temperature strength places the nickel-base alloys among the most promising materials for nuclear reactor application. These alloys, however, generally suffer embrittlement due to irradiation at high temperature. The effort to modify microstructures of nickel-base alloys to reduce their adverse reaction to subsequent irradiation is continuing.

Solid-Solution Hardened Alloys

Results were previously reported⁽¹⁾ on the room temperature tensile properties of control and irradiated specimens of Hastelloy X-280. Comparison with results obtained at NMPO led to the hypothesis that high temperature irradiation of Hastelloy X-280 in the solution-treated condition caused carbides to precipitate at irradiation damage sites within the matrix leading to increased strength and improved ductility. These carbides would normally precipitate, at the same temperature out-of-reactor, in a continuous grain boundary phase causing reduced ductility. To test this hypothesis, tensile specimens were fabricated from material solution-treated, cold-worked 26%, and then aged. Figure 4.32 compares room temperature tensile properties with those of controls and shows the increased strength and reduced ductility of the cold-worked material. The micrographs in Figure 4.33 show that heavy precipitation occurred along the strain lines of the cold-worked specimens and that grain boundary carbides were reduced. Tests on specimens having lesser amounts of cold work will be performed to determine if ductility can be improved. The effect of irradiation upon these cold-worked materials will be determined.

Precipitation-Hardened Alloys

The study of the effect of preirradiation heat treatments upon in-reactor mechanical properties of Inconel X-750 has continued. Tensile

-
1. Quarterly Progress Report - Metallurgy Research Operation, January, February, March, 1964, edited by J. J. Cadwell, HW-81269. April 15, 1964.

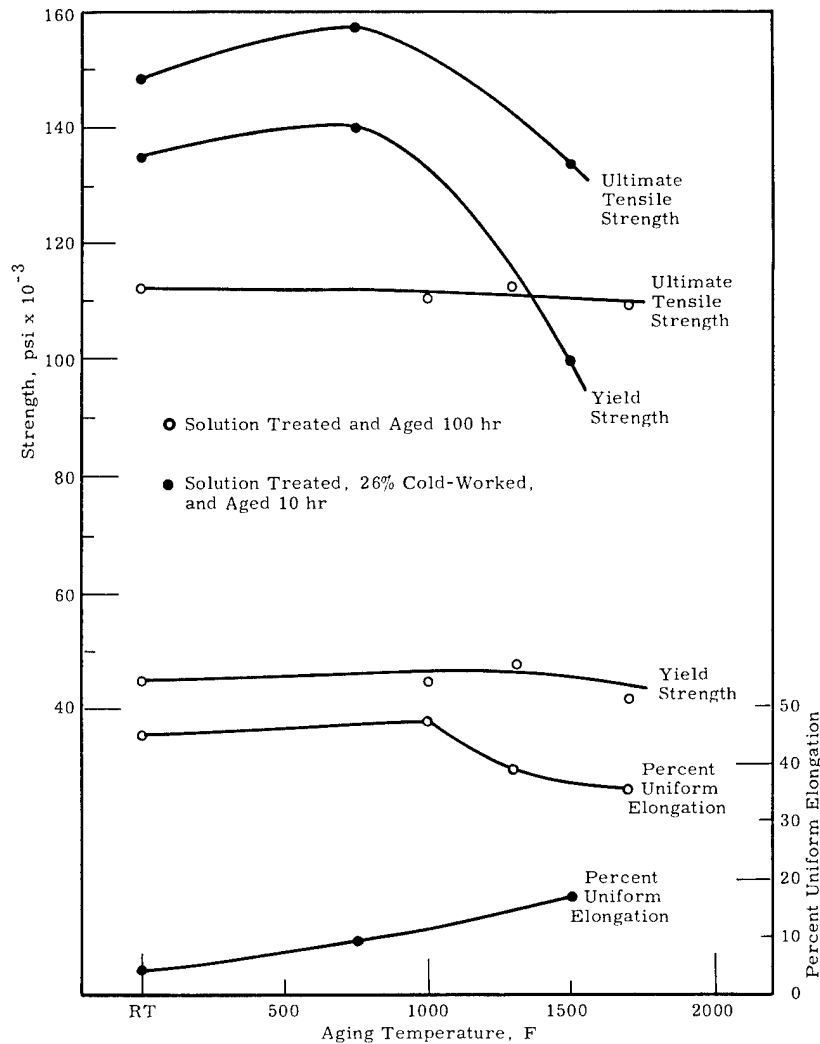
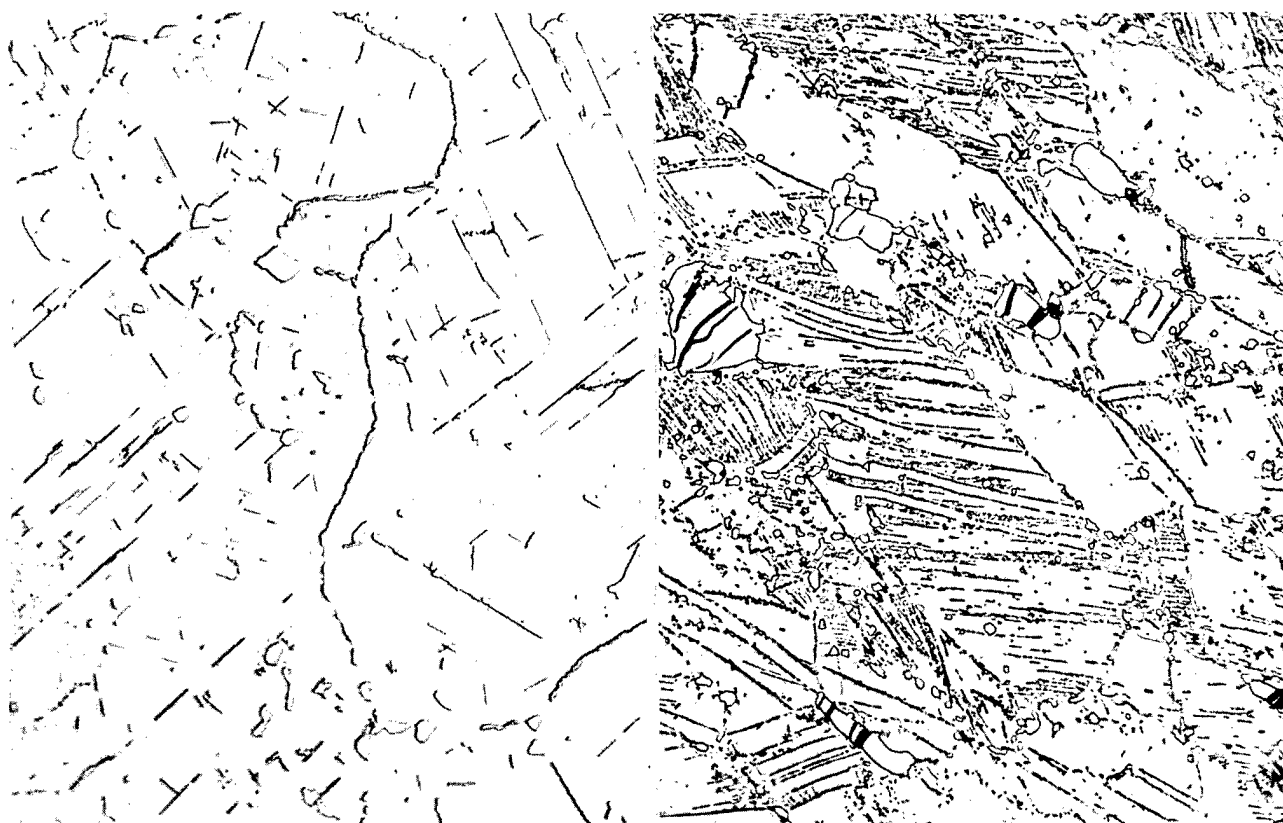


FIGURE 4.32

Hastelloy X-280 Room Temperature Properties After Aging Treatment

tests were performed on control specimens in several experimental heat treatments. Two of these were based on one recommended by the manufacturer⁽¹⁾ for development of a structure most resistant to high temperature creep; they differed in environmental conditions and solutioning treatment. Room temperature tests showed significant differences, particularly in ductility (Table 4.6, Treatments 1 and 5); the elongation

1. Engineering Properties of Inconel X-750, Technical Bulletin T-38. Huntington Alloy Products Division, International Nickel Co., Inc., Huntington, W. Va. 1963.



(a) Aged at 1750 F for 100 hr

(b) Cold-Worked 26%,
Aged at 1500 F for 10 hrFIGURE 4.33

Hastelloy X-280 Initially Solution-Treated
at 2150 F for 1 hr
1000X

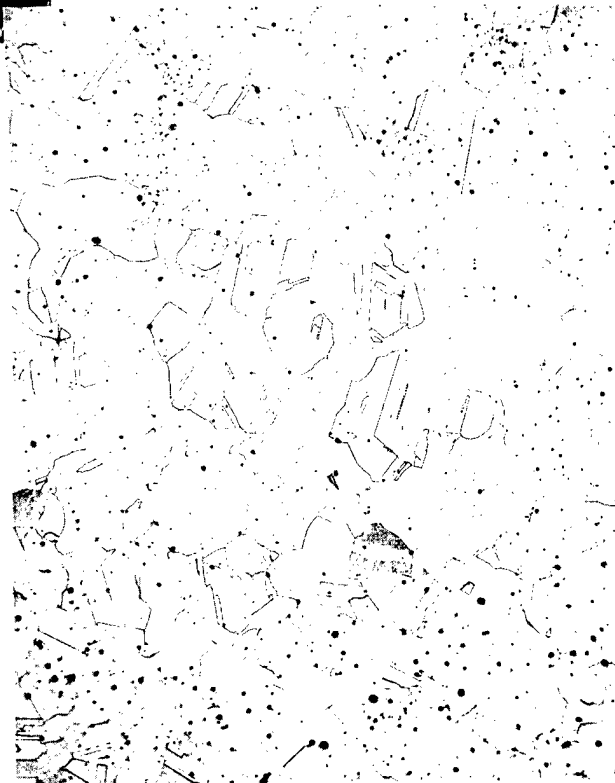
to be expected from the manufacturer's data is about 24%. The reduction found for specimens in Treatment 1 may be due to excessive grain growth during solutioning and/or to increased carbide precipitation at the grain boundaries due to a slower cooling of specimens encapsulated in an ampule. Figure 4.34 shows a significant grain size difference between the two treatments; however, Treatment 1 did give grain size recommended by manufacturer. Figure 4.35 shows that the possibility exists of a significant difference in the amount and blocky character of the carbide phase in the grain boundaries. Experiments will be performed to separate the effects of environment, cooling rate, and solution treatment upon ductility.

Neg. No. K2250; 4L642

AEC-GE RICHLAND, WASH.



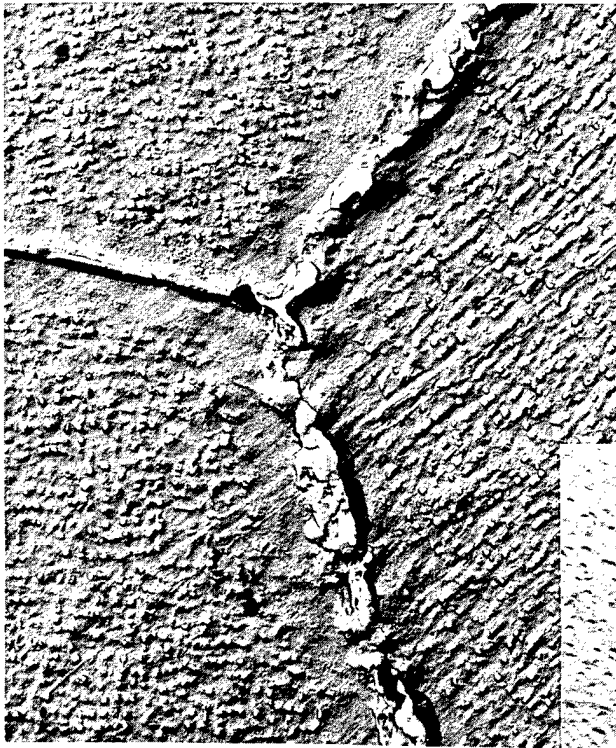
(a) Treatment 1
(in quartz ampule):
1250 F for 2 hr, Air Cool;
1550 F for 24 hr, Air Cool;
1300 F for 20 hr, Air Cool.



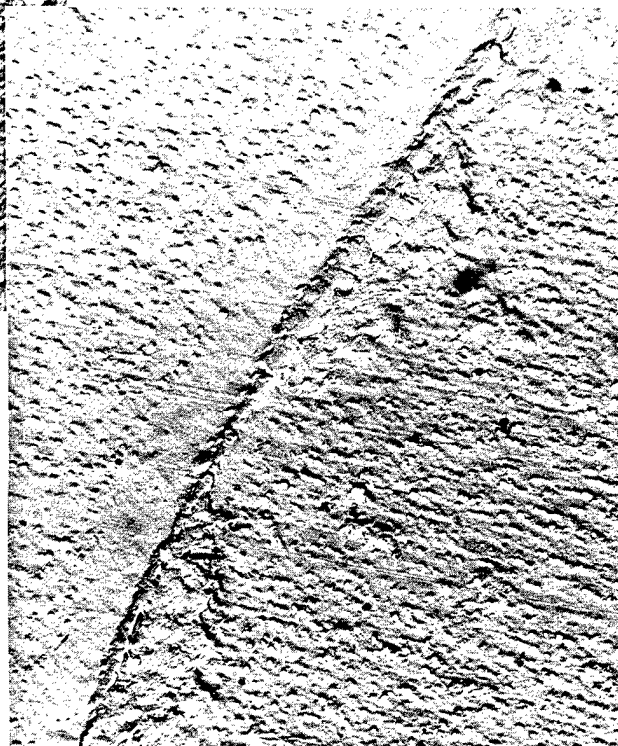
(b) Treatment 5
(in air):
2100 F for 1/2 hr, Rapid Air
Cool; 1550 F for 24 hr, Rapid
Air Cool; 1300 F for 20 hr,
Rapid Air Cool.

FIGURE 4.34

Inconel X-750; Effect of Treatments on Grain Size
Neg. No. 4L9F; 4L874C 50X
AEC-GE RICHLAND, WASH.



(a) Treatment 1
(in quartz ampule)



(b) Treatment 5
(in air, using fan for
rapid air cool)

FIGURE 4.35

Inconel X-750: Effect of Cooling Rate on Grain Boundary Phase
10,000X

Table 4.6 also shows the excellent tensile properties of Treatment 6 which is based on that recommended by the manufacturer for developing good high temperature short-time properties. The effect of irradiation on the mechanical properties of specimens in these treatments will be determined.

Neg. No. 2144B; 2358C
AEC-GE RICHLAND, WASH.

TABLE 4. 6
ROOM TEMPERATURE TENSILE PROPERTIES
OF INCONEL X-750

<u>Heat Treatment*</u>	<u>Specimen No.</u>	<u>Ultimate Tensile Strength, psi</u>	<u>0. 2% Yield Strength, psi</u>	<u>Total Elongation, % in 1 in.</u>	<u>Reduction of Area, %</u>
1	A027	151,000	95,800	12.0	11.5
	A028	148,900	94,700	12.0	14.0
5	A041	163,900	98,000	22.0	23.7
	A042	162,200	95,900	24.0	24.0
6	A043	191,000	138,000	24.0	47.2
	A044	189,100	137,100	24.0	49.4

* 1: Specimen encapsulated in a quartz ampule which was evacuated and backfilled with 1/2 atmosphere of helium: 2150 F (1177 C) for 2 hr, air cooled; 1550 F (843 C) for 24 hr, air cooled; 1300 F (704 C) for 20 hr, air cooled.

5: Specimen in air: cooling was rapid, using a fan: 2100 F (1149 C) for 1/2 hr, rapid air cool; 1550 F (843 C) for 24 hr, rapid air cool; 1300 F (704 C) for 20 hr, rapid air cool.

6: Specimen in air: 1300 F (704 C) for 20 hr, rapid air cool.

DAMAGE MECHANISMS - F. A. Smidt

The objective of the program is to determine the mechanism by which defects produced by neutron bombardment interact with dislocations to modify the plastic deformation characteristics of the metal. The initial studies of this program are directed toward understanding the mechanism of plastic deformation in α iron.

The basic principles of the theory of thermally activated flow have been treated in previous quarterly reports^(1,2) and will not be repeated in this report. In the last report,⁽²⁾ an empirical relation between strain rate and effective stress of the form

$$\dot{\epsilon} = \dot{\epsilon}_0 \tau^{*n} \quad (1)$$

was proposed, where

$\dot{\epsilon}$ = strain rate

$\dot{\epsilon}_0$ = proportionality constant

τ^* = effective stress on a dislocation

n = a constant for tests conducted at the same temperature.

Further consideration of this empirical relation in terms of the theory of thermally activated flow indicates the equation should be of the form

$$\dot{\epsilon} = \dot{\epsilon}_0 \left(\frac{\tau^*}{\tau_{\max}} \right)^n \quad (2)$$

where

τ_{\max} = effective stress at 0 K

and $\dot{\epsilon}_0$ is modified accordingly.

This expression is similar to those proposed for the stress dependence of

-
1. F. A. Smidt, J. J. Holmes, and M. R. Keegan. "Damage Mechanisms," Quarterly Progress Report - Metallurgy Research Operation, October, November, December, 1963, edited by J. J. Cadwell, HW-79766, pp. 4.56-4.76. January 15, 1964.
 2. F. A. Smidt and B. Mastel. "Damage Mechanisms," Quarterly Progress Report - Metallurgy Research Operation, January, February March, 1964, edited by J. J. Cadwell, HW-81269, pp. 4.57-4.64. April 15, 1964.

dislocation velocities^(1, 2, 3) but rather than employing the applied stress as the variable it uses only that stress component capable of altering the dislocation velocity, τ^* .

Testing the validity of this expression by conventional means is impossible because of the inability to measure τ^* directly. However, during the course of strain rate change experiments it was noted that a finite time is required for the strain rate to decrease to a lower rate and this decay was roughly exponential. A series of experiments was then performed in which the specimen was strained at a constant rate to establish the flow stress level after which the tensile machine was stopped and the recorder switched to a time base so as to follow the decrease in stress at constant crosshead separation. The stress dropped rapidly at first but approached a constant value in about 10 to 20 min in room temperature tests. At lower temperatures the decrease was much greater in accordance with the estimates of the magnitude of τ^* .

Essentially what happens is that the elastic energy stored in the machine is converted to work in straining the sample. This extension of the sample at constant cross head separation can be detected by placing an extensometer on the sample. The strain is found to be proportional to the decrease in stress with a slope which is equal to the modulus of the system. At room temperature the drop in stress is only about 0.8 kg/mm² and requires magnification to be measured accurately. An analysis of the experiment based upon Equation (2) yielded a theoretical expression which could be fitted to the experimental data by computer methods.

The analysis of the stress relaxation experiments begins with the equations used by Johnston and Gilman.⁽¹⁾ During the tensile test at constant crosshead speed the macroscopic strain rate is equal to that imposed

-
1. W. G. Johnston and J. J. Gilman. "Dislocation Velocities, Dislocation Densities and Plastic Flow in Lithium Fluoride Crystals," J. Appl. Phys., vol. 30, pp. 129-144. 1959.
 2. G. T. Hahn. "A Model for Yielding with Special Reference to the Yield-Point Phenomena of Iron and Related BCC Metals," Acta. Met., vol. 10, pp. 727-738. 1962.
 3. D. F. Stein and J. R. Low, Jr. "Mobility of Edge Dislocations in Silicon-Iron Crystals," J. Appl. Phys., vol. 31, pp. 362-369. 1960.

by the machine

$$\dot{\epsilon}_M = \dot{\epsilon}_e + \dot{\epsilon}_p \quad (3)$$

where $\dot{\epsilon}_e$ = elastic strain rate

$\dot{\epsilon}_p$ = plastic strain rate.

When the crosshead is stopped $\dot{\epsilon}_M = 0 = \dot{\epsilon}_e + \dot{\epsilon}_p$. We know the elastic strain rate is given by $\dot{\epsilon}_e = \frac{1}{M} \frac{d\tau}{dt}$ where M is the modulus of the system and $\frac{d\tau}{dt}$ is the rate of change of stress. Substituting Equation (2) for $\dot{\epsilon}_p$ gives

$$-\frac{1}{M} \frac{d\tau}{dt} = \dot{\epsilon}_0 \left(\frac{\tau^*}{\tau_{\max}} \right)^n \quad (4)$$

and since $d\tau$ varies only within the range 0 to τ^* the expression can be integrated to give

$$\tau_i^{*(1-n)} - \tau_f^{*(1-n)} = (1-n) \frac{\dot{\epsilon}_0 M}{\tau_{\max}^n} t \quad (5)$$

where τ_i^* and τ_f^* are the initial and final values of τ^* .

In general form this equation is

$$\tau = (\tau_i - \tau_f) \left[1 + (n-1) \tau_i^{*(n-1)} \frac{\dot{\epsilon}_0 M}{\tau_{\max}^n} t \right]^{-\left(\frac{1}{n-1}\right)} + \tau_f \quad (6)$$

or

$$\tau = (\tau_i - \alpha)(1 + \beta t)^{-\gamma} + \alpha \quad (7)$$

This equation was fit to the data by varying the three parameters α , β , and γ until the smallest residual for a least squares fit was determined.

In the one case analyzed to date for a stress relaxation from the flow stress at room temperature and $\dot{\epsilon} = 0.002 \text{ min}^{-1}$, τ^* was found to be 0.84 kg/mm^2 and n was 6.21 with a residual for 140 points of 0.08. An illustration of the experimental curve is shown in Figure 4.36.

The usefulness of the stress relaxation test appears to be quite extensive and only a few applications have been explored to date. Basically it is the same as a creep test at low temperatures in that the creep rate decreases as τ^* approaches 0 (or $\tau_{\text{apl}} \rightarrow \tau_i$). It differs from the

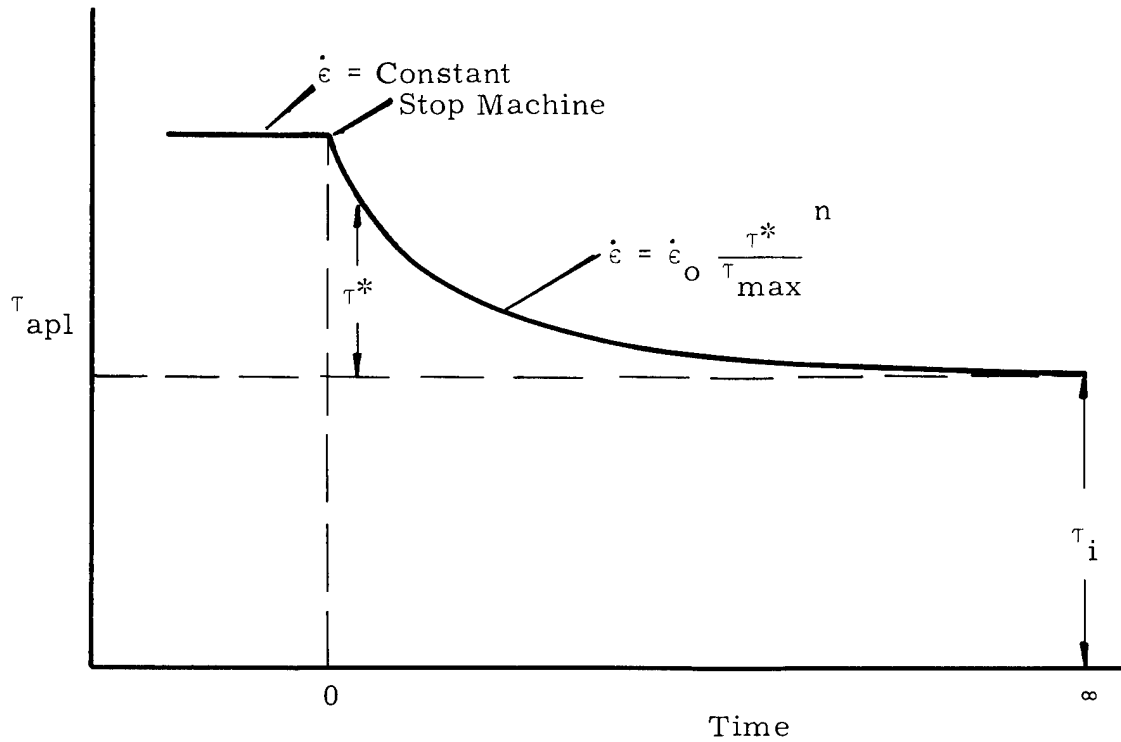


FIGURE 4.36

Schematic Diagram of Relationships Between τ_{apl} , τ^* , τ_i , and Time During Stress Relaxation Experiment

creep test however in that the substructure and dislocation density characteristic of a given strain rate are established in the constant strain rate portion of the test and the initial part of the stress relaxation is meaningful in contrast to the transient behavior of the creep test.

One series of tests where stress relaxation curves were obtained at several strains provided an interesting insight into work hardening in the body-centered cubic metals. The initial tests before about 4 to 5% strain showed a stress drop about twice that of the tests after 5% while the tests at strains greater than 5% showed a constant stress drop up to the ultimate load point. This behavior is believed to be indicative of the formation of a stable substructure, probably the cell wall formation noted by Keh and Weissmann.⁽¹⁾ After the cell structure forms, the work hardening is due to a buildup in the internal stress field τ_i while τ^* remains

1. A. S. Keh and S. Weissmann. "Deformation Substructure in Body-Centered Cubic Metals," Electron Microscopy and Strength of Crystals, edited by G. Thomas and J. Washburn. Interscience Publishers, New York, 1963. pp. 231-299.

constant during the remainder of the deformation. This behavior is similar to that previously observed in strain rate change tests for the change in $\Delta\tau$ with strain although in this latter case it could not be definitely established that the change was entirely due to τ^* .

Another area where the test is useful is the interpretation of the coefficient n , the strain rate sensitivity parameter. This parameter has been measured in the past from the slope of applied stress versus dislocation velocity curves obtained from etch pitting studies^(1, 2) and from strain rate change tests.⁽³⁾ Values of 35 and 66 were obtained by these methods, respectively, for 3.5% silicon-iron. These values, however, appear to be quite sensitive to the purity and perfection of the crystals used, a fact reflected in large values of τ_i hence erroneous results. The basic equation for n is

$$n = \frac{\Delta \ln \dot{\epsilon}}{\Delta \ln \tau_{apl}} = \ln \left(\frac{\dot{\epsilon}_2}{\dot{\epsilon}_1} \right) / \ln \left(\frac{\tau_1 + \Delta\tau + \tau_i}{\tau_1^* + \tau_i} \right). \quad (8)$$

It can be readily seen that the values of n determined from this equation will be meaningless if τ_i is large.

Johnston and Stein⁽⁴⁾ suggested the results should be corrected for changes in dislocation density during the test and extrapolated their n values to zero strain. Michalak⁽⁵⁾ incorporated this suggestion into his strain rate change experiments on single crystal Ferrovac "E" iron and obtained a value of 7.5. Smidt⁽⁶⁾ using τ^* as the stress variable found n

1. W. G. Johnston and J. J. Gilman. "Dislocation Velocities, Dislocation Densities and Plastic Flow in Lithium Fluoride Crystals," J. Appl. Phys., vol. 30, pp. 129-144. 1959.
2. D. F. Stein and J. R. Low, Jr. "Mobility of Edge Dislocations in Silicon-Iron Crystals," J. Appl. Phys., vol. 31, pp. 362-369. 1960.
3. R. W. Guard. "Rate Sensitivity and Dislocation Velocity in Silicon-Iron," Acta Met., vol. 9, pp. 163-165. 1961.
4. W. G. Johnston and D. F. Stein. "Stress Dependence of Dislocation Velocity Inferred from Strain Rate Sensitivity," Acta Met., vol. 11, pp. 317-318. 1963.
5. J. T. Michalak. Unpublished Data. Bain Laboratory for Fundamental Research, U.S. Steel Corp., Monroeville, Pennsylvania. 1963.
6. F. A. Smidt, J. J. Holmes, and M. R. Keegan. "Damage Mechanisms," Quarterly Progress Report - Metallurgy Research Operation, October, November, December, 1963, edited by J. J. Cadwell, HW-79766. pp. 4.56-4.76. January 15, 1964.

values of 3 to 5 on polycrystalline Ferrovac "E" when he solved for the parameter with two simultaneous equations from a double strain rate test. Although correct in principle, neglect of dislocation multiplication effects during strain rate changes made the method inaccurate. It appears that the true equation should be

$$n = \frac{\Delta \ln \dot{\epsilon}}{\Delta \ln \tau^*} + \frac{\Delta \ln \rho}{\Delta \ln \tau^*}. \quad (9)$$

The values of 6.2 obtained in the present experiments by analyzing the stress relaxation curves are believed to be quite accurate but further clarification of the role of dislocation multiplication is required.

If the validity of Equation (2) is accepted, several important equations can be derived which unify the concepts of dislocation dynamics and thermally activated flow, both of which have proven merits. Equating these two approaches we have

$$\ln \frac{\dot{\epsilon}}{\dot{\epsilon}_0} = n \ln \left(\frac{\tau^*}{\tau_{\max}} \right) = -\frac{U}{kT} \quad (10)$$

which gives

$$U = nkT \ln \left(\frac{\tau_{\max}}{\tau^*} \right) \quad (11)$$

Furthermore, since

$$U = \int_{\tau^*}^{\tau_{\max}} V^*(\tau^*) d\tau^*, \text{ it can be shown that}$$

$$V^*(\tau^*) = \frac{nkT}{\tau^*}. \quad (12)$$

The pre-exponential, $\dot{\epsilon}_0$, in Equation (2) has been modified so as to be compatible to both theories and is

$$\dot{\epsilon}_0 = b \left(\frac{A}{\ell} \right) \nu \quad (13)$$

where ρ = dislocation density in (cm/cm³)

b = Burgers vector

A = area swept by a successful thermal fluctuation

ℓ = average distance between points where thermal activation occurs

ν = Debye frequency.

The Equation (10) gives a fairly good description of the observed changes of τ^* with strain rate at a constant temperature. To test its applicability at other temperatures one must know the temperature dependence of τ^* and n . Temperature change experiments over the range 295 to 150 K show $\frac{\Delta\tau}{\Delta T}$ is linear with T and goes to zero at about 295 K for a strain rate of 0.002 min^{-1} . Assuming this linear relation holds at lower temperatures gives the relation

$$\tau^* (T) = 7 \times 10^{-4} T^2 - 0.416 T + \tau_{\max} \quad (14)$$

with

$$\tau_{\max} = 61.7 \text{ kg/mm}^2,$$

a value of τ_{\max} very close to that obtained by Conrad⁽¹⁾ by other methods. A comparison of this equation with the temperature dependence of the yield point is shown in Figure 4.37. Experiments to determine the temperature dependence of n are in progress.

Although the progress made to date on reconciling the theory of thermally activated flow with the experimental facts has been most encouraging there is one area where the results are still confusing. This is the area of dislocation multiplication effects. It is now widely accepted that the drop-in-load yield point is due to an increase in the density of mobile dislocations.^(2,3) Since smaller drop-in-yield points are also obtained in strain rate change tests it must likewise be assumed that there is a change in density during these tests, contrary to the usual assumptions in thermal activation theories. The stress relaxation tests

-
1. H. Conrad. "Yielding and Flow of the BCC Metals at Low Temperatures," The Relation Between the Structure and Mechanical Properties of Metals, National Physical Laboratory Symposium 15, vol. 2, pp. 475-516. Her Majesty's Stationery Office, London, England, 1963.
 2. G. T. Hahn. "A Model for Yielding with Special Reference to the Yield-Point Phenomena of Iron and Related BCC Metals," Acta. Met., vol. 10, pp. 727-738. 1962.
 3. A. H. Cottrell. "Discontinuous Yielding," The Relation Between the Structure and Mechanical Properties of Metals, National Physical Laboratory Symposium 15, vol. 2, pp. 455-473. Her Majesty's Stationery Office, London, England, 1963.

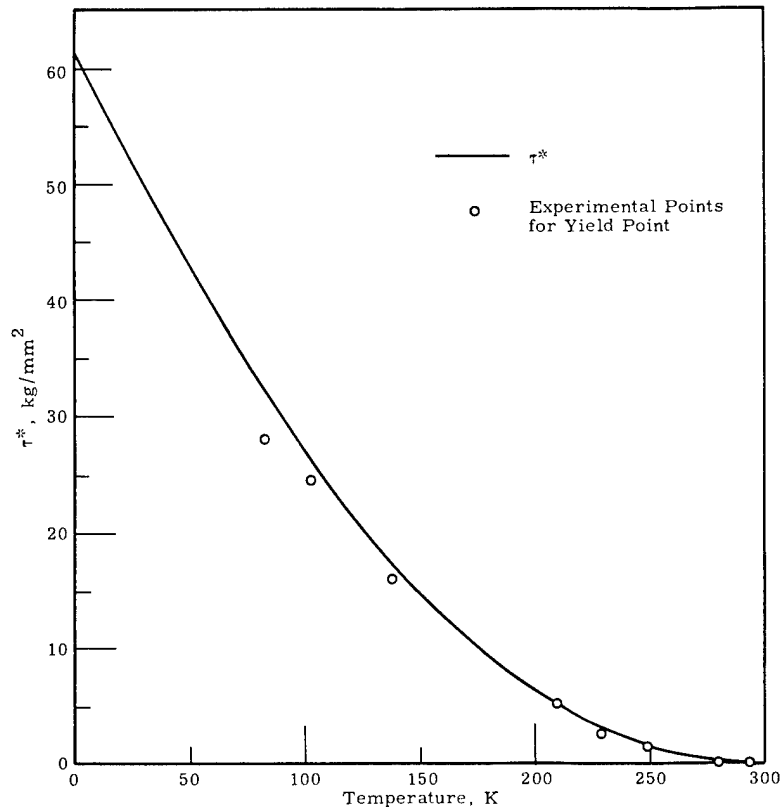


FIGURE 4.37

Temperature Dependence of τ^* for Ferrovac "E" Iron
 (The solid line represents the temperature dependence of τ^* as determined from two temperature change experiments for flow stresses and the points represent data from a temperature dependence of the yield point experiment.)

previously described, show excellent agreement between the data and Equation (2), but when the crosshead is started again at the conclusion of the test a large drop-in-load yield point comparable to the initial yield point but without a Lüders band is observed. This means there must be a change in dislocation density during the stress relaxation test. Perhaps the change in density is obvious only during a rapid change in strain rate and the use of an average value of dislocation density during a stress relaxation test still gives an excellent curve fit because inspection shows the curve fit is just as good in the final portions of the stress relaxation curve as in the initial portions. Several cases have also been observed in

strain rate change tests where there is apparently a reversible change in dislocation density, i. e., a drop-in-load yield point during an increase in strain rate and a decrease in load of about the same magnitude below the extrapolation of the equilibrium flow curve when decreasing the strain rate.

The failure of the analytical method for determining τ^* from two strain rate changes also indicates there must be a change in the density of mobile dislocations. Still more evidence of this is found in the slope of the $\Delta\tau$ versus ϵ curves obtained from strain rate change tests. At room temperature the slope is very nearly zero for Ferrovac "E", but at lower temperatures and for purer materials the slope is negative and can be increased by increasing the dislocation density as in the double strain rate change tests. It would certainly appear that provisions should be made for changes in the density of mobile dislocations if the theory is to give good agreement with the experimental results although the errors involved in neglecting this are probably not too large.

The following exercise shows one method of considering the situation: let us take Equation (10) and assume that ρ in the pre-exponential will change during a strain rate change test but not during a stress relaxation test where the fit has been shown to be good. For the strain rate change test then we have

$$\Delta \ln \dot{\epsilon} = -\frac{\Delta U}{kT} + \Delta \ln \rho = n \ln \frac{\tau_2^*}{\tau_1^*} + \Delta \ln \rho = 2.303 \quad (15)$$

(for $\dot{\epsilon}_2 = 10 \dot{\epsilon}_1$). It is apparent that ΔU and hence $\Delta\tau$ will depend on the change of dislocation density during the test. If one substitutes in values of n and τ_1^* obtained from a stress relaxation experiment from $\dot{\epsilon} = 0.002$ to 0.02 min^{-1} and $\tau_2^* = \tau_1^* + \Delta\tau$ for a strain rate change from $\dot{\epsilon} = 0.002$ to 0.02 min^{-1} , both tests at room temperature, a value of $\frac{\rho_2}{\rho_1} = 1.2$ is obtained.

The applicability of these methods to a treatment of twinning and the ductile-brittle transition temperature is being studied.

CHEMICAL METALLURGYENVIRONMENTAL EFFECTSWater Environment - W. A. Burns

Hydrogen analyses were completed during the report period on all specimens of Zircaloy-2 from Plate 6497 irradiated in Quadrants 73, 74, 85, and 86, and these are summarized in Table 5.1 together with pertinent weight gain and exposure data.

TABLE 5.1IN-REACTOR HYDROGEN PICKUP FOR ZIRCALOY-2

<u>% Cold Work</u>	<u>% Theoretical Corrosion Hydrogen⁽¹⁾</u>			
	<u>Quadrant 73</u>	<u>Quadrant 74</u>	<u>Quadrant 85</u>	<u>Quadrant 86</u>
0	15.2	16.6	27.5	31.0
10	15.1	18.4	30.0	33.2
20	15.5	18.6	48.5	36.8
40	15.9	18.7	47.8	27.4
Quadrant Average				
In-Reactor Weight				
Gain, mg/dm ²	80.1	70.6	49.7	59.9
Exposure Time				
at (T°F), days	38.8(540 F)	38.8(540 F)	22.6(520 F)	41.4(525 F)
Fast Flux				
Intensity	1.0 x 10 ¹⁴ (2)	6.0 x 10 ¹³ (2)	1.03 x 10 ¹⁴	1.04 x 10 ¹⁴

(1) Average of three specimens

(2) "Estimated"

These results are within the range previously reported for 12 other quadrants of irradiated material. Again it is to be noted that hydrogen pickup appears to be independent of either the extent of cold work or fast neutron flux intensity. Upon close visual inspection of the oxide surface on coupons

of Quadrants 85 and 86 it was noted that a slight brownish coloration was present as opposed to the dark grey or blue black appearance of all other coupons viewed to date.

Metallographic measurements of oxide thickness on a number of tensile test specimens during the quarter were found to fall in and beyond the high part of the range previously reported for bend test specimens. Fractional pickup of theoretical corrosion hydrogen was found to be within the range previously reported for bend test specimens. Results are shown in Figure 5.1, black points, and in Table 5.2 with hydrogen gain data and pertinent exposure information. It is to be noted that these are results for single specimens and the limitations of the method yield an accuracy of no better than $\pm 20\%$.

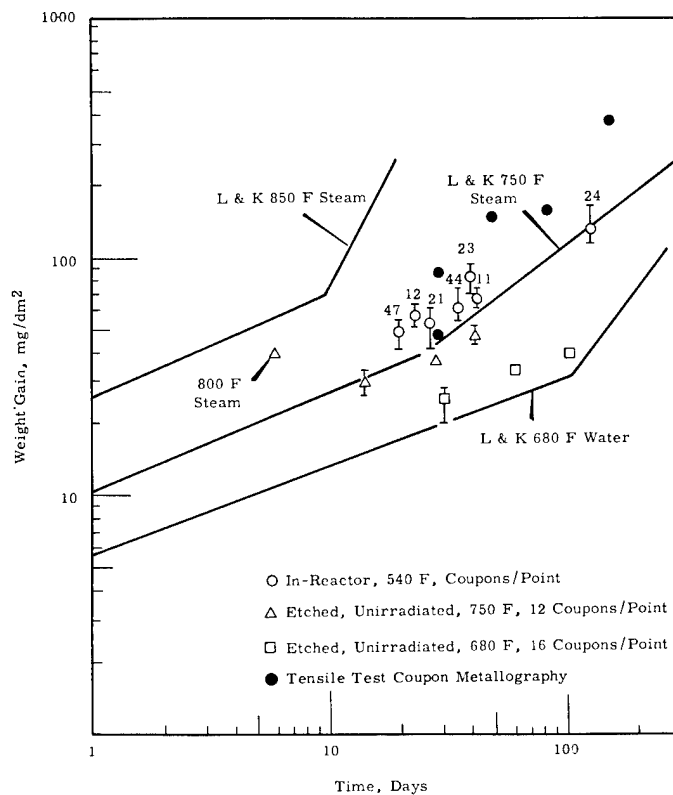


FIGURE 5.1
Corrosion Characteristics of Zircaloy-2

TABLE 5.2
CALCULATED WEIGHT GAIN AND HYDROGEN PICKUP RESULTS
FROM METALLOGRAPHIC EXAMINATION
OF SELECTED ZIRCALOY-2 TENSILE TEST SPECIMENS
FROM PLATE 6513 EXPOSED IN THE ETR G-7 LOOP

Quadrant	Specimen Number	Exposure Time at 540 F, Days	Fast Neutron Flux, nv	Calculated ⁽¹⁾ Total Weight Gain, mg/dm ²	Total Hydrogen, ppm	% Theoretical ⁽²⁾ Hydrogen
4	3	23.7	2.1×10^{13}	48	27	15
8	3	23.7	5.5×10^{13}	47	30	18
16	4	23.7	1.05×10^{14}	86	41	15
26	2	42.9	6.3×10^{13}	148	60	15
10	2	77.1	4.7×10^{13}	154	100	25
20	2	144.0	8.7×10^{13}	370	176	20

(1) Includes a pre-exposure autoclave weight gain of about 20 mg/dm².

(2) Based on total weight gain. Original plate hydrogen: 11 ppm.

Metallographic examination of specimens cut from a thick walled (0.475 in.) basket tube used in the M-3 Loop at the ETR showed oxide thickness corresponding to a weight gain of about 29 mg/dm² following 113 days exposure to a maximum fast neutron flux of 1.5×10^{13} in 500 F water and no metallographically visible hydride. This corresponds to a rate of oxidation not more than two to three times greater than expected for out-of-reactor exposure. Similar examinations of samples of Zircaloy-2 from a process tube, a fuel element jacket and a fuel element support following exposure in the Hanford KER test facility have shown evidence ranging from none to several-fold increase in corrosion rates under KER exposure conditions.

Environmental Effects - Low Oxygen Coolant Program - W. A. Burns

The unexpectedly high rates of oxidation consistently found for all Zircaloy-2 material exposed to the in-core environment of the G-7 Loop and the lack of general agreement among investigators on the effect of fast neutrons on the corrosion kinetics are a matter of record. Known differences in environmental conditions at various test facilities when conflicting data on in-reactor Zircaloy corrosion data is generated, including coolant composition, indicate a need for a special test to achieve a greater degree of similarity of environment.

With a view to obtaining a better match of coolant and flux parameters, a two-cycle special test will be conducted in the G-7 Loop of the ETR beginning with Cycle 65 in July of this year. The oxygen content of loop water will be reduced to levels more comparable with power reactor conditions and specimens will be exposed in a region of greatly reduced fast neutron flux.

Sufficient hydrogen will be injected into the loop to maintain 15 to 25 cm³/kg of coolant in an attempt to maintain oxygen well below 0.1 ppm (current oxygen concentration about 0.8 ppm). A special specimen hanger will be used to provide a test position in the region of highly perturbed neutron flux at the upper fringe of the active zone in addition to the seven normal positions. It is anticipated that the flux will approach levels of two orders of magnitude below the lowest previously attainable fast flux at the "A" level. For this reason, full-specimen length flux wires will be used in company with metallographic techniques to explore the flux dependence of oxidation kinetics.

A large number of stainless steel and Zircaloy-2 tensile, notch tensile and bend specimens will be exposed at all test positions. In addition, Zircaloy-2 tubing for subsequent burst testing as well as specimens of Zircaloy-4, Nickel-Free Zircaloy-2 (Zr-3Nb-1Sn) and heavily cold-worked Zircaloy-2 will be irradiated for corrosion and bend test studies. The results of this special test will be reported in subsequent issues of this report series.

Corrosion of ATR Loop Structural Materials - R. E. Westerman

Initial studies of the corrosion behavior of Haynes Alloy 25 and Hastelloy X-280 in support of the ATR program were performed at 2192 F (1200 C). Since that time, the maximum structural material operating temperature has been set at 2050 F (1120 C) so that the initial data yielded corrosion and evaporation rates which are not directly applicable to predicted ATR operating conditions.

The oxidation rates of Haynes Alloy 25 at 2192 and 2050 F in 100 torr oxygen are compared in Figure 5.2. The oxidation is assumed uniform, and the subscale reactions ignored for the purpose of the comparison. Dropping the test temperature from 2192 to 2050 F results in a 13-fold decrease in penetration at 500 minutes. When the 2050 F sample was cooled, extensive spalling of the apparently protective oxide film occurred.

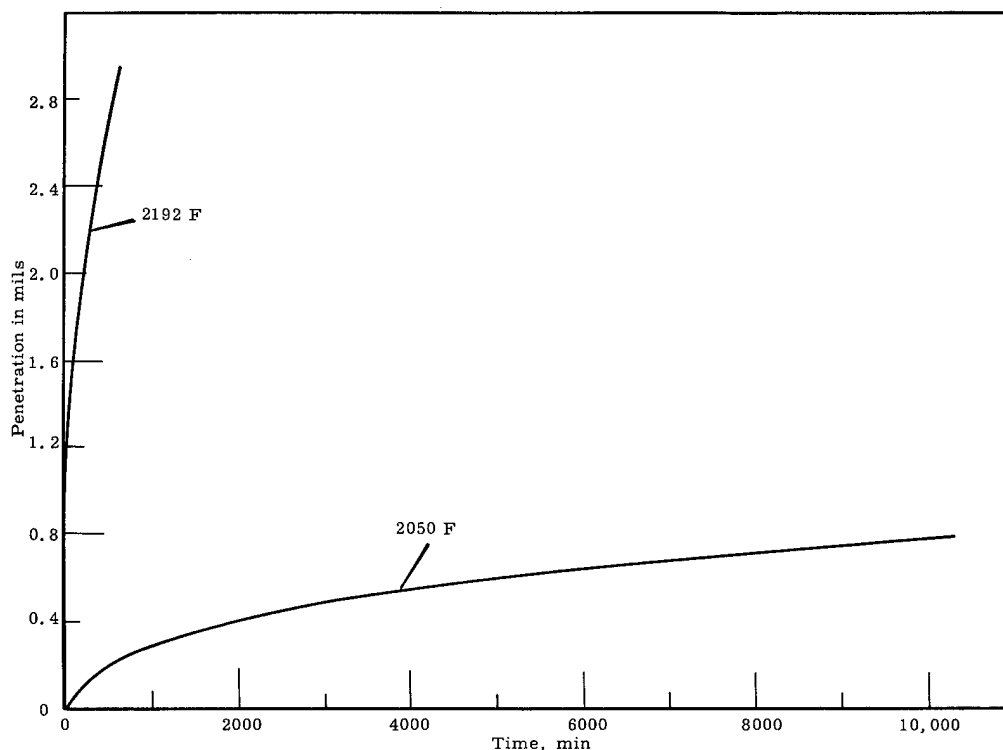


FIGURE 5.2

Penetration of Haynes Alloy 25 in 100 Torr Oxygen
at 2192 F (1200 C) and 2050 F (1120 C)

The evaporation rates at the two temperatures are compared in Figure 5.3. Dropping the test temperature from 2192 to 2050 F in a vacuum of $\sim 1 \times 10^{-4}$ torr reduces the evaporation rate by about a factor of 3. Again, the evaporative attack was assumed absolutely uniform and subsurface effects ignored for the purposes of comparison.

Future tests will include studying the effect of oxygen pressure on the oxidation rate of Haynes Alloy 25 at the lower test temperature (2050 F).

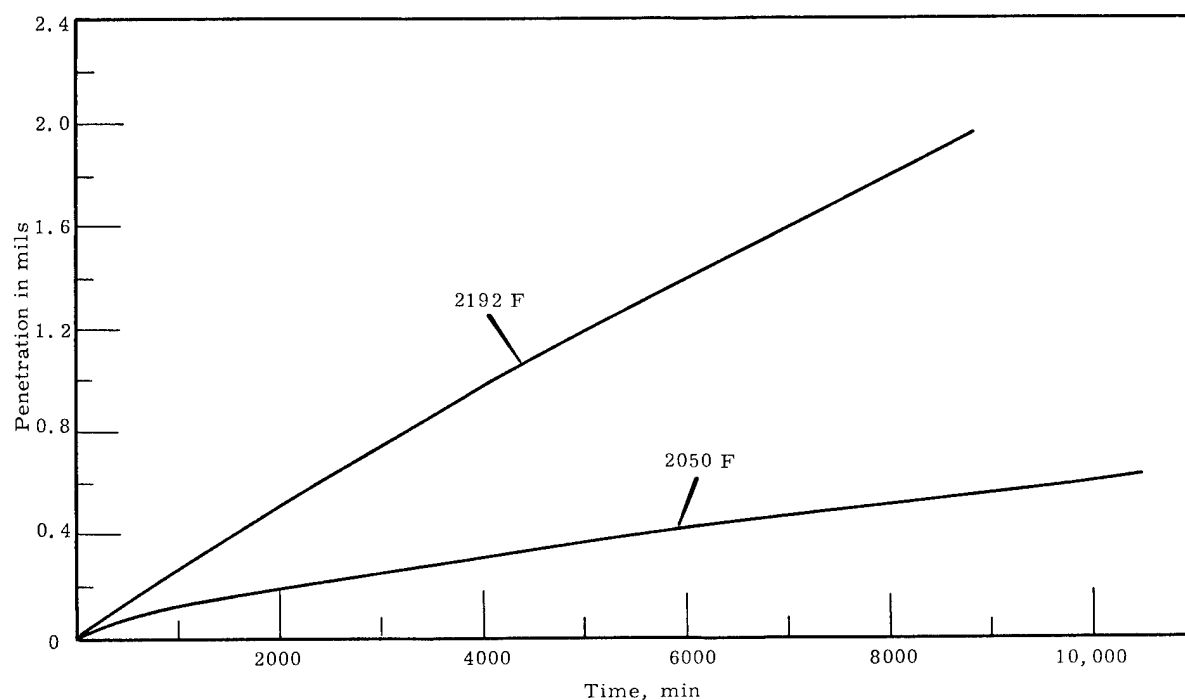


FIGURE 5.3

Penetration of Haynes Alloy 25 in Vacuum ($\sim 1 \times 10^{-4}$ torr)
at 2192 F (1200 C) and 2050 F (1120 C)

Gas-Solid Reactions at High Temperatures - W. J. Guay

Specimens of both fully annealed and stress relieved molybdenum sheet made from arc cast material and of both fully annealed and as-received TZM alloy (Mo-0.08 wt% Zr-0.5 wt% Ti) sheet were oxidized at 5×10^{-3} and 5×10^{-4} mm mercury pressure of air at 1000 C (1832 F). Results are shown below in Table 5.3.

TABLE 5.3

OXIDATION OF MOLYBDENUM AND ITS ALLOYS AT 1000 C

Experiment Number	Specimen Number	Composition	Time (hr)	Pressure Air mm Mercury	Wt Change g/cm ²	Metal Loss g/cm ²
1	1	Mo, stress relieved	16.8	5×10^{-3}	0.0015 loss	
	2	Mo, fully annealed	16.8	5×10^{-3}	0.0014 loss	
	1	Mo, stress relieved	38.1	5×10^{-3}	0.0045 loss	
	2	Mo, fully annealed	38.1	5×10^{-3}	0.0041 loss	
	1	Mo, stress relieved	104.2	5×10^{-3}	0.0153 loss	
	2	Mo, fully annealed	104.2	5×10^{-3}	0.0152 loss	
2	1	Mo, stress relieved	147.5	5×10^{-4}	0.0001 gain	
	2	Mo, fully annealed	147.5	5×10^{-4}	0.0003 loss	
	3	TZM, annealed	147.5	5×10^{-4}	0.0004 gain	
	4	TZM, as-received	147.5	5×10^{-4}	0.0011 gain	
	1	Mo, stress relieved	266.2	5×10^{-4}	0.0000 loss	0.0015
	2	Mo, fully annealed	266.2	5×10^{-4}	0.0008 loss	0.0032
	3	TZM, annealed	266.2	5×10^{-4}	0.0007 gain	0.0019
	4	TZM, as-received	266.2	5×10^{-4}	0.0016 gain	- *

* This sample showed a weight gain of 0.0000 g/cm² after descaling, indicating internal oxidation. All of the samples reported in Column 7 are being examined metallographically to determine the extent, if any, of internal oxidation.

The results in Column 6 are the weight change of the samples as removed from the furnace at the end of the experiment. In Column 7, weight changes are calculated after the samples were descaled.⁽¹⁾ In the absence of internal oxidation weight loss on descaling is a reliable measure of the amount of metal attack.

-
1. H. P. Maffei. Descaling of Various Iron and Nickel Base Alloys, HW-79048. September, 1963.

In all of the work covered by this report molybdenum is believed to be oxidized in two steps with nonvolatile MoO_2 being formed first at the metal-gas interface. As the MoO_2 layer grows, volatile MoO_3 forms at the MoO_2 -gas interface. With these two oxidation processes taking place simultaneously the samples will gain or lose weight depending upon the relative rates of the two oxidation processes.

In Experiment 1, which took place at the higher pressure of air (5×10^{-3} mm mercury), it is believed that most of the MoO_2 was oxidized to MoO_3 resulting in weight losses. The surfaces of the specimens were smooth and only slightly discolored indicating that little MoO_2 was left at the surface. In Experiment 2, at a lower pressure of air (5×10^{-4} mm mercury), the metal loss as determined by stripping of the oxidized samples is shown in Column 7. Specimens 1, 2, and 3 show much lower rates of attack than were indicated for the higher pressure air (Column 6). The weight change behavior of Sample 4 suggests internal oxidation, but conclusions will depend on metallography.

In Experiment 2 there was a noticeable difference in the results between molybdenum and TZM. The TZM surface was discolored but smooth. Molybdenum spalled after the 147.5 hr exposure. The titanium and zirconium in the TZM may have been preferentially oxidized and/or nitrided internally. Because of the two stage oxidation process (metal to nonvolatile MoO_2 to volatile MoO_3) comparisons of the weight changes, Table 5.3 Column 6 at 147.5 hr, are not an accurate quantitative measure of the respective rate of attack. Descaling of these samples will be required for meaningful comparisons. Upon descaling the results of Experiment 2 indicate much smaller rates of attack at the lower pressure. The descaling technique⁽¹⁾ used here has been used successfully on nickel-base alloys and the samples are being investigated further by metallography in order to calculate penetration rates more accurately.

1. H. P. Maffei. Descaling of Various Iron and Nickel Base Alloys, HW-79048. September, 1963.

Gas Chromatograph - D. W. Shannon

A gas chromatograph is being developed to analyze trace impurities in helium. The chromatograph uses a beta ionization detector which has very high sensitivity when operated with ultrapure helium as a carrier gas. It has been found, however, that this extreme sensitivity can be lost if the carrier gas, piping, valves and columns are not kept completely free of contamination. A 4 ft long, 1/8 in. diameter stainless steel column packed with Linde 13X molecular sieve was substituted for the 5A column with significant improvement in the sharpness of peaks. This allowed an increase in sample size and carrier flow rate which further improved sensitivity.

Calibrations of the chromatograph have started but have been hampered by inadequate standards in the region below 10 ppm. Three standards were made in the new Chemical Metallurgy Operation mixing facility. The procedure was to evacuate a stainless steel gas cylinder to below 1 micron. Gases were then added to the cylinder using a CVC 100A McLeod gage to measure the pressure. After all contaminant gases were added, 491 psi Grade A Helium was introduced. (This helium was later analyzed to subtract a blank, if any, from the peak heights.) The compositions are shown in Table 5.4.

TABLE 5.4

<u>Component</u>	<u>CALIBRATION STANDARDS</u>					
	<u>Mixture 1</u>		<u>Mixture 2</u>		<u>Mixture 3</u>	
	<u>mmHg</u>	<u>ppm</u>	<u>mmHg</u>	<u>ppm</u>	<u>mmHg</u>	<u>ppm</u>
H ₂	0.229	8.5	1.96	72.7	27.9	805
Air	0.233		2.14		21.7	-
80% N ₂	-	6.9	-	63.4	-	828
19% O ₂	-	1.7	-	15.2	-	197
CH ₄	0.196	7.3	0.89	33.0	-	-
CO	0.250	9.3	2.63	97.6	18.0	668
CO ₂	0.240	8.9	1.64	60.8	21.0	779

He 500 psi* x 53.91 = 26,955 mm in all mixtures

* 491 psi actually added to correct for nonideal behavior of helium

These three standards have been run on the chromatograph with the peak height results given in Figure 5.4. A typical chromatograph of Standard 1 is given in Figure 5.5. Extrapolation to the 2X noise level line indicates better than a 1 ppm lower detection limit for all components. This is subject to further verification after 1 ppm standards can be made when the Metallurgy Research ultrapure helium purifier is available.

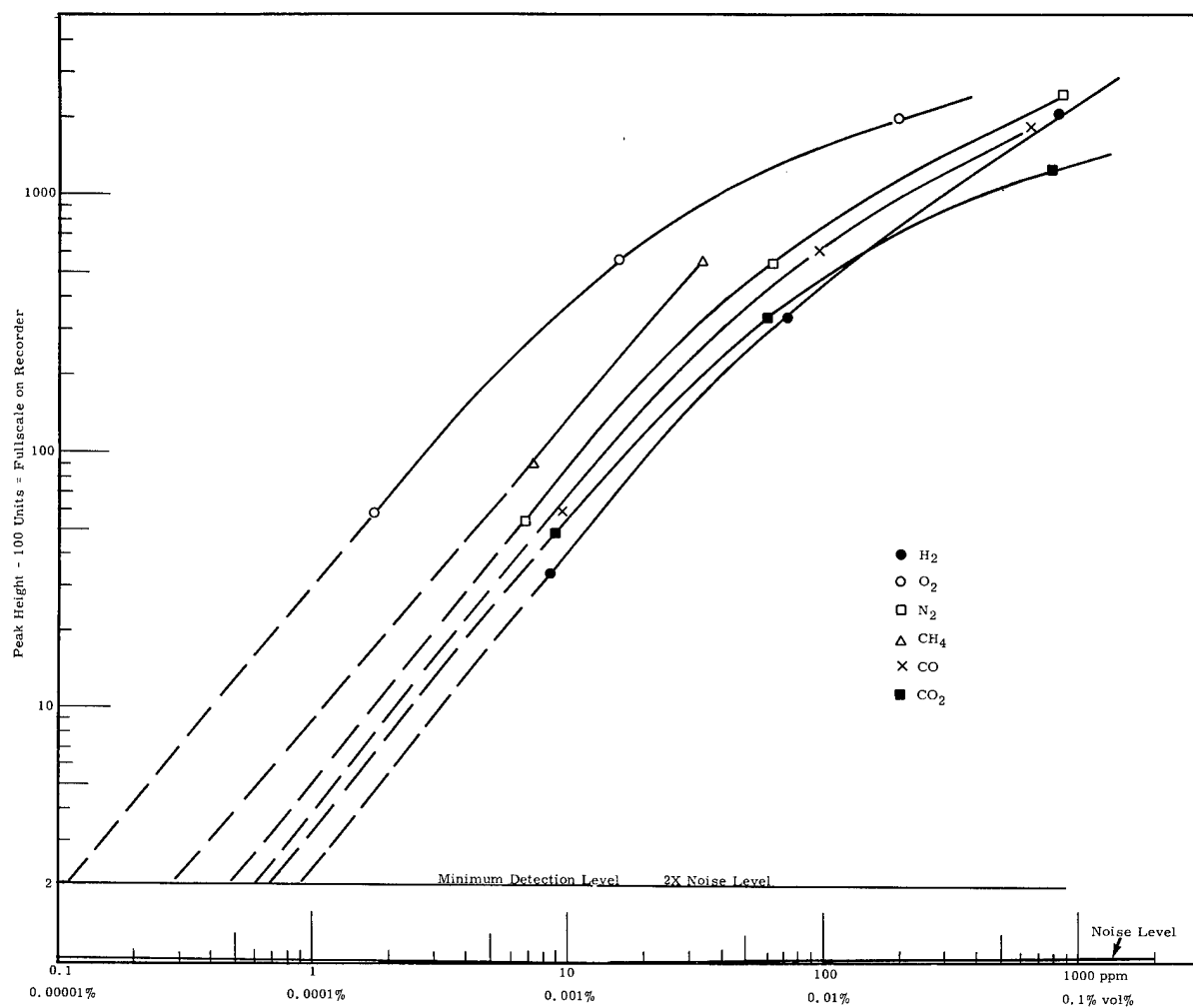


FIGURE 5.4
Peak Height Results

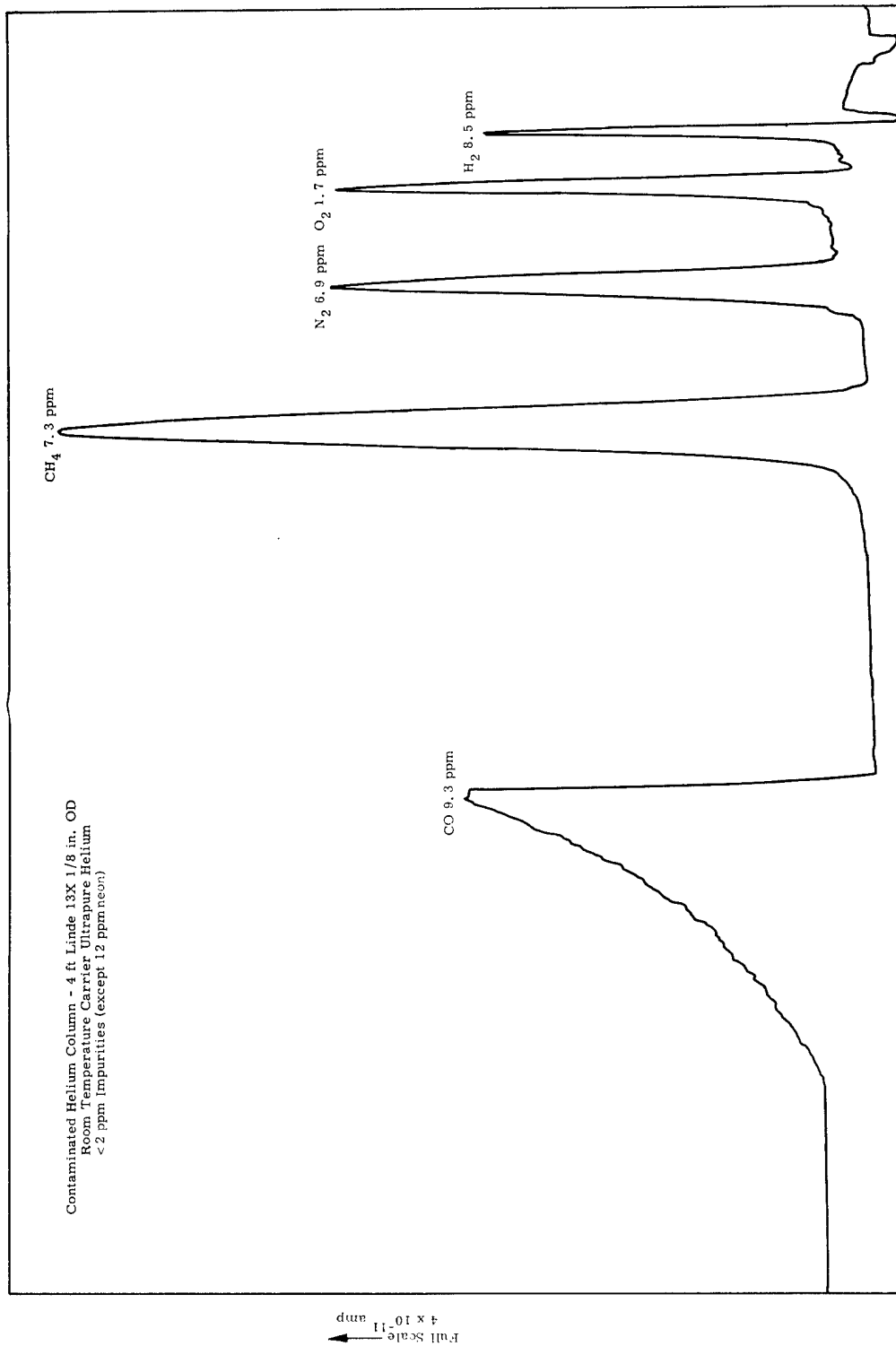


FIGURE 5.5
Typical Chromatograph of Standard 1

Irradiation Effects on the Corrosion of PRTR Zircaloy-2 Process Tubes

H. P. Maffei

Metallographic measures of oxide thickness on two sections of a discharged PRTR Zircaloy-2 process tube have been completed. The process tube had been in service from startup of PRTR until April 4, 1963. During this period of time, the tube was operating at a temperature of 400 F (204 C) or more for approximately 200 days. The two sections being examined have seen different flux densities of approximately 3.86×10^{12} nv (>1 Mev) and 2.02×10^{13} nv (>1 Mev), respectively.

Oxide thickness measurements taken from the metallographic cross sections are (Figure 5.6) equivalent to approximate weight gains of 41* mg/dm² for both samples.

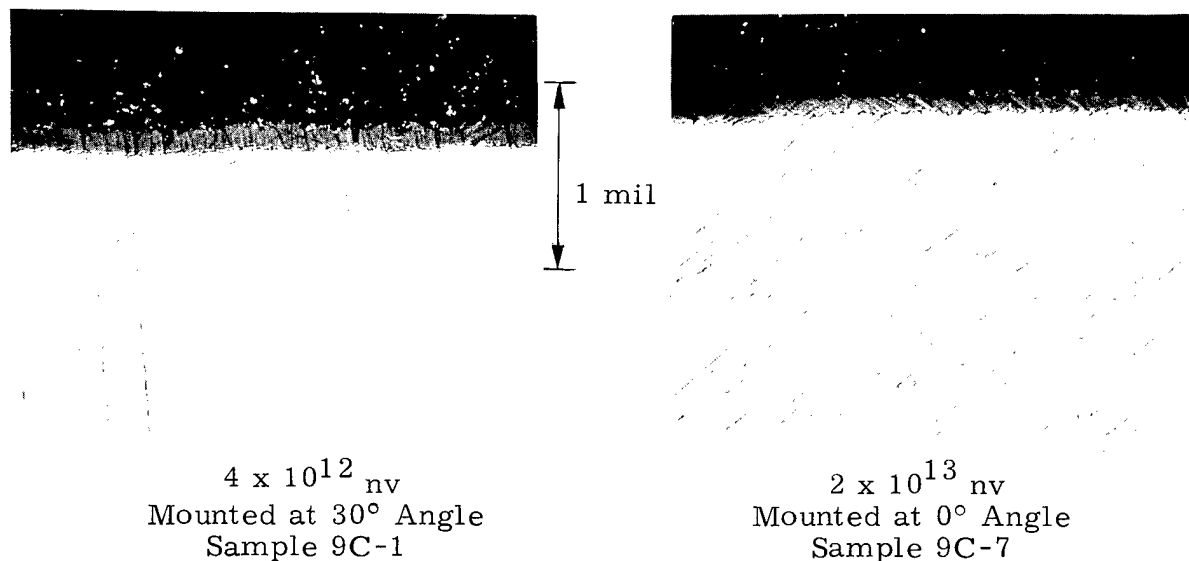


FIGURE 5.6

Cross Sections of PRTR Process Tube
at Different Neutron Flux Levels Showing Oxide Thickness
1000X

Assuming an original autoclave film on the process tube equivalent to a weight gain of 16 mg/dm², the net in-reactor weight gain would be approximately 25 mg/dm². This net weight gain is a factor of 5 higher than would normally be expected for Zircaloy-2 exposed out-of-reactor to

* Best estimates of the precision of the metallographic determination of oxide thickness on zirconium alloys are $\pm 20\%$ (See "Water Environment" page 5.1.)

the same temperature and water conditions for the same length of time. Metallography of the unirradiated section of the process tube indicates an oxide thickness equivalent to a weight gain of 21 mg/dm^2 of which 5 mg/dm^2 was probably incurred in-reactor. Available data is insufficient to conclusively establish an irradiation effect on Zircaloy corrosion in PRTR. Additional irradiated PRTR pressure tubes will be examined metallographically during the next reporting period.

An estimation of the total amount of corrosion product hydrogen which could have been absorbed by the process tube during reactor exposure has been calculated. Assuming that the process tube corroded the same amount on both the ID and OD surfaces, and that 30% of the corrosion product hydrogen was absorbed, the hydrogen content would have increased by 5 ppm. This appears to be verified by hot vacuum extraction analyses for the PRTR tube sections. Total hydrogen contents range from 30 ppm for the out-of-flux samples to 34 and 38 ppm for the in-flux samples. Metallographic cross sections showing hydride distribution are presented in Figure 5.7.

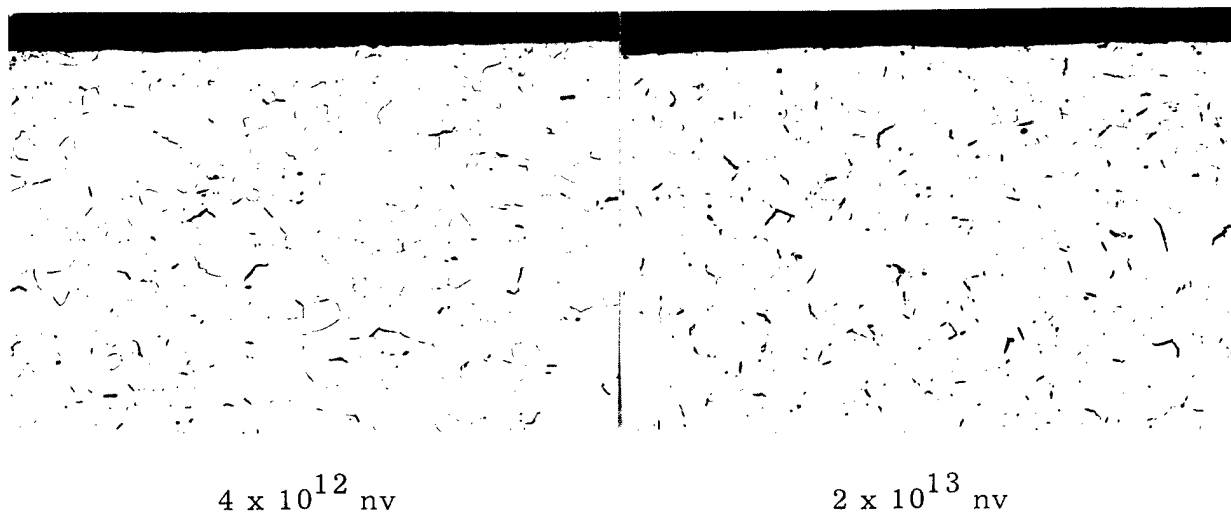


FIGURE 5.7

Cross Sections of PRTR Process Tube
at Different Neutron Flux Levels Showing Hydride Distribution
250X

Effect of Thermal Cycling on the Oxidation of Zircaloy-2 - D. W. Shannon

The cause of the rate transitions observed in the weight gain versus time plots of Zircaloy-2 have been a subject of considerable controversy and interest for many years. A publication of Griggs, Maffei and Shannon⁽¹⁾ pointed out multiple rate transitions and suggested that the inflections were caused by periodic mechanical breakdown of the film. A number of workers have subsequently confirmed the presence of multiple rate transitions. During March 1964 Libby-Cockcroft exchange meetings the British indicated they had seen multiple transitions in high pressure autoclaves (presumably thermally cycled) but not at low pressure in thermal balance experiments (isothermal).

A Hanford thermal balance experiment was started to corrode Zircaloy-2 under both isothermal and thermal cycled conditions. A Zircaloy-2 coupon (6.4 x 3.2 x 0.076 cm) was bright etched in HNO_3 -HF, dried, and suspended in an Ainsworth vacuum recording balance with a water trap attached. The water in the trap was frozen, the system evacuated, back filled with pure helium, and then the water was thawed to give a partial pressure of H_2O of about 23 mm. The sample was then heated to 425 C (797 F) and held isothermally for 85 days. No rate transition at all was observed in the 35 to 40 mg/dm^2 region where transition normally occurs. At about 60 to 70 mg/dm^2 the rate began to accelerate. No evidence of multiple transitions was observed.

A second experiment is now underway which is identical except the sample was periodically cooled to room temperature over night and reheated to 425 C (797 F) the next morning. Comparison of these two runs in Figure 5.8 shows the first thermal cycle at 30 mg/dm^2 had little effect on the rate, but thermal cycling at 35 and 45 mg/dm^2 both initiated an increase in rate with decreasing rate over the next 7 days following the thermal cycle. These results confirm the idea that rapid cracking and release of the compressive stresses in the oxide film is the cause of rate transitions observed, since the thermal shock treatment would accelerate cracking provided the stresses were already present.

1. B. Griggs, H. P. Maffei, and D. W. Shannon. Multiple Rate Transitions in the Aqueous Corrosion of Zircaloy, HW-67818 REV. December, 1960.

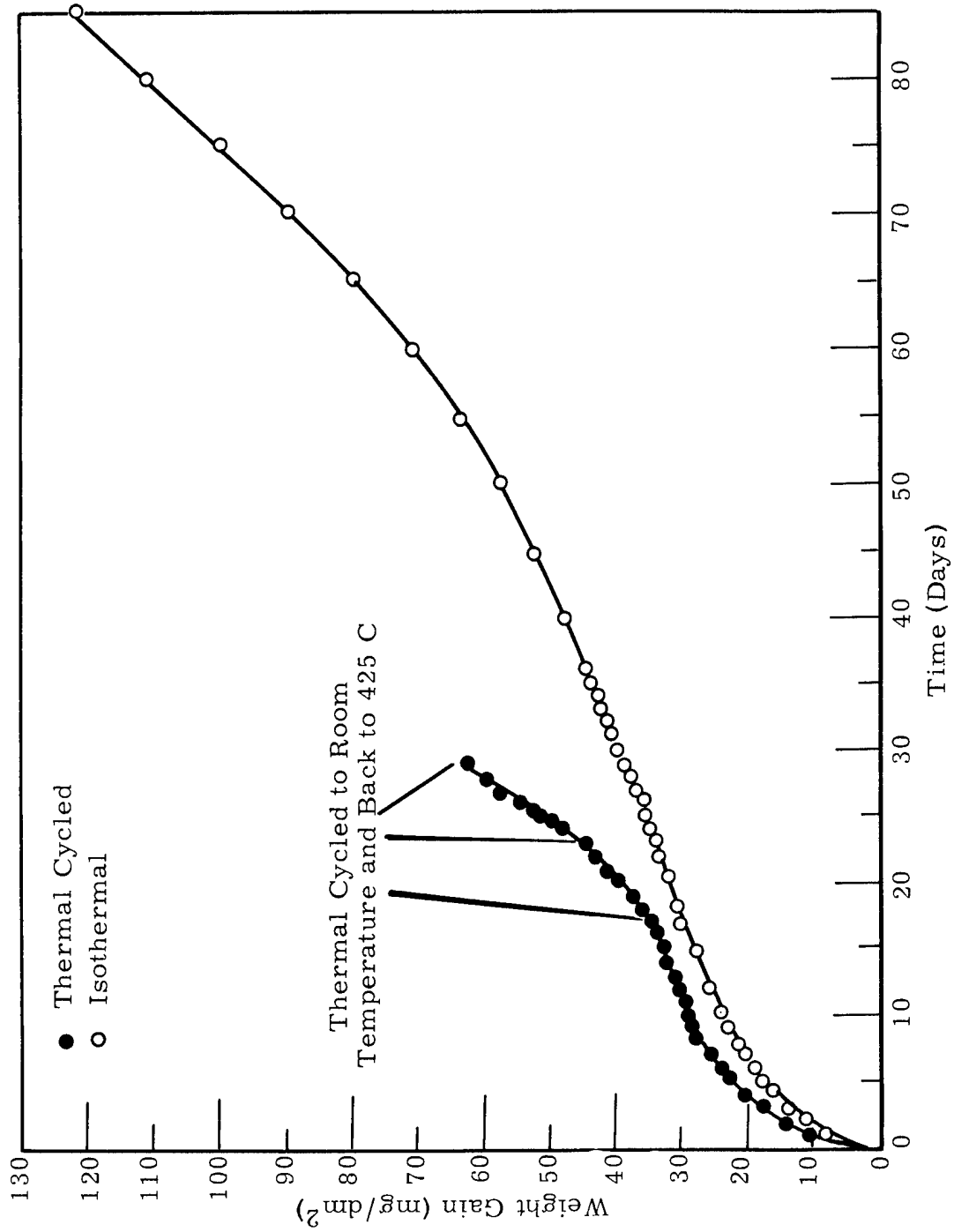


FIGURE 5.8

Effect of Thermal Cycling on the Oxidation
of Zircaloy-2 in Water Vapor, 23 mm Mercury, 425 C

Effect of Mechanically Flexing Autoclaved Zircaloy-2 Samples on
Subsequent Corrosion Behavior - V. H. Troutner*, W. C. Craven,
and R. L. Dillon

In the previous discussion the differences in oxidation of Zircaloy-2 under isothermal and thermal cycling conditions were attributed to mechanical stresses in the oxide film. A previously unreported study also strongly indicates the governing role of mechanical stresses on rate transitions during Zircaloy oxidation.

The multiple rate transitions of oxidizing Zircaloy-2 and Zircaloy-4 were described by Griggs, Maffei, and Shannon in 1960.⁽¹⁾ Repetitive weight gain measurements for single samples over a weight gain range of 100 to 150 mg/dm² in 360 C (680 F) water or 400 C (752 F) steam define clearly three or more film formation and breakdown cycles before definition is lost due to the formation of an increasingly complex oxide-metal interface. The weight gain and time of exposure at breakdown are reasonably reproducible quantities. The simplest explanation of the phenomenon is that general breakdown of the protective oxide occurs when stresses in the oxide exceed the shear strength. This is also the explanation arrived at by Vernon⁽²⁾ in accounting for a similar oxidation pattern for aluminum exposed to room temperature air. For additional confirmation of the physical nature of film breakdown, Troutner examined the possibility of mechanically inducing film breakdown.

Samples, 2 x 1/4 in., were cut from 30 mil Zircaloy-2 strip, etched and weighed. The samples were inserted into a 1.4 liter 300 series stainless steel autoclave operating at 400 C (752 F) at 1500 psi steam pressure. Periodically the autoclave was shut down, samples weighed, and two samples from the test bent around a 1 3/4 in. diameter cylindrical mandrel. The effect of the mechanical distortion of the oxide is to induce premature rate transition in that portion of the oxide affected by the bending, generally 25 to 40% of the sample surface.

* V. H. Troutner, General Electric Company, Pinellas Peninsula Plant.

1. B. Griggs, H. P. Maffei, D. W. Shannon. Multiple Rate Transitions in the Aqueous Corrosion of Zircaloy, HW-67818 REV. December, 1960.
2. W. H. J. Vernon. "First (Experimental) Report to the Atmospheric Corrosion Research Committee," Trans. Faraday Soc., vol. 19, pp. 839 to 845. 1923.

Apparently there is a minimum film thickness required before an effect is observed on the weight gain versus time plot (Figure 5.9). Undoubtedly the critical oxide thickness is a function of the mandrel diameter and the sample thickness, but this relationship has not been investigated. In this experiment about 20 days in 400 C (752 F) steam ($\sim 30 \text{ mg/dm}^2$ oxide thickness) are necessary before film breakdown can be triggered off. Subjected only to natural stress patterns, including those induced by thermal cycling, film breakdown occurs at 39 to 40 mg/dm^2 thickness and approximately 45 days exposure.

Weight gain during induced breakaway amounts to 20 to 35% of the total weight gain during the second corrosion cycle. Bending a sample over the mandrel and straightening by finger pressure appears to affect only the interior third of the sample length. The bent portions of corroded samples have a characteristic gray cast which amounts to 25 to 30% of the sample area in fair agreement with the mechanical behavior of the sample on bending and the ratio of induced-to-total second cycle weight gain.

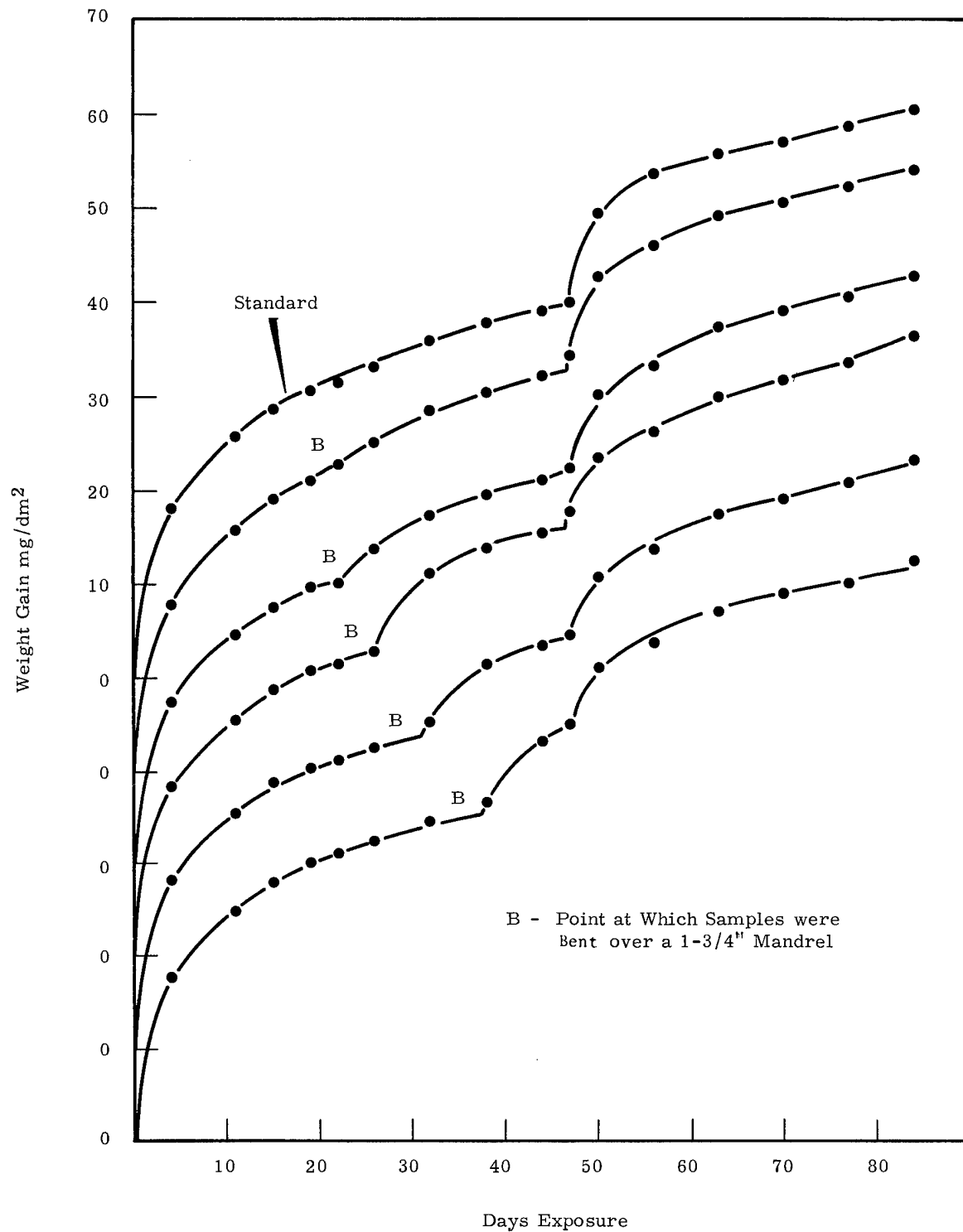


FIGURE 5.9

Induced Breakaway by Bending of Zircaloy-2 Specimens Corroded in 400 C, 1500 psi Steam

Zirconium Hydriding Mechanism - D. W. Shannon

The following mechanism for the hydriding of zirconium was presented in an oral paper to the 13th Annual AEC Corrosion Symposium.* This mechanism is an assimilation and attempted explanation of the work of a number of workers. The tentative state of the mechanism makes acknowledgment premature, but obviously discussions with colleagues at Hanford and elsewhere are reflected in the argument.

In the following list are a number of reasonably well established observations that must be factored into any mechanism on the hydriding of zirconium.

1. The corrosion process is controlled by oxygen diffusion from the environment to the metal.
2. The zirconium oxide corrosion product can be nonstoichiometric, i. e., $\text{ZrO}_{1.9}$ to ZrO_2 .
3. The corrosion weight gain kinetics initially follow a cubic rate law shifting to more or less linear at "transition" but close observation has shown this linear portion can be a series of repetitive nonlinear segments, i. e., multiple rate transitions (Figure 5.10a).
4. In high pressure systems the corrosion rate is relatively independent of oxygen or water pressure.
5. In low pressure systems the post transition corrosion rate becomes increasingly dependent on pressure as the oxide thickens and can fall appreciably below the limiting high pressure value.
6. In the absence of oxidants hydrogen is rapidly absorbed, but concentrations of oxidant sufficient to maintain the normal oxidation rate result essentially in complete inhibition of gas phase hydriding.
7. However, even with oxidants present, very high hydrogen pressures increase the hydriding rate although to a much lower extent than with oxidants absent.

* E. H. Hillner, Bettis Laboratories, Westinghouse, also presented a paper which was somewhat parallel to the ideas presented here.

8. The hydriding pickup fraction during aqueous corrosion has been observed to be high initially, slow down, and then become more rapid after transition following the general shape of Figure 5.10b.
9. Traces of oxygen present during aqueous corrosion reduce the hydrogen absorbed during corrosion in the general manner shown in Figure 5.10c.

Observations 1 and 2 can be used to formulate an explanation of the other observed phenomena in Observations 3 to 9, on the basis that the variations in corrosion rate and hydriding can be explained in terms of constantly changing properties of the film. The oxide film not only grows in thickness but also changes stoichiometry with time along a gradient where the most oxygen deficient oxide is near the metal and the most stoichiometric oxide is on the outer surface. It is not clear at present whether the zirconium/oxygen ratio at the inner and outer surfaces is constant or variable. Experimental determination of the zirconium/oxygen ratio at these surfaces would be most informative.

Explanation

Observation 3 - Cubic Rate Law - The stoichiometry gradients predicted by this model are shown in Figures 5.10 d, e, f, and g associated with the corrosion curve in Figure 5.10a. The corrosion process follows the general law in Stages 1 to 3 of $w = k_1 T^{1/3}$. Corrosion theory for diffusion of oxygen through a film of increasing thickness predicts the parabolic law $w = k_2 T^{1/2}$. However, this assumes diffusion occurs in a media of constant composition (i. e., k_2 is a constant). If the stoichiometry gradient varies as shown in Figures 5.10 d-g then the law would not be parabolic but could be anything depending on the values of k_1 . This model indicates k_1 is a variable and the cubic rate law is the result of changes in both thickness and stoichiometry. The transition sets in when the mechanical stresses set up become too high and extensive film cracking results (Figure 5.10g, Stage 4). The resulting rate controlling layer is thinner, more nonstoichiometric and the corrosion process accelerates.

Observation 4 - High Pressure Independence - Since the corrosion rate is determined by the rate of oxygen diffusion to the metal along the oxygen vacancies (i. e., degree of nonstoichiometry) additional oxygen is only absorbed when a vacancy reaches the outer surface. Since the relative numbers of vacancies are small, a small amount of oxidant will saturate the available sites as fast as they appear and any surplus oxidant has little effect, resulting in pressure independence.

Observation 5 - Low Pressure Dependence - Post Transition - In the post transition region the bulk cracked film can act as a diffusion barrier. At low pressure this effect would slow the oxygen diffusion rate and rate control would shift from diffusion through the coherent to diffusion through the cracked film. This effect might even begin to become important in Stage 3.

Observation 6 - Traces of Oxidants Inhibit Hydriding - When oxidants do not reach the oxide surface fast enough to destroy the vacancies, the degree of nonstoichiometry increases as shown in Figure 5.10h. (This effect has been confirmed by conductivity studies.) If we assume entry of hydrogen is via oxygen vacancies, and the sizes of the atoms and vacancies support this idea, then the rate of hydriding is governed by the vacancy concentration gradient at the outer surface. Once a hydrogen has entered the lattice the concentration of vacancies increasing toward the metal surface makes continued diffusion more rapid. Since the vacancy concentration is much higher in nonoxidizing environments, hydriding is fast in these systems, but since only a little oxidant is required to reduce the outer surface vacancy concentration, traces of oxidant inhibit hydriding. This model predicts that factors which govern the outer vacancy concentration near the outer surface control the hydriding rate.

Observation 7 - High Pressure Hydrogen Increases Hydriding - Since there are always some vacancies at the outer surface there is competition for these sites by oxygen and hydrogen, with hydrogen normally being less readily absorbed. Increasing the hydrogen pressure increases the probability of hydrogen occupying an absorption site, so the hydriding rate would increase slowly with increased hydrogen pressures.

Observation 8 - Hydriding Rate Varies with Corrosion Rate -

Looking at Figure 5.10d-g the variation of hydrogen pickup with extent of corrosion (Figure 5.10b) can be explained as the stoichiometry gradient changes during corrosion. Thus, in Stage 1 hydriding is high because of the high vacancy concentration near the outer surface due to the steep vacancy gradient. As the gradient becomes less the concentration of vacancies near the surface would decrease so hydriding is reduced (Stages 2 and 3). Post transition, (stage 4) the hydriding increases again because the vacancy concentration near the new rate control surface is high due to the steeper vacancy gradient. An additional contribution to hydriding results because the hydrogen generated during corrosion can build up in the crack structure effectively increasing the hydrogen partial pressure at the rate control surface to as high as total system pressure, thus, effectively enriching the environment in hydrogen.

Observation 9 - Oxygen Reduces Hydriding - The oxygen effect in reducing hydriding can be explained on the basis of absorption of oxygen on some of the sites in preference to water, effectively reducing the hydrogen generation rate. Another explanation is possible if oxygen were able to change the stoichiometry at the outer hydriding rate control surface, i. e., if the outer surface were more stoichiometric in oxygen containing systems. The reduced vacancy concentration would be expected to reduce the hydriding rate according to this model. This requires the outer surface stoichiometry to be variable rather than fixed.

The oxygen effect will be expected to become less important post transition since the oxygen is present at a low partial pressure and the "thick film effect" noted in dilute water vapor would be expected to result in a lower oxygen content at the rate control surface for thick film samples.

This mechanism does not yet account for alloy effects but these could be explained on the basis of • how the alloy agent affects the vacancy gradient or • how the alloy affects the plasticity of the oxide which in turn affects the cracks and the stoichiometry of the film or • the alloy agent could catalyze hydrogen entry across the outer vacancy barrier.

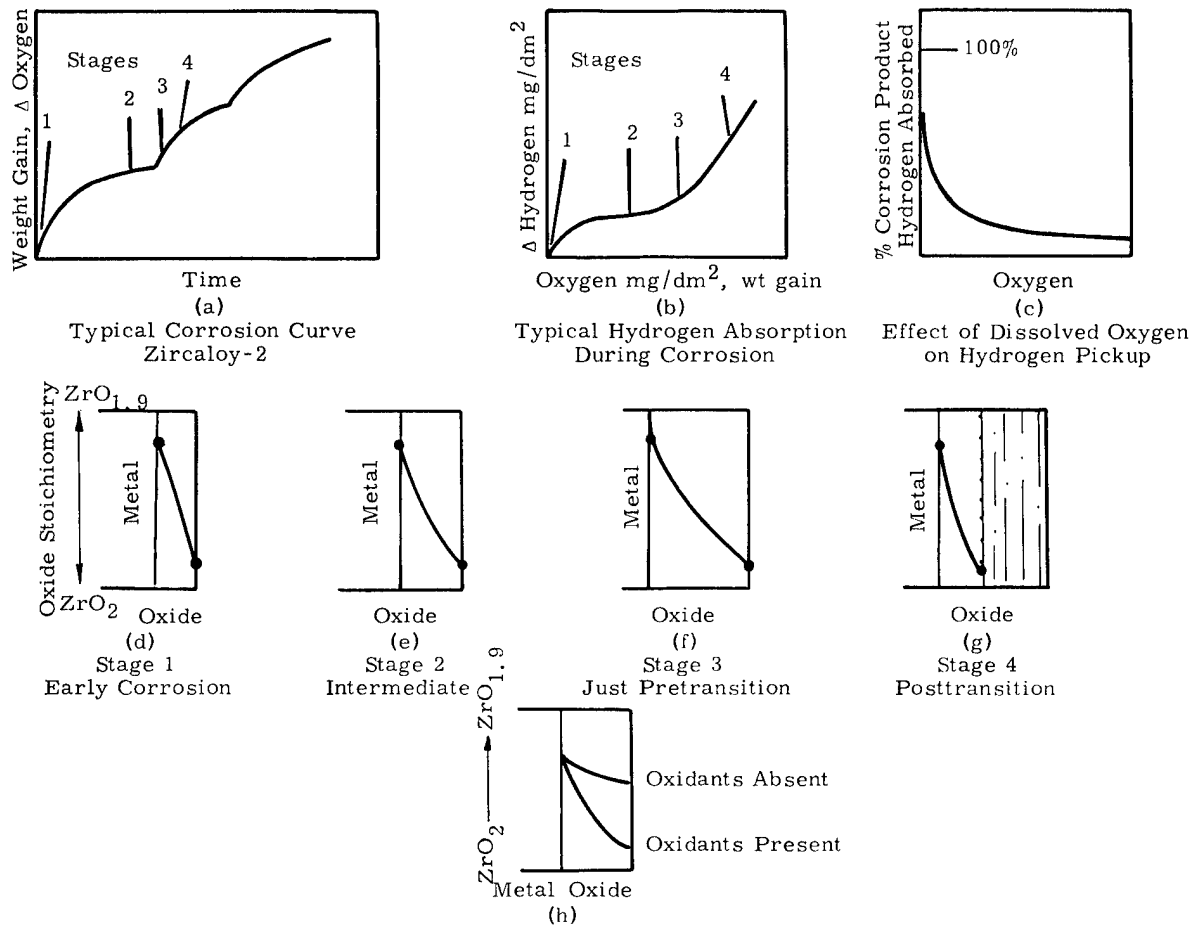


FIGURE 5.10

Stoichiometry Changes in Nonoxidizing Systems

One of the predictions of the model is that alloys with poor corrosion resistance will have low hydriding pickup fraction (not necessarily low total hydriding rates) because the very nature of high oxygen permeability leads to stoichiometric oxide, whereas corrosion resistant alloys with their tightly adherent oxide tend to be more nonstoichiometric. Thus, the goal of the ideal alloy as predicted by this model would be adherent, crack free, stoichiometric oxide film. However, data to date seem to indicate stoichiometric oxides are nonadherent and brittle.

ADVANCED REACTOR CONCEPT STUDIES

Hydride Moderator - W. J. Guay

Equilibrium and kinetic studies of the zirconium-hydrogen system have been undertaken to determine the feasibility of using a variable composition zirconium hydride moderator as a means of reactor control. In the proposed reactor applications temperature will vary from 1400 to 2100 F (760 to 1150 C) maximum, hydride composition will be approximately 5×10^{22} hydrogen atoms/cc ($\text{ZrH}_{1.33}$), size of hydride pellets may be up to 1 in., and pressure will range from approximately 0.5 to 2.0 atm. The hydrogen content of the zirconium hydride moderator can be controlled by temperature or pressure adjustment which may be interdependent. Control of the composition can best be accomplished in the single phase beta region by a simple temperature or pressure adjustment. At reasonable pressures (2.0 or less atm), the maximum hydrogen content which can be obtained in the single phase beta region is approximately $\text{ZrH}_{1.16}$ at 930 C (1706 F). Additional complications arise when maintaining control of the hydrogen content in the range $\text{ZrH}_{1.16}$ to $\text{ZrH}_{1.33}$, the two phase region. It requires either a high pressure system (up to 10 atm) to maintain the single beta phase, or requires the use of the two phase zirconium hydride. The two phase system is more difficult to control because at a given temperature and pressure the composition is not uniquely defined. It means that a control system must be used which meters the amount of hydrogen put into or taken out of the system by a given change of temperature or pressure. This is obviously not as desirable as simple temperature or pressure control in the beta field, but can be done with proper design.

Existing equipment with a vacuum of 10^{-6} mm of mercury was found to be adequate for these studies. The first phase of the investigation has been to determine the equilibrium isotherm of the zirconium-hydrogen system at 750 C (1382 F), using -6 +10 mesh crystal bar zirconium pellets. Data have been obtained over the composition range from $\text{ZrH}_{0.28}$ to $\text{ZrH}_{1.63}$. A plot of pressure versus x , (ZrH_x), shows the beta phase from $\text{ZrH}_{0.28}$ to approximately $\text{ZrH}_{0.99}$, and a two phase region from $\text{ZrH}_{0.99}$ to approximately $\text{ZrH}_{1.43}$. Above $\text{ZrH}_{1.43}$ is in the delta phase region. This checks

the results published by Gilbert⁽¹⁾ reasonably well. His are the only known published values, and unfortunately are in graphical form. Therefore, the best way to check the writer's data is to plot them on a graph along with Gilbert's plotted values. The comparison is shown in Figure 5.11. Equilibrium studies were made during absorption and desorption cycles as shown in Figure 5.11. The results indicate that hysteresis not a major factor in the beta phase or in the two phase region. The spread between the absorption and desorption curves above approximately $x = 1.41$ indicate that equilibrium was probably not attained. It is likely that the absorption cycle did not come to complete equilibrium in the 2 hr that were allowed for experiments. The five points from $ZrH_{1.41}$ up on the absorption curve can be rechecked during the kinetic studies. The discrepancy between the writer's absorption and desorption curves below $x = 1.40$ is thought to be attributable to temperature differences, approximately 730 C (1346 F) versus 750 C (1382 F) for the absorption versus the desorption curves. The desorption curve checks Gilbert's curve within the estimated limits of experimental error ($\pm 5\%$ for the values of x) except for the one point at $x = 1.33$.

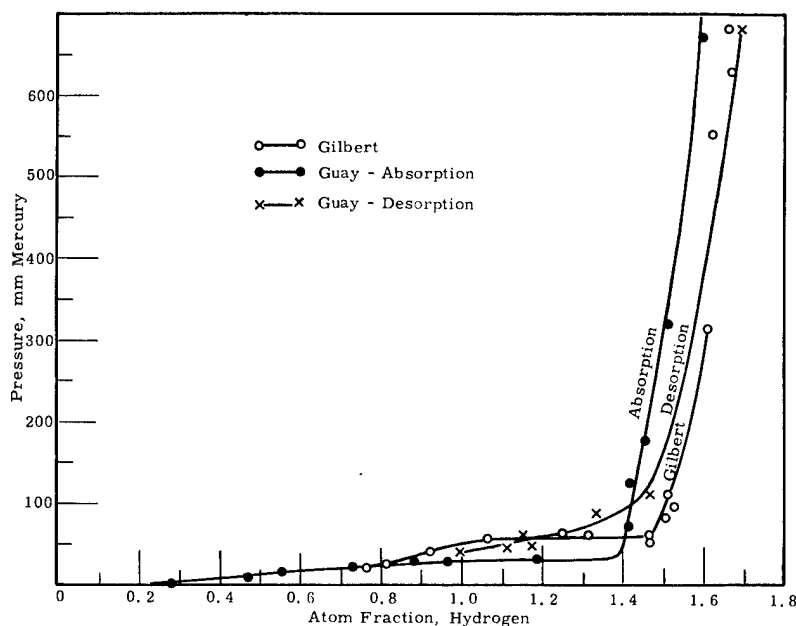


FIGURE 5.11
Equilibrium Isotherm
for Zirconium-Hydrogen
at 750 C

1. Paul T. Gilbert, Jr. Zirconium Hydride: A Compendium on the Systems Zirconium-Hydrogen and Hafnium-Hydrogen, and Related Topics, NAA-SR-1508, Atomics International Division, North American Aviation, Inc., Canoga Park, California. October 15, 1956.

Variable Composition Hydride Moderator Studies - W. J. Guay

Kinetic data were taken at 1385 F (750 C) using -6 +10 mesh crystal bar zirconium pellets over the composition range from $\text{ZrH}_{0.27}$ to $\text{ZrH}_{1.32}$ in a closed system where hydrogen was neither added to nor taken from the system during an experiment. Hydrogen pressure was thus continuously decreasing during absorption and continuously increasing during desorption. During absorption the time required for 90% of saturation varied from 3 to 24 min and during desorption from 2 to 8 min. Indications are that the rates of absorption and desorption are greater for the second absorption-desorption cycle rather than for fresh zirconium. Absorbed oxygen at the surface was probably a retarding factor during the first cycle. It is probable that the faster rates that were obtained (3 min for absorption and 2 min for desorption) could be consistently reproduced in a cleaner system. The vacuum used in these experiments was approximately 1×10^{-5} mm mercury. Since 90% absorption or desorption took place in a matter of minutes in all cases the use of a variable composition hydride moderator appears to have real promise in reactor technology. Funding for this work was discontinued. Work on this program has terminated though extension of the studies would be of interest to higher hydrogen composition and to higher temperatures, up to 1150 C (2102 F).

PRODUCTION REACTOR CORROSION AND COATING STUDIES

Corrosion of Aluminum-Rotating Disk Method - A. B. Johnson

Studies to investigate velocity effects on corrosion of aluminum have been conducted primarily in the high pH region (8.5-9.3).⁽¹⁾ Recent tests were conducted using 300 ppm chloride ion (as NaCl) and 300 ppm chloride plus 2 ppm copper ion (as CuCl_2) in Columbia River water to investigate possible synergistic effects of the ions on pit initiation. In 72 hr tests, no pitting was observed in either solution, using 8001 aluminum alloy disks (0.5% iron, 1.0% nickel).

A series of tests was conducted at low pH (3.2-7.8). At pH 3.2, pits were initiated after a 6 day exposure. The sample surface was apparently free of oxide film at the end of the 6 day exposure, and the corrosion attack proceeded rapidly. The rate was approximately 150 times faster at pH 3.2 than at pH 4.0. The disk in pH 3.2 water lost 14.6 g while the disk in pH 4.0 water lost 0.1 g. At pH 3.2 the disk was thinned near the outer edge. The plate thickness varied from 61.5 mils (0.0615 in.) near the center to 27 mils at the outer edge.

At pH 4.0, pits were initiated in a 10 day exposure, but were discernible only under the microscope (~10X).

At pH 7.2-7.8 rate of attack (as indicated by weight loss) was approximately double the rate at pH 4.0; however, no pitting was observed at pH 7.2-7.8 in exposures to 6 days.

1. Quarterly Progress Report - Metallurgy Research Operation, January, February, March, 1964, edited by J. J. Cadwell, HW-81269. April 15, 1964.

N REACTOR CORROSION AND HYDRIDING STUDIES

Effect of Thick Oxide Films on the Hydriding of Zircaloy-2 in Contaminated Helium - D. W. Shannon

Thick oxide films on Zircaloy-2 are being studied to determine effects on corrosion and hydriding in helium contaminated with traces of H_2O , CO , and H_2 . It was previously reported⁽¹⁾ that the presence of a thick oxide film could lead to an acceleration in hydriding. A factorial experiment has been set up to expose Zircaloy-2 coupons ($2.54 \times 1.25 \times 0.076$ cm) with film thickness of 0, 50, 100, 200, and 450 mg/dm^2 to helium contaminated with H_2 at 250 and 2000 ppm levels and H_2O inhibitor at 350 and 900 ppm levels and at temperatures of 250, 300, 350, and 400 C (482, 572, 662, and 752 F). CO was added to the same concentration as the hydrogen since CO is often present in reactor gases; however, the CO is thought to be relatively inert in this system. The coupons were prepared by bright etching in HNO_3 -HF, drying and weighing to six decimal places. Some of the samples were then prefilmed in oxygen at 450 C (842 F) to the required weights with a tolerance allowed of $\pm 10\%$ in the weight. It is recognized that prefilming in oxygen at high temperature may not produce the same films as long term exposure to H_2O at low temperature. However, a large number of etched samples were included in the experiment and will ultimately reach high weight gains under actual conditions.

Weight gain and hydrogen absorption data were taken at 26, 40, and 70 days exposure. Only the 70 day data are to be given here (Figures 12 to 17). Examination of the weight gain data (Figures 12 to 14) indicates the corrosion rate drops off sharply with increasing film thickness for all temperatures.

1. Quarterly Progress Report - Metallurgy Research Operation, April, May, June, 1963, edited by J. J. Cadwell, HW-77954. July 15, 1963.

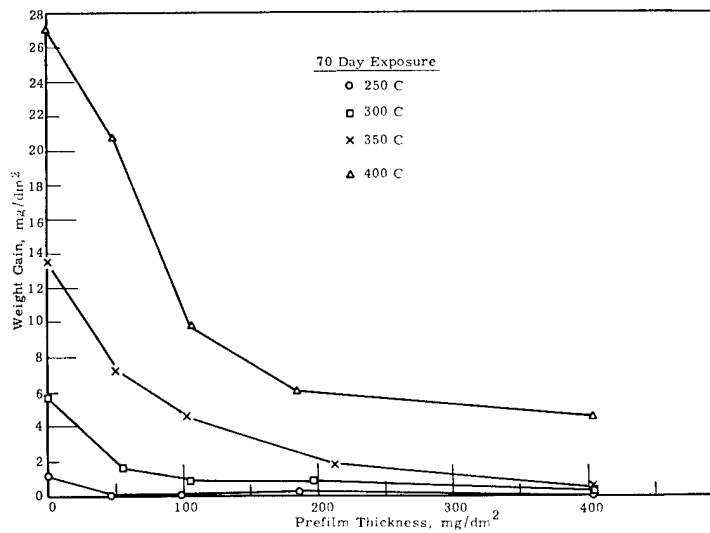


FIGURE 5.12

Oxidation of Prefilmed Zircaloy-2 in Helium Containing 250 ppm H₂, 250 ppm CO, and 350 ppm H₂O (Gas A)

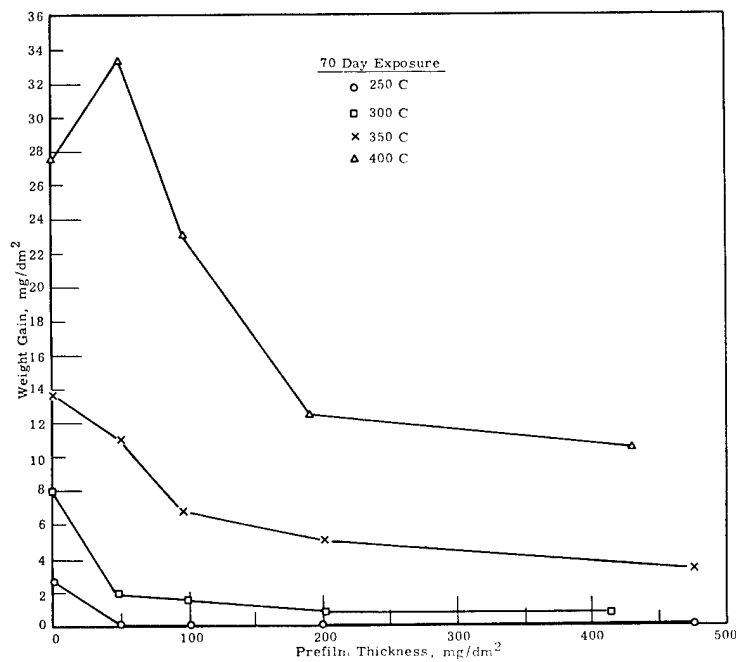


FIGURE 5.13

Oxidation of Prefilmed Zircaloy-2 in Helium Containing 250 ppm H₂, 250 ppm CO, and 900 ppm H₂O (Gas B)

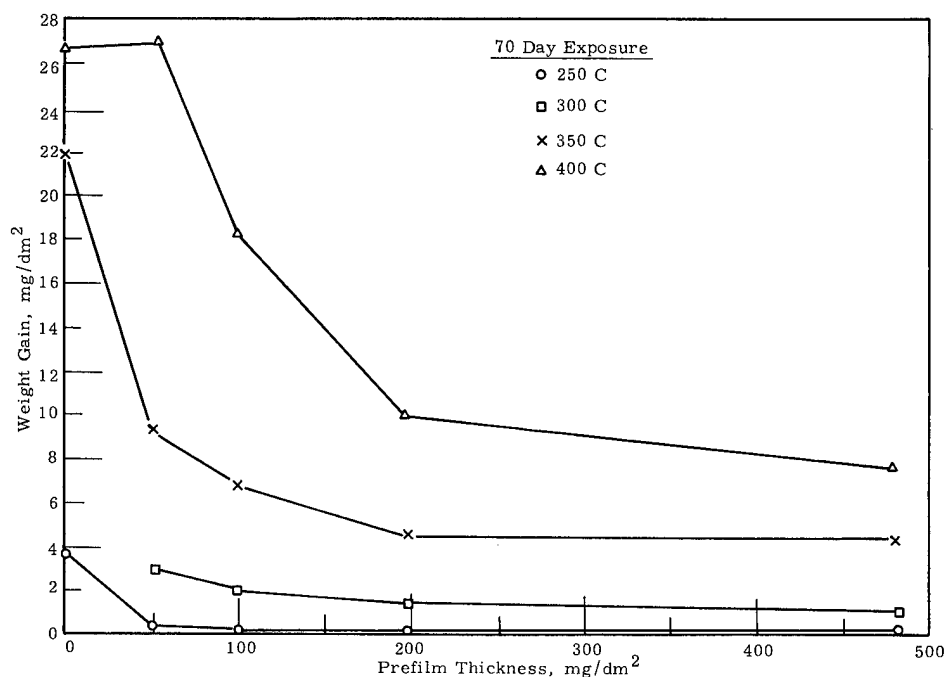


FIGURE 5.14

Oxidation of Prefilmed Zircaloy-2 in Helium Containing 2000 ppm H₂, 2000 ppm CO, and 100 ppm H₂O (Gas C)

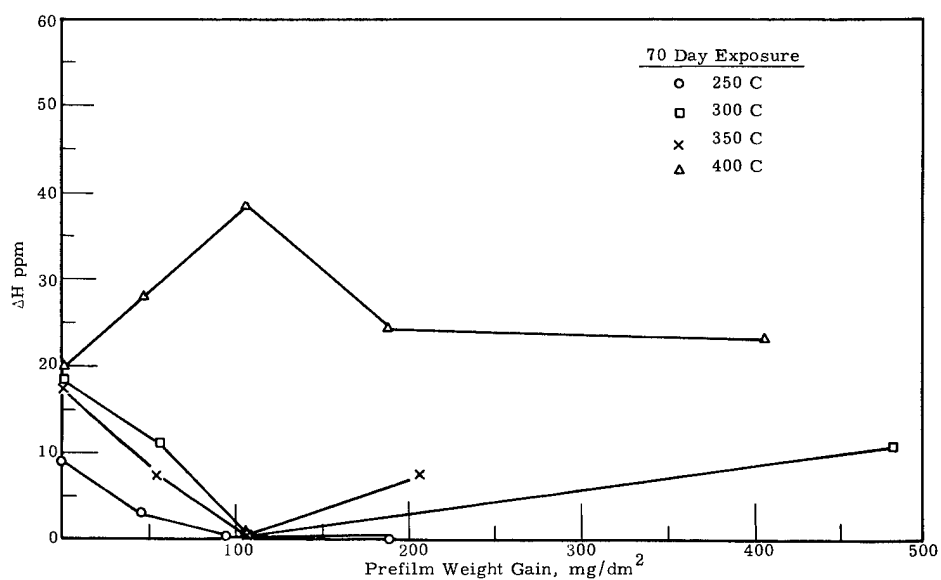


FIGURE 5.15

Hydrogen Absorption of Prefilmed Zircaloy-2 in Helium Containing 250 ppm H₂, 250 ppm CO, 350 ppm H₂O (Gas A)

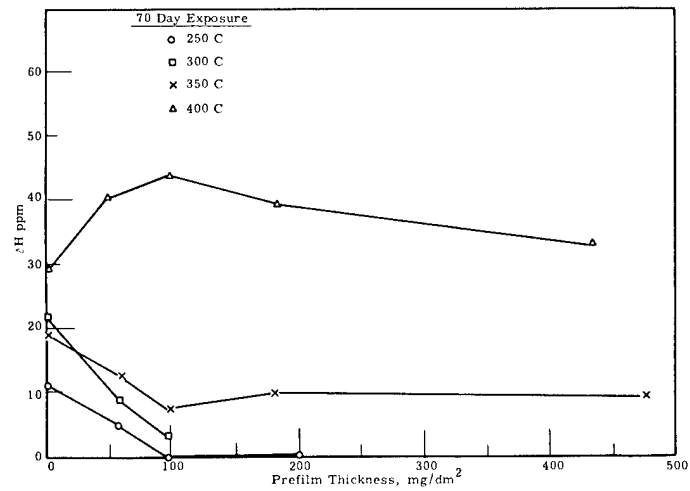


FIGURE 5.16

Hydrogen Absorption of Prefilmed Zircaloy-2 in Helium
Containing 250 ppm H₂, 250 ppm CO, and 900 ppm H₂O (Gas B)

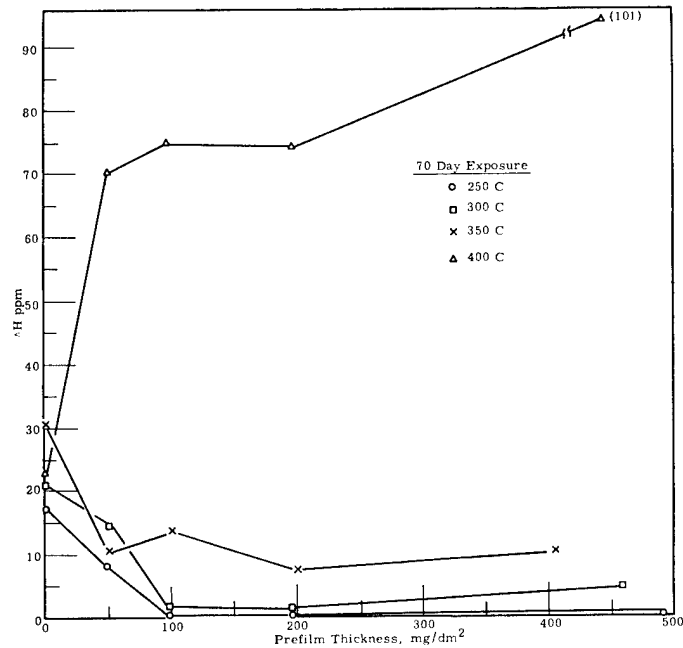


FIGURE 5.17

Hydrogen Absorption of Prefilmed Zircaloy-2 in Helium
Containing 2000 ppm H₂, 2000 ppm CO, and 900 ppm H₂O (Gas C)

In high pressure systems the corrosion rates (and 70 day weight gains) would be expected to be higher for prefilmed than for the unfilmed samples. This behavior is seen in Figures 13 and 14 where the 50 mg/dm² films at 900 ppm H₂O do not drop off as rapidly as the 350 ppm run. However, where more than 50 mg/dm² prefilm is present, all samples show a considerable reduction in oxidation rate. This means that the presence of the thick oxide film regulates the diffusion of water from the environment. Previous thin film experiments have indicated that whenever the oxidation rate becomes limited by some process other than diffusion of oxidant through the compact inner oxide the samples are prone to hydriding. Consistent with this observation, all prefilmed samples exposed to gas mixtures containing 2000 ppm hydrogen at 400 C (752 F) have reduced oxidation rates and also have absorbed gaseous hydrogen after 70 days. Hydrogen pickup in all other samples at all other temperatures can be accounted for by the corrosion process. In gas mixtures containing 250 ppm hydrogen at 400 C (752 F) no gas phase hydriding has occurred indicating there is also a pressure dependence on the hydriding reaction. This means that the thick films also slow hydrogen diffusion as well as water diffusion.

This experiment is scheduled to run several years because at the low H₂ pressures and low temperatures significant effects are not expected rapidly.

MATERIALS ENGINEERING

PRTR PRESSURE TUBES

In-Reactor Monitoring - P. J. Pankaskie

As an aid in assessing the performance of Zircaloy-2 as a pressure tube material the pressure tubes in the PRTR are periodically and nondestructively inspected in situ. These inspections usually consist of a visual examination of the inside surface to detect and measure the extent of localized corrosion and of mechanical damage from fuel charge-discharge; measurement of the inside diameter to detect creep deformation if any; and measurement of the extent of eccentricity of the helium insulating annulus between the Zircaloy-2 pressure and the aluminum shroud tubes.

During this quarter, 32 visual inspections were made in the pressure tubes in 29 process channels. Inside diameter and gas annulus measurements were made of the pressure tubes in 15 process channels. Visual examinations this quarter disclosed only minor fretting corrosion. No significant changes in pressure tube diameters were disclosed. Gas gap measurements disclosed significant amounts of eccentricity of the gas annulus in 5 of 15 process channels measured this quarter. Preliminary analysis indicates that some of the observed eccentricity may be attributable to temporary forces imposed on the outlet nozzles of these process channels by the inspection equipment. Tests will be made to determine if the measuring equipment forces cause tube bowing.

New inspection equipment was placed in operation this quarter and was used for inspection of 15 process channels. With the exception of relocating two limit switches, debugging is essentially complete.

Tube Testing - M. C. Fraser

Burst Test of Tube 6079. PRTR tube 6079 was discharged from channel number 1354 on March 3, 1964, having an average exposure of 326.5 Mwd which is 9.47×10^{20} fast nvt. Selection of tube 6079 to be the twelfth destructively examined was based upon the number of fret marks and neutron exposure. It had three fret marks whose depth was in the range 2.54 mm to 3.81 mm (10 to 15 mils) that had been produced by fuel element supports. This tube was discharged approximately one operating month after its predecessor - tube 6115.

Two 0.508 meter (20 in.) long pieces of this tube were pressurized to failure at room temperature. The fret marks mentioned above were on these pieces. The Lamé hoop stress at maximum pressures sustained were 7640 kg/cm^2 (108,600 psi) and 8700 kg/cm^2 (124,000 psi). Both pieces displayed circumferential plastic deformation. The piece with the lower strength had annealed microstructure and the other had cold-worked microstructure.

Vacuum fusion analysis of samples from both specimens indicated that the metal in the region of the burst origin had 70 to 80 ppm hydride, whereas elsewhere it was normal at 25 to 40 ppm.

Upon completion of the post burst test examination, the role of the fret marks in burst initiation and propagation will have been studied.

Eddy Current Probe of Tube 5526. PRTR tube number 5526 was discharged from channel number 1558 on October 10, 1963 because of the presence at 2.42 meters (7 ft 11 in.) from the flange and on the ID of a large unclassified flaw. Visual observation indicated it was a blister. Remote nondestructive examination of this flaw was performed using an eddy current device with the tube in the vertical position, but under water at the PRTR storage basin. Position control of the eddy current sensor on the end of a pole was done by hand. The eddy current data obtained indicate that this flaw is less than 0.159 cm (5/8 in.) long, less than 0.635 cm (1/4 in.) wide, and may be as deep as 1.01 mm (0.040 in.).

Crack Propagation. A 9.65 mm (0.38 in.) long crack in a cold-worked and in an annealed specimen of unirradiated PRTR Zircaloy-2 pressure tubing propagated at pressures of 545 kg/cm^2 (7750 psig) and 530 kg/cm^2 (7540 psig), respectively. The tests were done at room temperature. Dimensional differences between the two specimens made the Lamé hoop stress at propagation 6000 kg/cm^2 (85,300 psi) for both specimens. Preliminary examination of electron microfractographs of the fracture surfaces indicates that the fracture mechanism was principally shear; however, some cleavage was observed. Macroscopically, the fracture surfaces of both specimens displayed a chevron structure which is usually associated with cleavage. There was no apparent difference in behavior in spite of the dissimilar microstructure.

The cracks in these two specimens were manufactured by first milling slots of the desired length and width to a depth of 80% of the wall; and then, upon pressurization of the specimen, failure of the 20% wall produced a natural crack. With a "patch" over the crack to prevent loss of pressure, the specimen was pressurized a second time to cause crack propagation.

N-REACTOR PRESSURE TUBES

Brittle Fracture Tests - R. C. Aungst

A previous quarterly report ⁽¹⁾ described a method of brittle fracture testing based upon pressurizing a tubular sample defected by milling a slot of given length to a depth of 80% of the wall thickness. Tests were performed at room temperature on N-Reactor tubing for slots varying from 1.27 cm (0.5 in.) to 3.81 cm (1.5 in.) and the results plotted as stress for brittle fracture versus slot length. This curve fits reasonably well the theoretical equation

$$S(L)^{1/2} = C$$

where S is failure stress, L is slot length and C is a material constant. The equation that provided the best fit to the experimental data was

$$S(L)^{1/2} = 7730$$

when S is in kg/cm^2 and L is in cm and $S(L)^{1/2} = 69,000$
when S is in lb/in.^2 and L is in inches.

Since the previous report, tests have been performed on this same material at slot lengths to 7.62 cm (3 in.). The previous data has been combined with the more recent results and replotted as log stress for failure versus log slot length (Figure 6.1). This form facilitates statement of the mathematical relationship and defines the deviation from the theoretical. The equation most nearly fitting all the data for as-received 30% drawn N-Reactor tubing is

$$S(L)^{0.62} = 8260 \text{ (Metric Units)} \\ (66,000) \text{ (English Units)}$$

-
1. Quarterly Progress Report - Metallurgy Research Operation - July, August, September, 1963, edited by J. J. Cadwell, HW-78962. October 15, 1963.

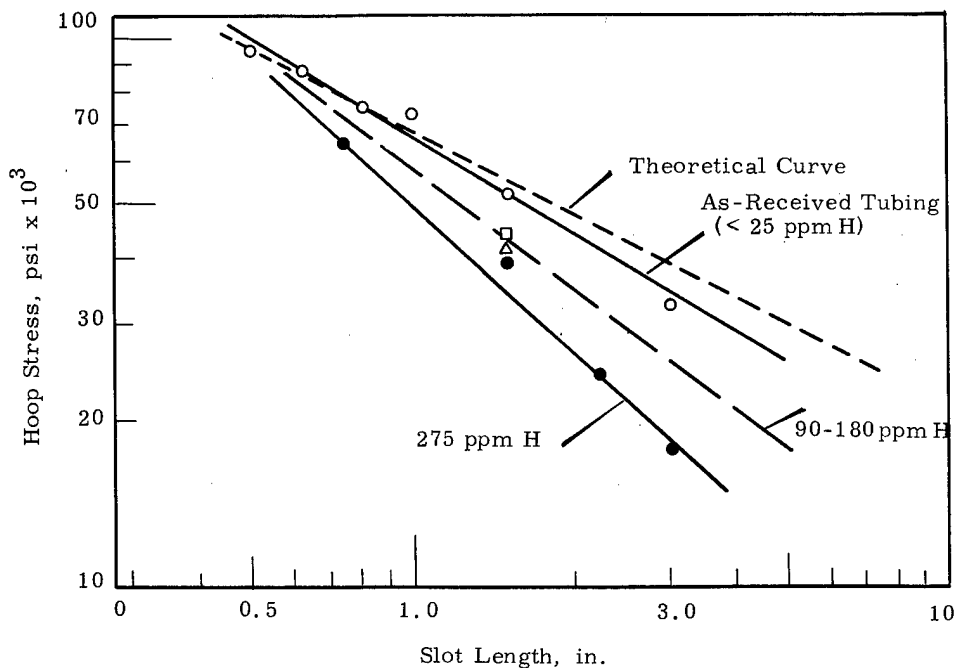


FIGURE 6.1

Effect of Hydrogen Content
on Susceptibility to Brittle Failure of Zircaloy-2 N-Reactor Tubing
(Room Temperature Tests)

Tests have been performed on material similar to that above, but hydrided to levels up to 275 ppm. The equation for material at the 90 to 180 ppm level is

$$S(L)^{0.86} = 8940$$

(57,000)

and for tubing hydrided to 275 ppm the equation is

$$S(L)^{0.93} = 8350$$

(50,000)

As hydrogen levels increase so does the value of the exponent and the system becomes increasingly sensitive to larger defects.

The design stress for N-Reactor tubing is about 700 kg/cm² (10,000 psi). If the curves of Figure 6.1 are extrapolated to this stress value it should indicate the crack length for instability at room temperature and operating pressure. For the as-received material this length appears to

be 58.5 cm (23 in.) and is reduced to 15.2 cm (6 in.) upon the accumulation of 275 ppm hydrogen.

Figure 6.2 shows a similar plot of room temperature data for KER tubing in both the unirradiated and irradiated conditions. The open circles represent tests on the as-received tubing and the solid circles represents tests of similar material after 3 to 4 years residence in-reactor. No quantitative irradiation figure in nvt is available for these specimens, but they can be rated in order of the relative amount of irradiation received. Note that 3 of the 4 irradiated points fall almost exactly on the curve established by the tests of as-received tubing. The one point that does deviate represents one of the specimens receiving an intermediate amount of irradiation, suggesting that some other factor is responsible for the deviation. These data, preliminary in nature, indicate little or no effect of irradiation on the susceptibility of this material to brittle fracture.

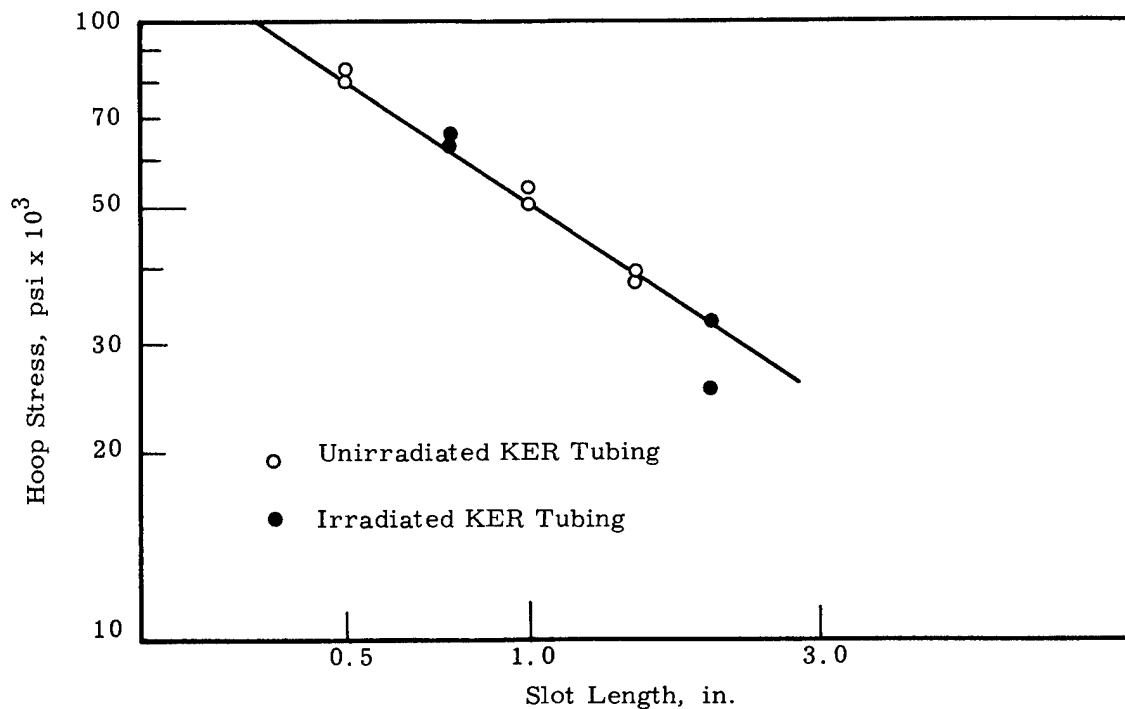


FIGURE 6.2

Effect of Irradiation
on Susceptibility to Brittle Failure of Zircaloy-2 KER Tubing
(Room Temperature Tests)

Irradiated Tube Testing Facility - P. M. Jackson

The new facility for postirradiation evaluation of reactor pressure tubing has been in operation during this quarter (Figure 6.3). Burst tests have been completed on two PRTR tube sections and seven KER tube sections. Heat balance tests have been conducted in three of the new furnace-containment vessels and a specimen temperature uniformity of 2 to 3 C was readily obtained at a temperature of 300 C (572 F).

The underwater remotely fired gun mechanism for initiating a crack in an irradiated tube has been completed and checked out. Good results have been obtained with this device and it functions satisfactorily.

NPR Steam Generator Tubing Tests. The testing program for the NPR steam generator tubing was completed and the final report was issued⁽¹⁾. This report covered tests on 58 individual tube sections with variable flaw types, pressures and temperature. The limited test program undertaken has shown that operational failures which could and probably will occur will not be of the catastrophic type.

1. P. M. Jackson. NPR Steam Generator Tubing Burst Tests, HW-82233. May 8, 1964.

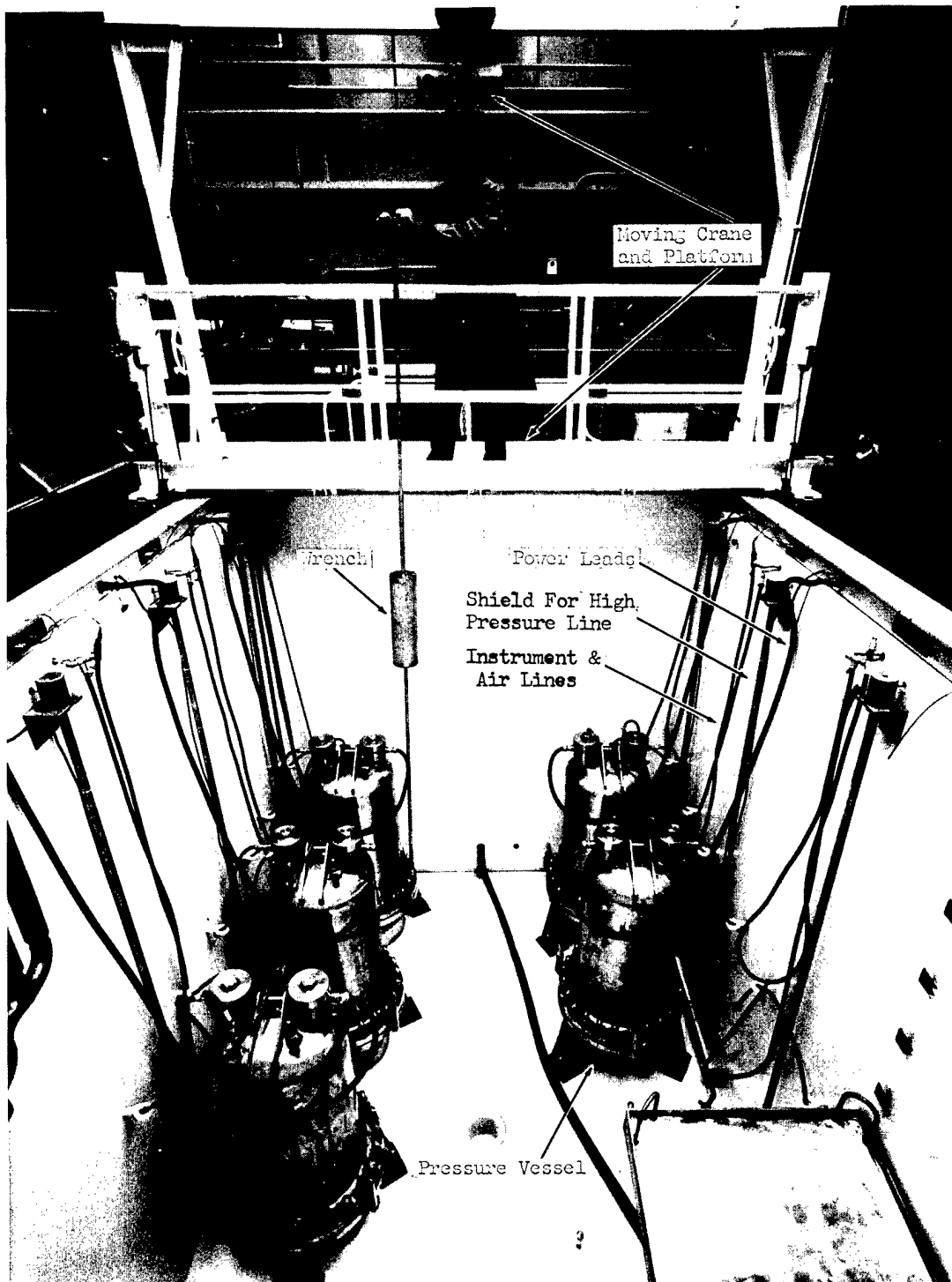


FIGURE 6.3
Irradiated Tube Test Facility

INTERNAL DISTRIBUTIONCopy Number

1	F. W. Albaugh - H. M. Parker
2	T. W. Ambrose
3	J. A. Ayres
4 - 5	T. K. Bierlein
6	S. H. Bush
7	J. J. Cadwell
8	T. T. Claudson
9	D. L. Condotta
10	L. L. Crawford
11	D. H. Curtiss
12	D. R. de Halas
13	R. L. Dickeman
14 - 15	R. L. Dillon
16	K. Drumheller
17	E. A. Eschbach
18	E. A. Evans
19	T. W. Evans
20	J. C. Fox
21	J. M. Fox, Jr.
22	L. A. Hartcorn
23	H. Harty
24	W. M. Harty
25	R. S. Kemper
26	G. A. Last
27	M. C. Leverett
28	C. G. Lewis
29	L. M. Loeb
30	J. E. Minor
31	W. N. Mobley
32	R. D. Nelson
33	J. W. Nickolaus
34	R. E. Nightingale
35	R. Nilson
36	D. P. O'Keefe
37	R. E. Olson
38	R. S. Paul
39	J. W. Riches
40	W. E. Roake
41	E. D. Sayre
42	R. K. Sharp
43	F. A. Smidt
44 - 45	J. C. Tobin
46	F. W. Van Wormer
47	E. E. Voiland
48	M. T. Walling
49 - 50	R. G. Wheeler
51	O. J. Wick
52	300 File Copy
53	Record Center
54 - 58	Extra
59 - 60	Technical Publications

EXTERNAL DISTRIBUTION (Special)Number of Copies

2	Atomic Energy Commission, Washington Division of Research Attn: Don K. Stevens Dorothy Smith
2	Atomic Energy Commission, Washington Division of Reactor Development Attn: W. R. Voigt J. M. Simmons
1	Atomic Energy Commission, Washington Military Liaison Committee Attn: Captain D. E. McCoy, Staff Assistant to the Chairman
1	Battelle Memorial Institute Radiation Effects Information Center Attn: W. H. Veazie
1	Center for Nuclear Studies at Saclay P. O. Box #2 Gif-sur-Yvette (Seine-et-Oise), France Attn: Thomas de Montpreville
1	European Atomic Energy Community (Euratom) 51-53- rue Belliard Brussels, Belgium Attn: Pierre Kruys
2	General Electric Technical Data Center, Schenectady
1	H. J. Pessl Route 1, Box 892 Hood River, Oregon
1	RLOO, Technical Information Library
1	University of California, Berkeley Attn: J. F. Dorn
1	University of Florida Metallurgical Research Laboratory College of Engineering Attn: R. T. de Hoff
1	University of Michigan Attn: M. J. Sinnot

Ptd.	Standard Distribution	Ptd.	Standard Distribution
3	ABERDEEN PROVING GROUND	2	BROOKHAVEN NATIONAL LABORATORY
1	AEROJET-GENERAL CORPORATION	1	BUREAU OF MINES, ALBANY
1	AEROJET-GENERAL NUCLEONICS	1	BUREAU OF NAVAL WEAPONS
2	AERONAUTICAL SYSTEMS DIVISION	1	BUREAU OF SHIPS (CODE 1500)
1	AEROPROJECTS INCORPORATED	1	CARBORUNDUM COMPANY
		1	CHICAGO PATENT GROUP
1	AIR FORCE INSTITUTE OF TECHNOLOGY	1	COMBUSTION ENGINEERING, INC.
	AIR FORCE INSTITUTE OF TECHNOLOGY (MAFB)	1	COMBUSTION ENGINEERING, INC. (NRD)
1	ALLIS-CHALMERS MANUFACTURING COMPANY	1	DEFENCE RESEARCH MEMBER
1	ALLIS-CHALMERS MANUFACTURING COMPANY, BETHESDA	1	DENVER RESEARCH INSTITUTE
1	ALLISON DIVISION-GMC	4	DU PONT COMPANY, AIKEN
10	ARGONNE NATIONAL LABORATORY	1	DU PONT COMPANY, WILMINGTON
1	ARMY ENGINEER RESEARCH AND DEVELOP- MENT LABORATORIES	1	FRANKFORD ARSENAL
1	ARMY MATERIALS RESEARCH AGENCY	1	FRANKLIN INSTITUTE OF PENNSYLVANIA
1	ARMY MISSILE COMMAND	1	FUNDAMENTAL METHODS ASSOCIATION
1	ARMY RESEARCH OFFICE, DURHAM	2	GENERAL ATOMIC DIVISION
1	ARMY TANK-AUTOMOTIVE CENTER	2	GENERAL DYNAMICS/FORT WORTH
1	ATOMIC ENERGY COMMISSION, BETHESDA	2	GENERAL ELECTRIC COMPANY, CINCINNATI
1	AEC SCIENTIFIC REPRESENTATIVE, BELGIUM	1	GENERAL ELECTRIC COMPANY, PLEASANTON
1	AEC SCIENTIFIC REPRESENTATIVE, FRANCE		
1	AEC SCIENTIFIC REPRESENTATIVE, JAPAN	1	GENERAL ELECTRIC COMPANY, SAN JOSE
3	ATOMIC ENERGY COMMISSION, WASHINGTON	1	GENERAL NUCLEAR ENGINEERING CORPORATION
4	ATOMIC ENERGY OF CANADA LIMITED	1	GOODYEAR ATOMIC CORPORATION
		1	IIT RESEARCH INSTITUTE
2	ATOMIC ENERGY OF CANADA LIMITED, WHITESHELL	2	IOWA STATE UNIVERSITY
4	*ATOMICS INTERNATIONAL	2	JET PROPULSION LABORATORY
1	AYCO CORPORATION	1	JOHNS HOPKINS UNIVERSITY
4	BABCOCK AND WILCOX COMPANY	3	KNOLLS ATOMIC POWER LABORATORY
2	BATTELLE MEMORIAL INSTITUTE	1	LING TEMCO VOUGHT, INC.
2	BEERS (ROLAND F.), INC.	1	LOCKHEED-GEORGIA COMPANY
1	BERYLLIUM CORPORATION	1	LOCKHEED MISSILES AND SPACE COMPANY (NASA)
1	BRIDGEPORT BRASS COMPANY	3	LOS ALAMOS SCIENTIFIC LABORATORY
1	*BRIDGEPORT BRASS COMPANY, ASHTABULA	1	M & C NUCLEAR, INC.

Ptd.	Standard Distribution	Ptd.	Standard Distribution
1	MALLINCKRODT CHEMICAL WORKS	1	RADIOPTICS, INC.
1	MARITIME ADMINISTRATION	1	RAND CORPORATION
1	MARTIN-MARIETTA CORPORATION	1	RENSSELAER POLYTECHNIC INSTITUTE
1	MOUND LABORATORY	1	SAN FRANCISCO OPERATIONS OFFICE
		2	SANDIA CORPORATION, ALBUQUERQUE
1	NASA LEWIS RESEARCH CENTER	1	SANDIA CORPORATION, LIVERMORE
		1	SPACE TECHNOLOGY LABORATORIES, INC. (NASA)
1	NASA MANNED SPACECRAFT CENTER	1	STANFORD UNIVERSITY (SLAC)
2	NASA SCIENTIFIC AND TECHNICAL INFORMATION FACILITY	1	SYLVANIA ELECTRIC PRODUCTS, INC.
		1	TENNESSEE VALLEY AUTHORITY
2	NATIONAL BUREAU OF STANDARDS	2	UNION CARBIDE CORPORATION (CRGDP)
1	NATIONAL BUREAU OF STANDARDS (LIBRARY)	5	UNION CARBIDE CORPORATION (ORNL)
2	NATIONAL LEAD COMPANY OF OHIO		
1	NAVAL POSTGRADUATE SCHOOL	1	UNION CARBIDE CORPORATION (PADUCAH PLANT)
3	NAVAL RESEARCH LABORATORY	2	UNITED NUCLEAR CORPORATION (NDA)
		1	U. S. GEOLOGICAL SURVEY, DENVER
1	NUCLEAR MATERIALS AND EQUIPMENT CORPORATION	1	U. S. GEOLOGICAL SURVEY, MENLO PARK
1	NUCLEAR METALS, INC.	1	U. S. GEOLOGICAL SURVEY, WASHINGTON
1	NUCLEAR UTILITY SERVICES, INC.	1	U. S. PATENT OFFICE
1	OFFICE OF ASSISTANT GENERAL COUNSEL FOR PATENTS (AEC)	2	*UNIVERSITY OF CALIFORNIA, BERKELEY
		2	UNIVERSITY OF CALIFORNIA, LIVERMORE
2	OFFICE OF NAVAL RESEARCH	1	UNIVERSITY OF PUERTO RICO
1	OFFICE OF NAVAL RESEARCH (CODE 422)	1	WESTERN RESERVE UNIVERSITY (MAJOR)
1	OHIO STATE UNIVERSITY	4	WESTINGHOUSE BETTIS ATOMIC POWER LABORATORY
1	PETROLEUM CONSULTANTS	1	WESTINGHOUSE ELECTRIC CORPORATION
4	PHILLIPS PETROLEUM COMPANY (NRTS)	1	WESTINGHOUSE ELECTRIC CORPORATION (NASA)
1	PHYSICS INTERNATIONAL, INC.	325	DIVISION OF TECHNICAL INFORMATION EXTENSION
1	PICATINNY ARSENAL	75†	OFFICE OF TECHNICAL SERVICES, WASHINGTON
1	POWER REACTOR DEVELOPMENT COMPANY		
3	PRATT AND WHITNEY AIRCRAFT DIVISION		
1	PURDUE UNIVERSITY		

*New listing or change in old listing.

†These copies should be shipped directly to the Office of Technical
Services, Department of Commerce, Washington, D. C. 20230